TÉCNICO LISBOA

Concept development and construction of a high-precision handling and cutting system for the automation of battery cell production

Berk Gökoğlu

Thesis to obtain the Master of Science Degree in

Energy Engineering and Management

Supervisors: Prof. Maria de Fátima Grilo da Costa Montemor

M. Sc. Hannes Wilhelm Weinmann

Examination Committee

Chairperson: Prof. Duarte de Mesquita e Sousa

Supervisor: Prof. Maria de Fátima Grilo da Costa Montemor

Member of the Committee: Dr. André Diogo Tavarez Mão de Ferro

May 2019

I declare that this document is an original work of my own authorship and that it fulfils all the requirements of the Code of Conduct and Good Practices of the Universidade de Lisboa.

To my family and friends who helped me through this serpentine journey with their endless support and encouragement.

Acknowledgements

First of all, I would like to extend my gratitude to my supervisors Hannes Weinmann and Prof. M. Fatima Montemor for guiding me and giving me their precious opinions. Their assistance helped me not only to find the right direction but also to improve the quality of my work. Additionally, our discussions with Mr. Weinmann was more than helpful to get additional knowledge about the current state of the technology and gain inspiration to come up with the alternative designs proposed within the frame of this work. I would also like to express my appreciation to Dora Akgul for her emotional support, helping to structure, iterating on ideas and questioning the possible improvements. I would like to thank my family both for their financial and emotional support throughout my studies including this dissertation. Last but not least, I would like to express my appreciation to Prof. Marta Ramilo Abrantes, Prof. Jorge Matos and Prof. Jose Falcao de Campos for enabling me to extend my thesis so that I could continue the experimental analysis and upgrade the design based on the extended experiments.

Abstract

Reducing the cycle time of the lithium-ion production, significant cost savings are possible contributing to make the electric vehicles the primary preference in the market. This work focuses on improving the cycle time of the electrode web conveyance unit in the poach cell production applying the single sheet stacking method. This system consists of processes from the point the calendered electrode material roll is unwrapped until its punched into individual layers. We reviewed a wide range of literature on battery manufacturing, web handling, and gripper technologies. Shelton's Beam Theory with emphasis on web dynamics created a framework for the design of the experiments carried out on this work. The experiments aimed to verify whether these principles would apply for the cathode and anode of the lithium-ion cells. Tension, velocity, misalignment angle, web span seem to have a strong correlation to the instabilities of the web. In regard to literature and experimental analysis, there is a compromise between product quality and manufacturing speed. Given the theoretical and empirical results, two alternative designs were developed to make improvements. These designs feature significant improvements in web stability. Besides the process is predicted to be completed around 38.3% faster in contrast to the reference technology. Besides, the linear motion identified as a bottleneck of the electrode processing unit was replaced with alternative approaches to improve the lead times substantially. Consequently, we compared the conceptualized designs on a theoretical frame. A plausible design is proposed as a result of this comparison.

Keywords

Lithium-ion, Production Technologies, Pouch Cells, Single sheet stacking, Electrode web

Resumo

A redução do tempo de produção no processo de fabrico de baterias de ião lítio é um desafio bastante atual e que preocupa a indústria uma vez que pode conduzir a poupanças significativas nos custos de produção. Essa redução terá um impacto significativo, por exemplo na implementação dos veículos elétricos no mercado.

Este trabalho visa implementar soluções que reduzam o tempo de processamento numa unidade de produção de eléctrodos para baterias de ião lítio do tipo “poach cell” onde é aplicado o método de empilhamento em folha única, i.e. deposição do material ativo sobre o colector de corrente em processo contínuo. O processo envolve o desenrolamento dos coletores de Alumínio e cobre, a deposição do material ativo e todos os processos complementares de calandragem e empilhamento.

Neste trabalho é feita uma revisão do estado da arte dos processos de fabricação de baterias de ião lítio e de todos os componentes associados ao processo, rolos e garras, por exemplo bem como o efeito de diferentes parâmetros processuais.

Foram efetuados ensaios numa montagem piloto e para estudar o processo utilizou-se a teoria do feixe de Shelton. Avaliou-se a sua aplicação quer ao processamento do ânodo quer do cátodo. Foram estudados diferentes parâmetros tais como: tensão aplicada, velocidade, largura de banda e ângulos de desalinhamento, e avaliou-se o seu impacto quer na qualidade do produto quer no tempo de fabrico.

Com base nos resultados foram propostas 2 soluções alternativas para o processo e que permitem introduzir melhorias no mesmo. As soluções propostas poderão reduzir em 38,3% o tempo de processamento relativamente à tecnologia atual. As soluções propostas permitem também ultrapassar algumas limitações inerentes à unidade de processamento e permitirão melhorar também a qualidade do produto. As soluções propostas foram comparadas com as soluções estado da arte e o seu impacto traduz-se por um decréscimo do tempo de processamento e a redução da probabilidade de imperfeições nos elétrodos.

Palavras-chave

Lítio-íon, Tecnologias de Produção, Células de Pouch, Empilhamento de folha única, Eletrodo web .

Table of Contents

List of Figures

List of Tables

List of Acronyms

BEV	Battery Electric Vehicle
CAD	Computer-aided Design
EV	Electric Vehicle
GUI	Graphical User Interface
HEV	Hybrid Electric Vehicle
ICE	Internal Combustion Engine
IRTM	Imaginary Resistive Tension Member
PET	Polyethylene terephthalate
SEI	Solid Electrolye Interface

List of Units

fps	Frames per second
rpm	Rotations per minute

List of Symbols

A	Cross sectional area
D	Flexural rigidity
E	Young's Modulus
F	Force
F_a	Force acting on the active material layer
F_c	Force acting on the colector
F_e, T	Tensile force
F_{lat}	Lateral force
F_{res}	Resultant force
F_{st}	Stabilizing force
k	Spring coefficient
L, l	Length
M	Moment
$M_{0,crit}$	Critical moment
I	Moment of Inertia of the web (I = tw^3/12)
Q	Resultant shear load
r	Radius
RM	Resistive member
s	Span of a bendable medium
t	Web thickness
V_{edge}	Web speed at the edges
V_{center}	Web speed at the centre
w	Width
ϵ	Strain

ϵ_{st}	Stiffness ratio
θ	Misalignment angle
θ_L	Critical misalignment angle
μ	Coefficient of friction
$\sigma_{bend,r}$	Stress due to bending radius
$\sigma_{bend,r}$	Stress due to bending radius

List of Software

Siemens NX 11	Design Software
Python	Analysis, post-processing and visualization of the experimental data
MATLAB	Test stand position control, collection of load cell data

Chapter 1

Introduction

This chapter introduces the motivation, objectives and structure of the work. Under these topics, we describe the importance of the field, expected outcomes, and pathway to reach the desired solution.

1.1 Motivation

Promotion of electric mobility does not only show a significant potential to reduce or even to eliminate the need for fossil fuels but also increases the second law efficiency of energy conversion to yield useful exergy (Serrenho et al., 2016). Technology should meet the requirements of the transport sector, making electric mobility desirable for consumers. Consumer tendency to deny any significant adaptation efforts challenges this transformation. The key performance indicators of the EV and HEV technologies are the safety, affordability, lifetime, the range of the vehicle and charging rate. These vehicles rely on energy storage systems. Latest improvements in the energy storage technologies show great potential to become the new driver of the transport sector.

EV sales data obtained from the U.S Department of Energy (2014) from December 2010 until June 2013, shows the market share of the EVs and HEVs jumped from 0.06% to 1.23%. The market share grew more than 20 times in less than three-year timeframe. According to Claire Curry (2017), the cost of lithium-ion batteries in the U.S went down from 1000$kWh to 599$/kWh in the same three years. In 2016, lithium-ion batteries contributed to 48% of the total cost of the BEV's. These data show the impact of the lowered battery costs in the transport sector.

Commercial availability of lithium-ion batteries is one of the most significant challenges the automotive industry has to overcome. In an attempt to tackle these challenges, sale price plays a dominant role in the market. Most of the research and development is focusing on a selection of more abundant materials. Cost intensity of the battery manufacturing processes is often overlooked.

Schlick et al. (2011) reported the cell production allocates 47% of the overall battery costs. Improving cell production in terms of productivity and reducing residual material is a challenge suppliers are required to overcome. Such improvement signifies a considerable cost reduction potential. Research and development in battery manufacturing technologies are fast becoming a principal instrument in the cost-effectiveness of the batteries and electric vehicles.

1.2 Objectives

A number of studies have reported different approaches to improve the electrode processing unit (Baumeister and Fleischer, 2014;Aydemir et al., 2017;Schröder et al., 2016b). However, these studies have not dealt with the mechanical behavior of electrode webs during transport in detail. This work focuses on the fundamental principles of the electrode web mechanics. These principles shape the design of the experiments and specify critical parameters to measure, observe and analyze during these experiments.

In light of the theoretical background and experimental analysis, two alternative designs are proposed. These designs improve the stability of the lithium ion single sheet stacking electrode processing line consequently improving the production cycle times. The plausible design is then nominated accounting for the relevant parameters defined through the research.

1.3 Structure

Including the introduction, the overall structure of this work takes the form of six chapters. Chapter 2 describes the existing technology of lithium-ion battery production and types of production methods dependent on the type of cell. Moreover, current converting technologies used to process web materials are reviewed. Besides, this chapter provides necessary information about lithium-ion battery chemistry, functional components and function. Types of cells are also reviewed in this section. Lastly, principles behind the web handling are introduced in this section mainly to build up a foundation.

Chapter 3 gives insights into the workflow structure designed to reach the objective. Besides, the experimental procedure used to get to the results is described. The experimental procedure is clarified in Chapter 4. The results obtained from the experiments are also presented in this section. Benchmarking is used to obtain favorable system components to propose two alternative design solutions.

Two design proposals are introduced in Chapter 5. Using benchmarking, a favorable design is proposed. Based on the experimental analysis, operational constraints are introduced to provide further improvements. Chapter 6 assesses the work and the results obtained from this work. Additionally, possible errors and overlooked conditions are interpreted. Foremost, an outlook is provided to suggest a possible framework for future work.

Chapter 2

State of the Art

This chapter provides information on the existing technologies in the making of lithium-ion batteries, feeding and gripper systems. Additionally, the test stand and lithium-ion production assembly developed in the Karlsruhe Institute of Technology Institute of Production Technologies (KIT wbk) is introduced. A foundational comprehension of lithium-ion batteries, mainly presenting the function, components and cell types of the lithium-ion batteries are presented. Furthermore, the fundamental aspects of web handling are introduced.

2.1 Production of Lithium-ion batteries

Li et al. (2017) reviewed forty studies in order to identify consumer intentions to adopt battery electric vehicle technology. Their overview unfolded the notable challenges the automotive industry has to overcome. These are driving range, charging time and purchasing cost of the batteries. It is clear that all three of these significant obstacles are associated with the advances of lithium-ion technology. Lithium-ion battery production is predominantly relevant considering the improvement potential of these aspects. Battery production consists of raw material production, electrode production, cell production, and module assembly.

Raw material production starts with grounding, mixing and conditioning the raw material to form an active material slurry. The slurry is then coated onto a metal foil which is dried afterward and calendered respectively. Electrode strips are wound up into rolls to be transported onto the cell production line.

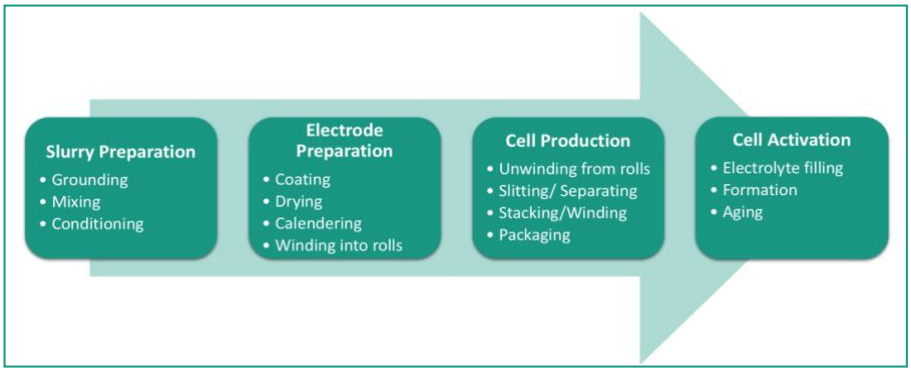

Figure 2.1: Manufacturing steps of the lithium-ion battery.

Both electrode strips and separator are unwound to be slit, separated and stacked or re-wound. Cell units are contacted onto each other, welded, packaged before electrolyte is filled. Subsequently, formation and ageing processes are performed. The final step is the module and pack assembly. After the cells are inspected and tested, they are aligned according to the power and voltage requirements either in parallel or in series. Alignment and placement of these cells are performed under dry and clean room conditions. The demand for EVs is expected to rise vigorously. Thus, integration and automation of the processes above have a remarkable impact on cost reduction (Maiser, 2014).

The production processes are described in depth in the following sections. The content of the processes follow the order shown in Figure 2.1.

2.1.1 Slurry Preparation

Description of the following sections are based on an anode active material lithium graphite (LiC). Graphite is preferred since it is a commercially accepted anode active material. Except for different chemical compositions, the procedure of cathode sheet preparation is similar.

The chemical compounds used to form the cathode are mixed until all of the components are homogeneously distributed. Homogeneity of this mixture can be secured using a multi-step mixing

process. Carbon black is added to the mixture when the material is still in the dry state. The powder is slowly mixed until it is homogeneously distributed. Addition of the carbon black improves conductivity. Additives, binder, thickener, and solvent is then added and mixing speed is increased gradually until the mixture is evenly dispersed (Baunach et al., 2016).

2.1.2 Electrode Web Preparation

The slurry is coated on a thin aluminum foil on the cathode and thin copper foil on the anode. Coating delivers uniformly distributed active material with minimum thickness variances. The coated material is then dried in order to remove the solvent. This step enables the formation of gaps which host the lithium ions during the operation (Singh et al., 2015).

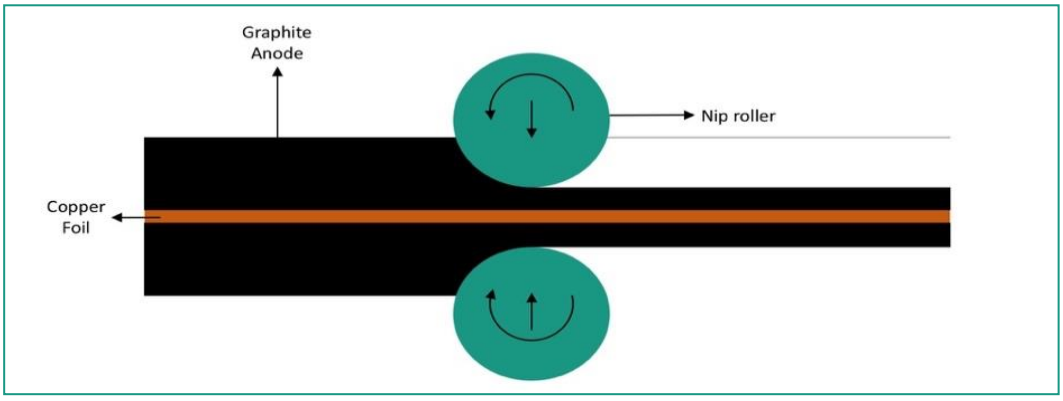

Figure 2.2: Calendering of the negative electrode active material.

The electrode is calendered using a compactor. A compactor is a nip roll that presses coating on both sides. Figure 2.2 shows this process. After calendering is completed, the material is rolled into a cylindrical form to be transported to the cell production.

Compaction can be performed under different compression rates depending on the force applied by the nip roll towards the foil. The primary intent of this process is to decrease the porosity and increase the density of the lithium-ion battery. Besides, the adhesion is improved at this step which hinders delamination problems (Meyer et al., 2017).

2.1.3 Cell Assembly

Cathode, anode, and separator rolls are unwinded to be processed in the cell production unit. Processes of prismatic hard-case and cylindrical cells differ compared to the pouch cells starting from the compound assembly.

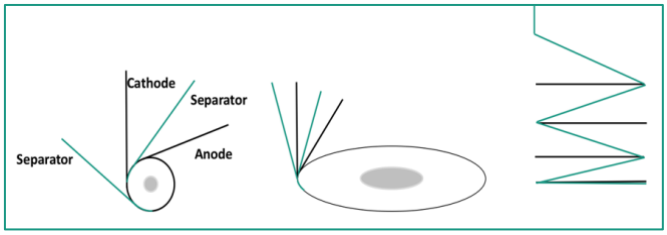

Figure 2.3: Assembly of the cylindrical cell (Left), prismatic cell (middle) and pouch cell (right).

Two different methods are used to obtain the pouch cell in the sequence of positive electrode-separator-negative electrode-separator. The first method involves cutting single sheets for both electrodes and separator either with the aid of laser cutting or die cutting equipment. Then the single sheets of electrode and separator will be placed in the sequence above. This step is called pick and place operation as each sheet is picked and stacked on top of the previous layer. This method is addressed in more detail in 2.4.3.

The alternative method involves a continuous sheet of separator enveloping the single sheet electrodes. Enveloping is realized by folding in the separator in z form. Hence, the method is called the Z-folding method. On the other hand, winding is used to assemble the hard-case prismatic and cylindrical cells. All four layers are winded simultaneously forming the layered structure of the cell. All four strips are cut when the desired cell size is reached, ready to be placed into the housing. The winding of a cylindrical cell and hard-case prismatic cell and Z-folding of the pouch cell is illustrated in

Figure 2.3.

After the layered structure is obtained, all three types of cells go through the tab welding procedure. Connectors are welded onto each other to secure an electrical connection between the assembled electrodes. This procedure is performed either by ultrasonic, laser or resistance welding.

The housing of the cylindrical cells and also for the hard-case prismatic cells are either deep-drawn aluminum or welded steel which provide ruggedness. The wounded cell needs to be joined to the housing. Joining is critical to avoid the material damages due to inertial motion inside the housing. Pouch cell housing is a deep-drawn aluminum-polymer-compound foil which provides design flexibility. The stacked layers of the pouch cell can be directly placed onto the lower half of the housing without requiring any joining. The upper half of the housing is then placed onto the lower half, and three edges are sealed (Schröder et al., 2017).

2.1.4 Cell Activation

The electrolyte is filled into the cells using an injector. The amount of electrolyte filled inside the cell should be carefully measured. Too little or too much electrolyte cause malfunctions and degradation of cell performance. As soon as the filling is completed, the cell should be sealed (Westermeier et al., 2013). For the pouch cell, before the 4th edge is sealed, the air inside is evacuated to depressurize the swollen cell. Moreover, shrinking housing forces the electrolyte to percolate through the pores of electrodes (Schröder et al., 2017).

The battery is charged and discharged for at least one complete cycle. This step is also called formation. “Formation” refers to the formation of the SEI layer which is described in 2.5.1. Pouch cells require extra care for these steps as they may swell during these processes due to gas formation. The gas is removed by removing the extra pouch and resealing the housing. The prismatic and cylindrical cells are not affected by this since they have a built-in degassing valve. Finally, the ageing process is performed. The purpose of this process is to verify the performance and properties of the cells. The battery is operated under a range of temperatures (Maiser, 2014).

2.2 Feeding

Components of the feeding system in the existing applications are reviewed in order to gain an insight into possible applications that can be applied to the electrode processing line. Design of the improved system primarily features the transport system which is reviewed in this section. Selection criteria is defined based on the test results which is described in chapter 4.1.

2.2.1 Driven and Idle Rolls

2.2.1.1 Contact Rolls

Contact rolls are operated as driven and idle rolls. Driven rolls require a connection to the roll to transmit the rotation. A coupling is used to make this connection. The coupling connects the roll shaft to either the motor directly or an extra belt is used which is driven by the motor on one side, drives the roll shaft on the other side. A proper bearing arrangement is necessary to transmit the axial and radial loads to the housing. Rolls are designed and manufactured on the basis of two parameters: the diameter and the material of the roll.

Roll diameter is often specified by comparing the diameter with the roll width. The ratio of roll width to diameter is generally less than 16. This criterion limits the maximum diameter of the roll. Roll width is determined based on the web width; roll width is chosen as small as possible allowing clearance of the web from both sides. The larger the web width and diameter, the more difficult it is to drive the rolls. Rotational moment of inertia induces this behavior. Mass and square of the radius are directly proportional to the moment of inertia. The diameter is also limited by the bending radius. The following formula is applied to calculate the stresses acting on the web due to the bending radius:

$$\sigma_{bend,r} = \mu \frac{F_{res}}{2r arcsin\left(\frac{s}{2r}\right) t} \text{ (Schmits, 2018).} \qquad \text{Eq. 2.2.1}$$

Stainless steel and aluminum rolls are frequently used in web handling applications. Alternatively, carbon fibre rolls are also available. Aluminum and stainless steel roll costs are comparable while carbon fiber rolls are more costly. Carbon fiber rolls are lightweight. Lighter roll weights provide less rotational inertia and higher critical speeds (Smith, 2012).

The coating layer is an essential part of the material selection for the contact rollers. To avoid air entrainment induced slip, coefficient friction is a limiting factor in the roll material selection.

Coating material sustains the capability of sufficient traction and avoids instabilities. The friction coefficient should not be too high since excessive frictional forces lead to scratches on the web surface. Furthermore, the coating material should not have reactive properties when in contact with the web material. Otherwise, the web and the coating material is degraded (Ünlü and Atik, 2007).

2.2.1.2 Contact-free Rolls

Contactless handling principles facilitate contamination-free transport and positioning of limp and delicate materials. Magnetic levitation, electric levitation, and aerodynamic levitation are some of the techniques to realize this type of conveyance. Magnetic and electric levitation is limited by material conductivity whereas aerodynamic levitation is constrained by material porosity and permeability (Delettre et al., 2012).

New Way Air Bearings introduced commercial application contact-free web handling rolls, namely Air Turn rolls. Air Turn rolls operate according to the aerodynamic levitation principle. Van Dam et al. (2014) tested the functionality of this product with the results indicating significant potential for limp web handling applications. Tests were carried out with $150\ \mu m$ thick, $300\ mm$ wide PET foil as well as $100\ \mu m$ thick, $250\ mm$ wide stainless steel web under a variety of web tensions at a supply pressure of 3 and $4\ bars$. The results are depicted in Figure A. 1 and Figure A. 2.

The stainless steel web could be operated up to $200\ N$ foil tension with a fly height of slightly below $100\ \mu m$. The testing phase also showed improvements in web stability behavior. An improved stiffness was achieved during the experiments, which can be justified with the air film layer forming an even force distribution over the foil. Surprisingly, the air film delivered a wrinkle removing characteristics. One possible explanation for this flattening effect may be the spreading caused by re-stiffening of the foil. Further experiments have been proposed to investigate and verify this behavior.

The Air Turn can also be used to replace the dancer applications. Dancer systems is discussed in 2.2.4. It is notable, however, that one of the significant problems encountered with dancer operation is the inertial forces exerted on the web through acceleration and deceleration. Rotation-free operation of Air Turn eliminates rotational inertia of the dancer roll. Effective implementation of the Air Turn eliminates the necessity of a complicated control mechanism required to balance inertial forces.

The Air Turn roll is tested with the stainless steel foil up to $83\ mm/s$ (Schröder et al., 2016b). Moreover, improvement beyond this speed is hypothetically achievable using this equipment. The electrode web should also be examined at high speeds in order to observe and verify the functionality of the Air Turn in the lithium-ion battery production.

Figure 2.4 displays the airflow path and web direction. Airflow approaches the web perpendicularly from the core of the Air Turn towards the web. This path allows a lifting force keeping the web away from the roll. Concave radial air bearings and the controllability of the web are described in greater detail in chapter 2.2.2.

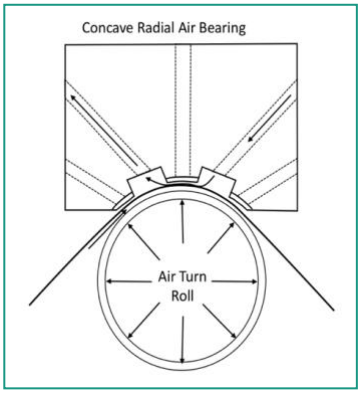

Figure 2.4: Air Turn roll and concave radial air bearing (Devitt, 2010)

2.2.2 Web Guidance

Web guidance systems adjust the lateral position of the web. Web guide is controlled through electro-mechanical or electro-hydraulic actuation. The actuator moves the guide, shifting the roll and hence the web. Ultrasonic or optical sensors are used to adapt closed-loop feedback control strategies. Based on the lateral position detected by sensors, the guide is directed. Web guide is essential for the electrode processing unit to adjust the lateral position of the roll, so the electrode is precisely cut according to the specifications.

If the guide is designed to shift one of the rolls keeping the others at a standstill, the shift results in misalignment angle between the consecutive rolls. If this angle is beyond the critical misalignment angle, excessive lateral movement results with wrinkles or slackness on the web edges. These disturbances cause permanent damages to the material. Selection, implementation, and control of web guides are therefore critical (Seshadri and Pagilla, 2012). In roll-to-roll systems, guide mechanisms are implemented on the unwinder, winder or between rolls. Unwinding and rewinding operations can be guided by terminal guides, while intermediate guides are used to navigate the processes between the unwinding and rewinding (Hawkins, 2003).

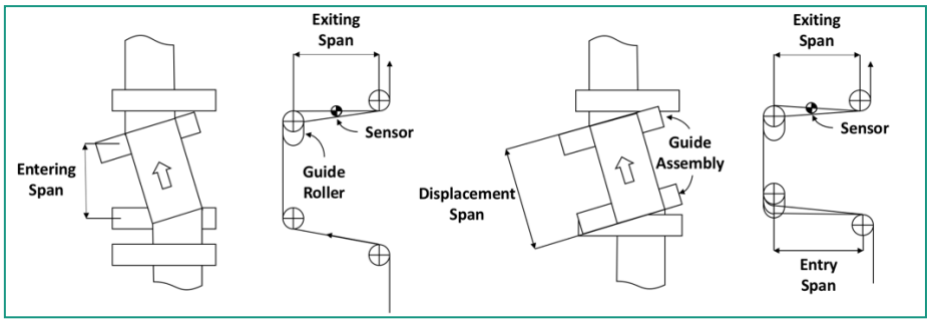

Figure 2.5: a) Steering Guide b) Partial Displacement guide (Shelton, 1986)

Intermediate guides are conventionally implemented in the form of partial displacement guide (offset-pivot guide) or steering guide (remotely pivoted guide) mechanisms. Steering and displacement guide employs the perpendicularity principle for lateral adjustment of the web. The steering guide is designed to adjust the offset angle of the forthcoming roll. This principle allows the roll to align itself perpendicularly

to the web by forcing the web to move sideways. However, a long span is required to ensure a stable operation.

Partial displacement guide is better suited for a relatively shorter entry span. Unlike steering guides, entry and exit spans are parallel to each other, the web enters and leaves the guide at a vertical angle. The lateral displacement is obtained through pivoting the guide rolls around a reference position to reposition the web (see

Figure 2.5). As the displacement is obtained without bending the web, displacement guides cause fewer wrinkles than steering guides (Shelton, 1969).

The unwind guide facilitates lateral web positioning moving the unwinder stand. This method allows web adjustment on an early stage, ensuring continuous alignment before the web enters the process. The same principle can be applied integrating the desired portion of the converting system into a single stand. Since this principle is also similar to the displacement guide, it is designated as a complete displacement guide. This system enables efficient positioning without dealing with non-perpendicularity between the unwinding stand and rolls. The lateral positioning adjustment is carried out via a position sensor attached to the stationary machine frame, recording the current position. Managing the data obtained from the sensor, the controller commands the linear motor to shift the stand laterally (Hawkins, 2003).

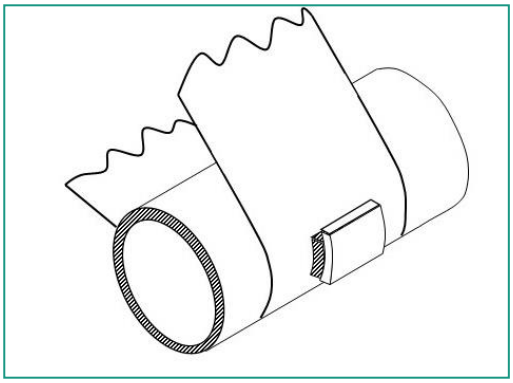

Figure 2.6: Concave Radial Air Bearing

Another alternative approach for lateral adjustment is a combination of Air Turn and concave radial air bearing. Air Turn rolls were discussed earlier in section 2.2.1.2. The concave radial air bearing is also supplied with an airflow creating a counteracting air film against the Air Turn roll. Applying viscous shear to this layer, motion control is obtained. A pressure exerted on the air bearing in a particular direction results with a bias of the bearing. This bias pushes the web laterally in the desired direction. If the air bearing gets closer towards the web on one side and gets further away from the other, airflow pushes the web towards the opening hence allowing motion. This principle can be applied in both lateral and longitudinal directions. Consequently, using one concave radial air bearing, both lateral and longitudinal positioning control is possible (Devitt, 2010). According to Devitt et al. (Devitt and Allen, 2014), a single $50\ x\ 100\ mm$ concave radial air bearing was capable of applying $30\ g$ of shear force with a resolution of 1/100th of a gram in $50\ mm$ direction. This enables precise control of lateral and longitudinal positioning.

2.2.3 Web Spreaders

The main purpose of the web processing assembly is to convey the web without degrading the material quality. To meet this objective, the web should be flat throughout the process. Wrinkle formation is an inevitable occurrence for web converting equipment with instabilities. Causes of the wrinkle formation are addressed in section 2.6.3.1 (Hawkins, 2003). Wrinkling and similar material imperfections are decisive for the battery cells concerning performance and safety. Presence of fold-over wrinkles can disrupt the ion-flow paths hindering the battery performance. Besides, a formation of sharp edges caused by these defects also risks the mechanical integrity of the separator. During degassing, gas formations inside the cell are sucked out and housing shrinks towards the stacks applying compression stress induced by form closure. Sharp edges may spike the surface of the separator, which poses a vital safety risk in the form of short circuits. Spreader rolls provide re-flattening of the web so that the wrinkles are removed avoiding potential safety hazards.

Spreaders temporarily stretch out the web in the lateral direction. Spreading is accomplished with adequate traction. Baggy webs are conflicting when operating with the spreaders because spreaders cannot exert sufficient traction forces on the web. Thus, an acceptable amount of tension is essential to avoid bagginess so that spreaders can catch enough traction to stretch the web in the lateral direction (Land et al., 2010).

Concave, bowed and extended rolls are commonly preferred in spreading applications. However, as the web gets thinner, the risk of wrinkle formation increases. One possible explanation could be the decreasing flexural stiffness, not being able to counter against the shear or cross-directional compressive loads (Roisum, 2003).

2.2.3.1 Concave Rolls

As the name implies, concave rolls have elevated edges and lower center which forms a curved shape. The change in diameter in the direction of the edges forces the web to move further on the edges than in the center. As a result, leading web edges and lagging center force the wrinkles out. Different web velocities across the roll surface are shown in Figure 2.7. The tension profile across the web is also similar to the velocity profile. The steepness of the arc is a decisive factor defining the aggression of the spreading characteristics (Roisum, 1998).

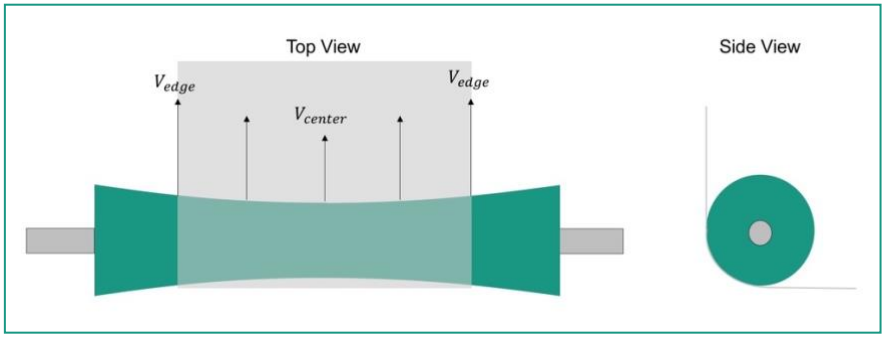

Figure 2.7: Concave roll top view (left) and side view (right).

Web elasticity is an essential measure for applicability of the concave rolls. This is due to an indirect spreading effect, as the spreading is obtained by the stretching the web edges longitudinally. Excessive concavity forces the material to overshoot the yield point. Accordingly, plastic deformation leads to reduced material quality (Smith, 2012).

2.2.3.2 Bowed Rolls

Bowed rolls consist of an axle shaft and a roll which are both bent towards the machine direction. The parabolic shape of the rolls requires a proper load distribution to the shaft. Ball bearings across the whole shaft handle this load distribution. A proper bearing arrangement is necessary to extend the service life of the rolls as well as to avoid mechanical failure during the operation. Optionally, a rubber sleeve can be fitted on the roll surface. The rubber cover is used for two reasons: To dampen the force transmission to the web which prevents scratching, and to obtain slip-free traction (Roisum, 1998).

As depicted in Figure 2.8, the web approaches the bowed roll at an angle of $90°$. This principle forces the web to stretch. Most of the spreading action takes place between the preceding roll and bowed roll. The entry span is critical as it is a determining factor for the amount of spreading. On the other hand, the exit span should be kept as short as possible to avoid the web shrinking back to its former wrinkled state.

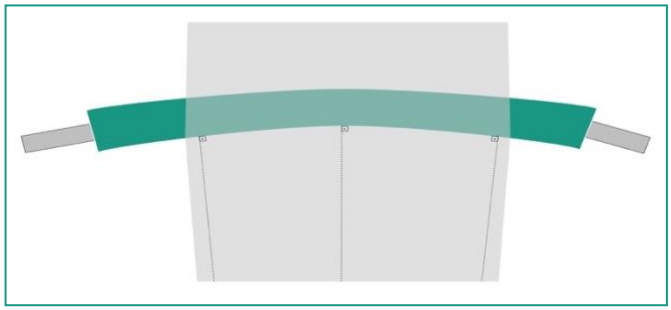

Figure 2.8: Illustration of a bowed roll

Bowed spreaders provide a suitable solution for webs exposed to frequent and severe wrinkles. Spreading behavior is intensive. However, the trade-off between spreading aggressiveness and high tension distribution poses challenges particularly for webs with low yield strength. An excessively aggressive spreading exert high lateral loads on the web resulting in a tear-off (Hawkins, 2003).

2.2.3.3 Flat Expander

Flat expander rolls are fitted with an adjustment screw, a linear center shaft, a disk support tube, stacked rubber disks, and a cover. The Adjustment screw pivots the collar and disk support tube. The web enters the roll, where the rubber sleeve is shorter as illustrated in Figure 2.9. The stretching starts before the web enters the roll as each IRTM tends to approach perpendicular to the roll axis. The web leaves the roll where the rubber sleeve is longer. The stretching continues until the web exits the roll. Rotation of the roll allows the sleeve to be stretched laterally; the web expands together with the rubber sleeve due to traction between the sleeve and web (Damour, 2016).

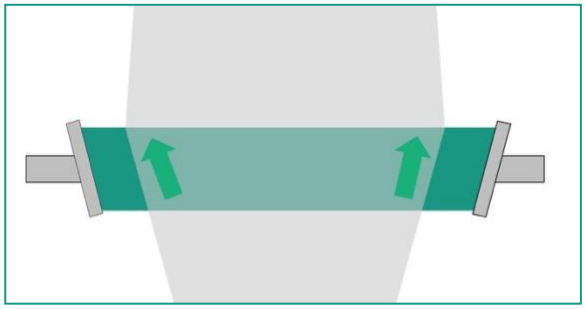

Figure 2.9: Flat Expander Illustration and direction of forces.

Linear surface profile ensures uniform force distribution across the web. The rubber surface delivers additional traction, avoiding the scratches at the same time. In contrast to the rolls described previously, the flat expander gives the freedom of adjustability. Spreading adjustment is possible even during operation. However, the angle of the adjustment disk should be identical on both sides; asymmetry can lead to additional wrinkles on the web. On the other hand, at high speeds, the centrifugal force sways the bands away from the roll. Thus, the operation speed is limited in the slat expander spreaders (Roisum, 1998).

2.2.3.4 Angled Nip Rolls

The nip rolls are classified into two working principles: air loaded and friction contact. Air loaded nip rolls apply vacuum whereas friction contact nip rolls apply friction to stretch the web. Both types come in pairs which are fitted at the web edges. Both sides can be adjusted independently. This flexibility gives the choice of adjustment based on the type, orientation, and direction of the wrinkles. Especially for the asymmetrical instabilities, nip rolls can be adjusted such that one side can spread out more than the other side simply modifying the nip angle. However, for precise positioning applications like printing, asymmetric angled nip roll alignment is not recommended since it also alters the lateral position of the web. In such cases, additional web guiding may be used to compensate for the lateral motion.

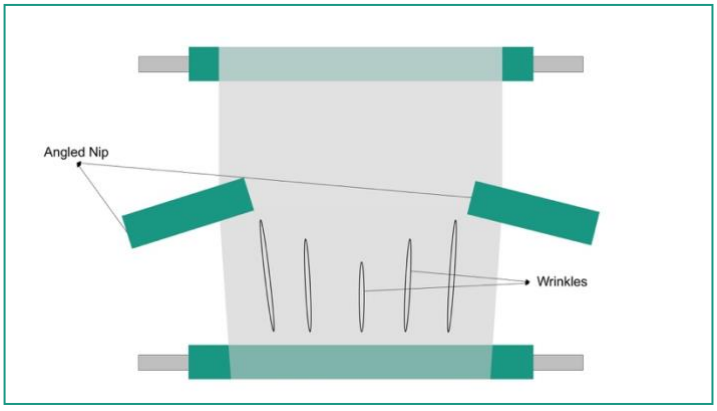

Figure 2.10: Angled nip roll spreader.

For air loaded nip rolls, the load on the web can be adjusted via a pressure regulator modifying the suction pressure. In contrast, friction contact nip rolls are less flexible considering the load variation. However, load adjustment is still possible through the selection of the surface allowing additional traction or by adjusting the distance between the nips. Furthermore, the angle of the nip roll determines the

direction of the load applied on the web. Compared to other spreaders available, angled nip rolls are characterized by high flexibility and adjustability in the direction of the load and aggressive spreading.

Figure 2.10 illustrates the nip roll spreading a wrinkled web. In this case, the web is symmetrically wrinkled. Thus the nips are adjusted also using the same angle about the approaching web. In other words, the web tends to travel perpendicular to the axis of the nips spreading the web equally on both sides. This results with IRTMs stretching in just the opposite direction as the cross-directional compressive or shear loads (Damour, 2017).

2.2.4 Dancer

Fluctuations and instabilities are inherent to web conveying systems. To minimize these disturbances, specific equipment should be used with appropriate control strategies. Suitable tension control measures have a significant capability to assure stable operation at higher speeds. Besides tension, velocity is also taken into account for tension attenuation, since tension fluctuations also result in velocity fluctuations and vice versa.

Dancer systems are designed for either tension measurement or tension control to minimize tension attenuations. Tension measurement is obtained by measuring the dancer roll displacement. Tension regulated by controlling the dancer position. These mechanisms are employed in order to minimize tension variations.

Dancer systems are classified according to the directness of the control system. The passive dancer arrangement incorporates indirect tension control. With an air cylinder, counter pressure is applied on a pivot or a linear slide which then transfers the load to a floating dancer roll. Active dancers operate by controlling the translational velocity. The closed-loop feedback control uses the tension measured by a load cell downstream to the dancer (Dwivedula et al., 2006).

Selection of the correct dancer roll arrangement depends on a number of factors. The roll mass is critical as the movement of the dancer generates oscillations induced by inertial forces. Besides, even without the consideration of the inertia, the mass of the dancer roll should be half of the tension desired on the web since the web carries the roll on two ends (Kuribayashi and Nakajima, 1984). Additionally, tension disturbances should be characterized in order to make an appropriate selection of the dancer system. The combination of periodic tension disturbances and high operational speeds require tension attenuation at larger ranges as the tension fluctuations are directly proportional to the speed in such cases.

On the one hand, active dancers are capable of tension attenuation in a wide frequency range. This is due to the ability to adapt different controller strategies for the given configuration. On the other hand, passive dancers are characterized by a better tension attenuation capability of web materials with high elastic modulus (Dwivedula et al., 2006). However, at higher velocities passive dancer are not able to keep up with the tension attenuation.

2.3 Gripping

Electrode processing unit consists of three main steps: Feeding, gripping and cutting. The function of gripping devices is critical in electrode handling. Electrode sheet must be transported and fixed past the die-cutting unit so that the pre-outlined sheet can be cut. For certain applications, grasping is complicated by the fact that the material has a porous structure for both the anode and cathode. Fast, robust, clean and damage free gripping are pre-requisites to obtain a standard quality.

Various studies focused on limp material grasping technologies. These studies revealed the complexity of gripping primarily due to the unpredictable behavior of the limp materials (Seliger et al., 2003;Löchte et al., 2014;Fantoni et al., 2014). Gripping consists of the following steps: approaching, making contact, tightening through force build-up, securing, moving and releasing (Fantoni et al., 2014). As presented in Figure 2.11, grippers are classified under three physical force transmission principles: force closure, form closure, and material closure (Stephan, 2001). From this point on, the object to be lifted/moved is referred to as object and the component that grips is referred to as gripper.

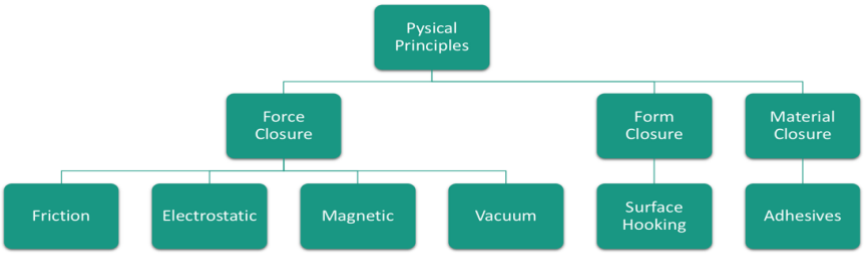

Figure 2.11: Working principles of grippers.

Each method is compared and evaluated in chapter 4.3, where each step is to be analyzed quantitatively to find the most appropriate method. For this comparison, the following factors should be considered: non-damage gripping, contamination, speed, gripping reliability, holding forces, material and form flexibility (Seliger et al., 2003).

2.3.1 Force Closure

Clamping grippers provide the gripping force by mechanically tightening the objects. The degree of freedom of the object is constrained by the frictional forces exerted by the gripper. The coefficient of friction among the contact surfaces plays a critical role in preventing slippage during the gripping process. This situation has a significant influence on the reliability aspect. Besides, since the frictional forces are generated by compressive stresses, delicate surfaces can be easily damaged (Fantoni et al., 2014).

Suction Grippers are vacuum induced grippers. In other words, the holding force is generated through the pressure difference between the atmospheric pressure and negative pressure of the suction gripper chamber. Even surfaces are optimal to operate these type of grippers (Fleischer et al., 2016). Suction grippers are limited to airtight materials. Vacuum enhancement is required to handle the materials with permeability reliably (Fantoni et al., 2014).

Magnetic gripping is limited to ferromagnetic materials. The surface of the material needs to be even in order to accomplish a reliable holding performance. Suction and Magnetic grippers are capable of gripping without damaging the material since the forces acting on the material are evenly distributed and not concentrated in specific areas (Pham and Yeo, 1988).

Electrostatic gripping is achieved by providing an electrostatic force between the gripper and object. The object and gripper are exposed to counter voltages. This opposition results with forces of attraction between the object and gripper. Hence the object is lifted. The gripping force depends on the conductivity of the object and amount of the voltage applied. If the current flows through the object which is not a good conductor, the material starts heating due to resistance. Excessive heating of the object may cause permanent damages. Another issue about this method is the particles in the surroundings attracted by the electrostatic forces. Contamination problems may arise using this principle (Heiland, 2003). However, it should be considered that gripping can be fulfilled without causing any mechanical damages to the material. Moreover, the object can be gripped and placed to the point of delivery with relatively high accuracy (Fantoni et al., 2014).

2.3.2 Form Closure

Needle elements facilitate a reliable material grip by penetrating the object from multiple directions. Since penetration is necessary to provide gripping by form closure principle, the objects to be gripped usually are limited to materials like fabric, cloth, and fibre composite materials. These materials are characterized by high porosity and flexibility. Hence, needle penetration does not damage the object (Giuseppe, 2011). Delicate materials such as thin metal foils are not suitable for needle gripper applications since the needles can puncture the material destructively.

2.3.3 Material Closure

Adhesives are the most frequently used gripping method that works with the material closure principle. Adhesives can be used in a wide range of applications; they are abundant, cheap and robust. Moreover, even force distribution is rather simple even for materials with uneven surfaces, as the adhesives have the ability to access the small porous structures. However, since the gripping force is enabled by chemical bonds, the removal of the adhesives is detrimental to the object. Besides, this approach features the addition of chemicals making it unfavorable for the objects requiring contamination-free environments.

A second option for material closure gripper is hydro-adhesive gripper. This gripper is equipped with a Peltier element which is capable of freezing water instantly. A nozzle is used to atomize a small amount of water onto the object. The built-in Peltier element freezes the water creating a physical bond between the gripper and object. The object can be released using pressurized air which heats up the ice melting it to liquid form. This gripper is characterized by its ability to exert a high amount of forces without damaging the object (Seliger et al., 2003).

2.4 Roll to Sheet Electrode Handling

2.4.1 Battery Performance

Common problems encountered in web processing are discussed in chapter 2.6.3. This section is dedicated to the aspects of battery safety, performance, and quality when these problems are present. Jia and Li (2016) investigated the effects of wrinkling on mechanical performance on the negative electrode substrates under cyclic charging and discharging. They used theoretical and finite element analysis in order to study the performance of the anode substrate. Their work revealed that the charge-discharge cycle induced periodic wrinkling mechanism.

In the event of extensive charging cycles, the wrinkling mechanism leads to plastic deformation and ultimately severe necking bands. While these findings are limited to the wrinkle formation only during charging and discharging, wrinkling formation can initiate crack propagation and leads to irreversible capacity fading. Wrinkling formation during handling of the electrode is not necessarily cyclic. However, it certainly cannot be disregarded. In both scenarios plastic deformations are induced by wrinkling. Thus, the formation of wrinkles due to charging-discharging cycles evaluated on these experiments imply similar consequences as the wrinkles formed during the electrode handling (Jia and Li, 2016).

2.4.2 Mechanical Characteristics of the Electrode Sheets

Aluminum and copper are used as cathode and anode current collectors respectively. According to Bonatti and Mohr (2016), Sahraei et al. (2015) and Wang et al. (2018), aluminum foil used in lithium-ion batteries show anisotropic characteristics. On the other hand, their findings showed that the Copper foil used as a negative electrode current collector is isotropic.

Active materials for the cathode and anode should also be considered to assess the mechanical characteristics of the electrode web. Zhang et al. (2017) investigated the contribution of the active layer for the electrodes under tensile loads. The porosity of the active materials causes discontinuous interfaces. The properties are strongly dependent on the current collector. However, all layers (one collector and two active) should be considered to define the effective response of the web. For cathode and anode, this correlation can be introduced as follows:

$$F_e = 0.1F_a + 0.9F_c \qquad \text{Eq. 2.4.1}$$

F_e is the tensile force whereas F_a and F_c are forces acting on the active and collector layers respectively.

2.4.3 Single Sheet Stacking Unit at wbk

Single sheet stacking was briefly described in 2.1.3. This section describes the process chronologically. Each step is expressed from the point where the active material is coated onto the current collector foil until the stacking is completed. The processes refer to the single sheet stacking unit developed in Karlsruhe Institute of Technology, Institute for Productions Sciences.

As described in 2.1.1, the active material is applied to the current collector foils, then dried and calendered. The strips are then wrapped into material rolls to be processed in the single sheet stacking unit. The components associated with the following steps are marked in Figure 2.12 and Figure 2.13. The numbers are given in parenthesis indicating the corresponding component in the Figure 2.12.

Initially, using a servo motor driven mandrel ('**1**'), electrode rolls are unwrapped. With the help of an idle roll ('**2**'), the web is transported through a dancer roll system ('**2**'). The dancer roll is attached to a cylinder. The cylinder is supplied with a tension set point. For small tension differences, continuous motion of the dancer is avoided by applying pressure on the cylinder. Change in tension presses the dancer roll and counteracts the cylinder pressure. Dancer roll moves until the pressure can balance the web tension pushing the roll in the opposite direction. The passive dancer system naturally adjusts the position of the dancer.

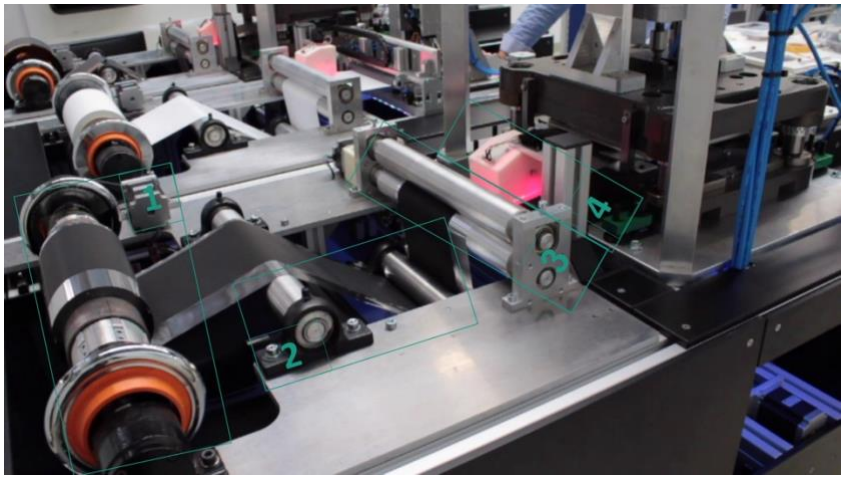

Figure 2.12: Wbk single sheet stacking unit.

After the dancer roll, nip roll pair ('**3**') provides traction and translates the web with 90 degrees. The web is then introduced to the die-cutting unit. The position sensor ('**4**') measures the edge position of the active material. In case a precision error is present, entire converting equipment is mounted on a stand which can be laterally controlled with another servo motor coupled with rack and pinion assembly. This mechanism is essential to obtain a clean, precisely cut electrode sheets.

The web is **fetched** with the help of a vacuum gripper ('**5**') and **pulled** past the die-cutting unit ('**6**'). After this step, the web is clamped from both ends. Then the electrode strip is cut into a single sheet. The single sheet is moved to the stacking compartment with the help of another vacuum gripper. On the other hand, the residual material is removed as the gripper fetches the end of the electrode.

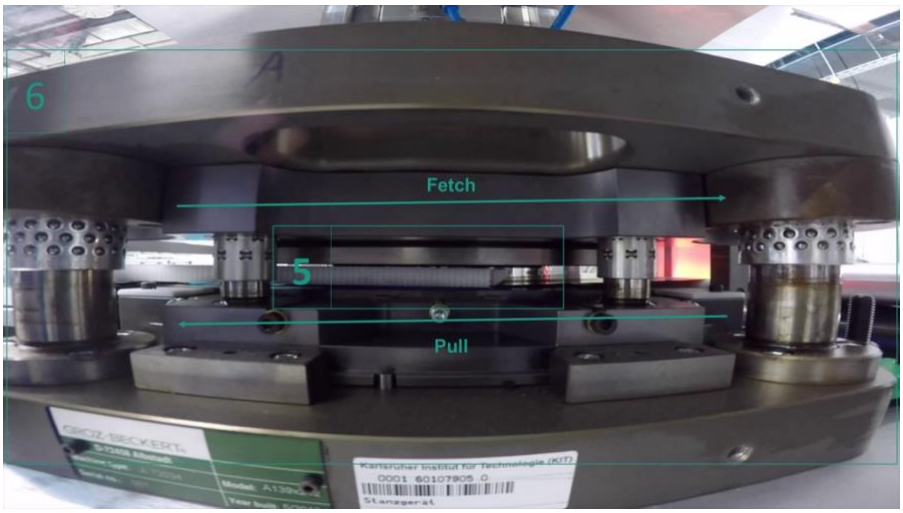

Figure 2.13: Gripper moving through the die-cutting tool to fetch the material.

The separator is also transported in the same manner as the electrode strips. It is also positioned processing the data gathered by the position sensor and captured with the help of a vacuum gripper. The pick-and-place assembly with a vacuum gripper head holds the separator on the place until it is cut by a sharp blade that moves in a lateral direction going through the separator material. The separator in single sheet form is then transported to the pick and place assembly where it is placed on top of a cathode or an anode. Before the vacuum gripper releases the separator sheet, the mechanical grippers are engaged to hold the material in place at four cross-directional locations. This procedure is repeated until the desired number of anode-separator-cathode-separator stacks are collected to form a full cell (Baumeister, 2017).

2.4.3.1 Identification of Potential Issues

Process and system components should be examined, before seeking for improvement possibilities or designing experiments. Bottlenecks are critical in identifying potential problems. All measures subject to deterioration of stability and/or congestion within the cycle are identified in this section. For simplicity, the system is divided into two parts: unwinding and collection assembly. Unwinding assembly consists of system components that interact with the electrode before it enters the die-cutting assembly. As the name suggests, the collection assembly collects the residual material after the single sheet is removed by the gripper within the die-cutting assembly.

The total cycle time required to obtain electrode sheets from the material roll is shown in Table 2.1. The linear motion of gripper as it grips the electrode web and moves out accounts for more than 67.6% of the total cycle. Thus, the gripper motion has considerable potential for improvement. The gripper to accelerates, decelerates and come to a standstill twice only to bring the web to the position in which the residual material is removed and the individual sheet is withdrawn. Inefficiencies through this step can be minimized changing the motion principle.

Table 2.1: Time period of each process in the single sheet formation of electrodes.

Process Name	Time (s)
Die Cutting Down	0.32
Die Cutting Up	0.44
Handling On	0.55
Handling Off	0.47
Clamping Down	0.15
Clamping Up	0.47
Vacuum Gripper In	2.84
Vacuum Gripper Out	3
Vacuum On	0.2
Vacuum Off	0.2
Total	**8.64**

Unwinding assembly is subject to stability issues that limit the handling speed and quality of the electrode sheets. Instabilities degrade the web material simply exerting unwanted loads through the material. There are several possibilities that require a further evaluation supported by theoretical explanations: Firstly, the friction between the aluminum rolls and the web may cause shear loads. Additionally, the rolls should be parallel, beyond a certain degree the misalignment angle also results with shear stresses on the web. If the shear loads exceed the material stiffness limits, the material starts folding. Compressive loads exerted on the web by the rolls then transform these folds into permanent wrinkles.

Secondly, despite the dancer mechanism is designed to provide a more stable handling environment obtaining tension attenuation control, the mechanism itself can cause additional instabilities due to a complicated control mechanism, and lagging adaptation mechanism. In addition, operating the web at elevated speeds cause speed difference between the web and roll. This risks the stable operation hence is a constraining factor for faster operations. Lastly, the aluminum rolls wear out over time, particles depositing on the web surface is a potential source of safety hazards on the lithium-ion cell.

2.4.4 Electrode Web Test Bench at the wbk

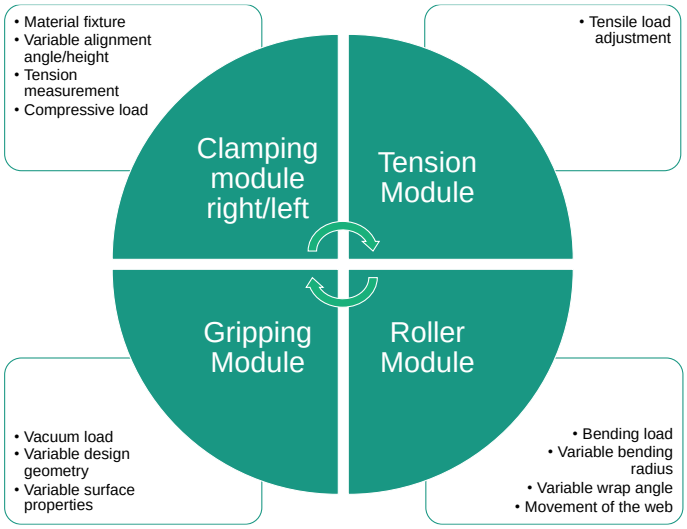

Figure 2.14: Elements of the test stand at wbk

The electrode test bench at the wbk was designed to facilitate a variety of experiments on the electrode web under different conditions. The system consists of four main sections as seen in Figure 2.14. Since only the tension and clamping assemblies are relevant for this work, only these two are described in detail.

For easier interpretation, each component is assigned a number on Figure 2.15. These markings are also given in parenthesis to match each component to the components shown in the figure. Clamping assemblies ('**1**' and '**3**') are located on both sides of the test stand. These assemblies have the same functionality except for the tension measurement, ability to shift the clamp on the y-axis in right clamping assembly ('**3**') and adjustability of the misalignment angle on the left clamping ('**1**') assembly. Functionality features of the clamping assembly can be seen in the figure above.

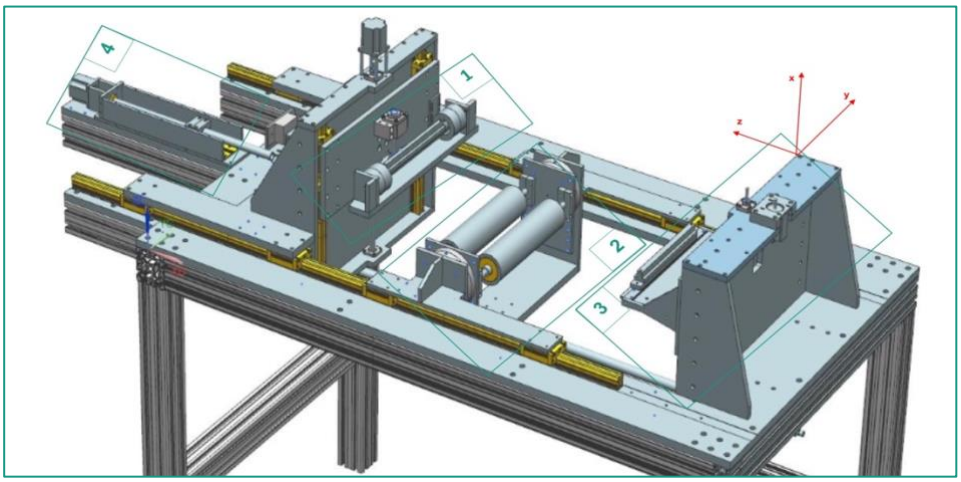

Figure 2.15: The Test Bench (Biernat, 2017)

The material is secured by a t-shaped top plate screwed onto another plate which is supported by the load cell bearing on both sides. These components are illustrated in Figure 2.16. The web tension is measured using two load cell bearings. These components are integrated onto the left clamping assembly ('**1**'). Using the voltage signal readings captured by the load cell, tension measurements can be performed in the range of $0 - 50\ N$ on each cell which sums up to maximum web tension of $100\ N$.

Direct measurement is preferred over other tension measurement techniques since it minimizes deviations resulting from external factors. Bending and friction forces are some of the external forces that cause deviations in the measurements.

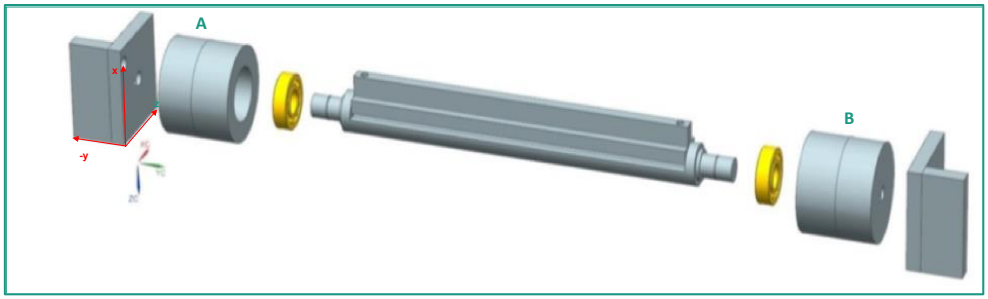

Figure 2.16: T-shaped clamping plate (top) with support plate (bottom) (Biernat, 2017)

Two separate measurements at positions '**A**' and '**B**' allow the consideration of potential errors in coaxial direction. Positioning in the x-direction is possible for both assemblies independently of each other. This is realized by a ball screw driven by a servo motor on each assembly. These servo motors are able to adjust the position of the assemblies precisely. Effects of misalignment can be observed by rotating the left clamp assembly with respect to the z-axis. The angle adjustment can be determined with factors of $0.5\,^{\circ}$ in the range of $-1\,^{\circ}$and $3\,^{\circ}$.

Right clamp assembly ('**3**') has fewer features compared to the left clamp assembly. As seen in Figure 2.17, as the clamp does not have a load cell, it is fixed on a plate without additional components. However, unlike the left clamp assembly, the right clamp fixture is shiftable on y-direction.

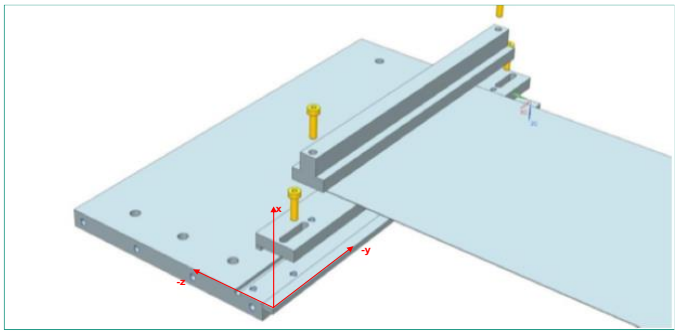

Figure 2.17: Right clamp assembly (Biernat, 2017)

Tension module ('**4**') tensions the web by pulling the web in the z-direction. This module is also illustrated in Figure 2.18. The tension module is linked to the left clamp assembly ('**1**') with a chain, a strainer and a hook respectively. The web tension can be set manually or using the GUI built on MATLAB. MATLAB controls the servo motor by comparing the set value to the load cell readings on the left clamp assembly.

One end of the tension spring is controlled by a servo motor. The servo motor communicates with MATLAB via a programmable logic controller. A ball-screw shaft assembly transforms the rotary motion of the servo motor into linear motion. The other end of the tension spring is attached to a long chain. Every mesh of the chain enables the system to be also adjusted manually with an extended range of tension. For finer manual adjustments in the range of $1-10\,N$, a turnbuckle strainer is used which allows smaller displacements. Both the chain adjustment and turnbuckle screw allows manual tension adjustment independent from the servo motor. The turnbuckle screw comes between the chain and a hook. The hook is attached to the frame plate of the left clamp assembly ('**1**'). As tension rises on the hook, the left clamp assembly is pulled towards the tension module moving left clamp in the z-direction guided by the rail system. The web fixed between the left and right clamp then starts stretching in the machine direction gaining longitudinal tension (Biernat, 2017).

Figure 2.18: Tension module

2.5 Lithium-ion Batteries

In order to compete with ICE vehicles, lithium-ion batteries are challenged to meet the demand of numerous customer needs. Lithium-ion battery technology enabled penetration of new generation electric vehicles into the transport sector (Masias, 2018). Lithium is easy to oxidize, light and small, factors that contribute to the attractiveness of Li for the making of lightweight, high voltage and fast charging batteries (Schlögl Robert, 2012).

The demand of the battery market is controlled by critical parameters such as energy density, power density, cycle life, cost ($€/kWh$), energy efficiency, recharge ability and self-discharge rate. Thanks to the Li high standard electrode potential and low equivalent mass (or volume), lithium-ion batteries feature high energy density. Despite the high cost, safety issues and material availability concerns, high efficiency, long lifetime and low self-discharge rates help lithium-ion battery to be very competitive compared to other commercial batteries (Mahmoudzadeh Andwari et al., 2017).

2.5.1 Components

The functional role of the lithium-ion cell components is the same as in other secondary batteries[1]. Each cell is made up of a cathode, an anode, current collectors, an electrolyte, a separator, and the respective casing. Selection of materials for these components is what makes the lithium-ion cells distinct.

Charging initiates the migration of lithium ions from the cathode (Metal oxide) to the anode (graphite). Lithium atoms support the layered crystal cathode structure and complete Li depletion of the cathode would change the structure and collapse the cathode. This is a consequence of mechanical instability induced by extreme volume fluctuations. Therefore, the ability to utilize the maximum amount of lithium without changing the mechanical properties is vital in choosing a suitable positive electrode material. For example, $\mathrm{LiCoO_2}$ can utilize lithium migration up to 55% without losing its mechanical stability (Burheim, 2017).

Current collectors provide the electrical conductivity and thus the current may flow from or to an external electrical circuit. The material selection for the collectors depends on physical and chemical characteristics. The most important physical parameters are mechanical strength, weight, and thickness (Glaize and Genies, 2013).

Aluminum is currently used as cathode current collector in lithium-ion batteries. Aluminum foil with high purity is desirable, especially concerning the weight and chemical stability of the material. Moreover, it is cost-effective. Yet, aluminum suffers from pitting corrosion after extensive cycling due to high voltages. In contrast, aluminum shows a better corrosion resistivity when it is used with a $LiFePO_4$

[1] Secondary battery: Type of battery that is capable of re-charging for a number of cycles.

electrolyte solution as this solution can operate at lower voltages in comparison to the $LiMn_2O_4$.(Iwakura et al., 1997)

Copper foils are generally utilized as an anode as it shows stable performance at a lower narrow voltage range. Copper, however, is not suitable for over-discharging conditions. Unlike the aluminum current collector, it is less corrosion resistant and over time dissolution is inevitable. In fact, the majority of lithium-ion batteries should not be over-discharged. Over-discharging results with high anode potential which triggers copper dissolution. Dissolved copper particles may plate on the active material surface blocking the transferrable lithium ions, and posing the risk of short-circuiting (Myung et al., 2011).

The electrolyte maintains the ionic transport between the anode and the cathode through the separator to allow the ionic flow that counterbalances the electron flow across the external circuit. The electrolyte is mainly based on various organic solvents were Li salts are dissolved. The lithium-ion transfer should be tested for the safety limits, under a wide range temperature and charging rates (Gulbinska, 2014).

$\mathrm{LiPF_6}$ (Lithium salt) is commonly used as salt in the electrolyte. It is highly reactive to water molecules and formation of HF is unavoidable in the presence of $\mathrm{H_2}O$. Up to a limited extent, this formation is desirable, as the battery performance benefits from a limited amount of HF formation. This formation yields increased cycle life and HF helps to build a protection layer of $\mathrm{Li_2}O$ on the graphite surface. This phenomenon is called formation of an ionically conductive Solid Electrolyte Interface (SEI). SEI causes capacity losses and therefore the excessive formation of SEI should be avoided (Ozawa and Matsuki, 2009).

A separator is the most vital passive component of lithium-ion cells. Lithium-ion cells suffer from safety problems, namely thermal runaway. Examples range from the Dell computer incidents in 2006 to Samsung phone battery incidents in 2016. Taking the example of the Samsung phone incidents, the company published a press review upon their investigation. Based on the publication (2017), a damaged separator was the probable cause of the thermal runaway. The welding burrs penetrated the separator and there was direct contact between the anode and the cathode. As a result of the internal short circuit, the cell temperature rose excessively eventually inducing thermal runaway. Since the separator protects the battery against short circuits, it must be carefully handled during manufacturing and assembly (Zhu et al., 2018).

2.5.2 Working Principles

The lithium-ion battery works on the basis of reversible intercalation of the lithium-ions. Reversibility decreases over time. Reversibility is reduced through side reactions and permanent deposition of lithium ions at the electrodes. These occurrences determine the service life of the battery. Charging begins when the battery is connected to an external power source. By imposing a potential difference, the anode is reduced and the cathode oxidized, resulting in an electron flow from the cathode to the anode. The charging reactions are illustrated in Figure 2.19 in the forward direction.

Cathode:	$LiMO_2 \leftrightharpoons Li_{1-x}MO_2 + xLi^+ + e^-$
Anode:	$C + xLi^+ + xe^- \leftrightharpoons Li_xC$
Overall Reaction:	$LiMO_2 + C \leftrightharpoons Li_xC + Li_{1-x}MO_2$

Figure 2.19. Chemical reactions of a lithium ion cell during charge

The accumulation of electrons at the anode is counterbalanced by the intercalation of the lithium ions. As the lithium ions are positively charged, they move through the electrolyte to the electrode where they intercalate forming Lithium Graphite. A simplified representation of the lithium-ion cell and its components are shown in Figure 2.20. Discharge is exactly the opposite of the charging mode. Instead of an external power source, the battery is connected to an external load, the carbon anode is oxidized and the metal oxide cathode is reduced (Linden and Reddy, 2002).

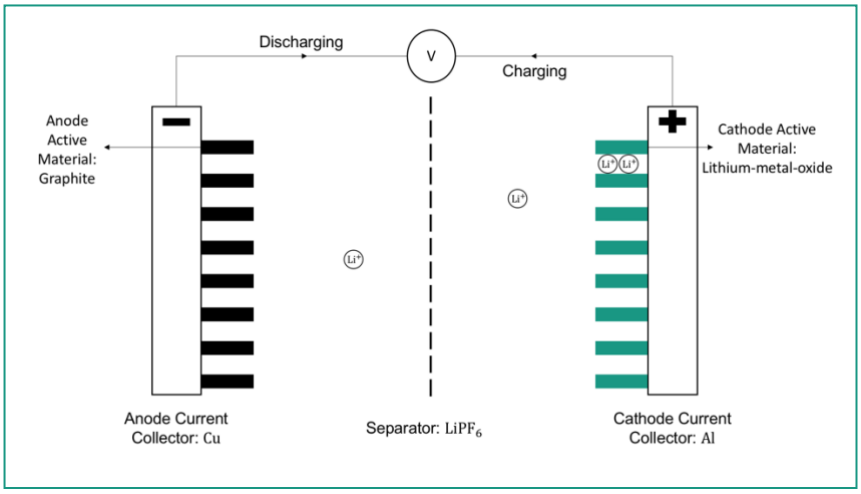

Figure 2.20. Simplified illustration of a lithium-ion cell

2.5.3 Cell Types

Lithium-ion cells are categorized into different forms. This type of classification is convenient as the packaging design has a significant impact on the battery metrics and performance parameters such as temperature management, self-discharge rate, cost, and lifetime. Besides, automation and retro-fitting of manufacturing equipment are taken into account in comparing different types (Maiser, 2014). Figure 2.21 illustrates three different forms of lithium-ion cells: cylindrical, prismatic and pouch.

Some sources in the literature also consider pouch cells as a sub-category of prismatic cells. However, this classification is regarded to be inaccurate as pouch cells feature flexible design geometry, unlike the prismatic cells (Schröder et al., 2017).

From the manufacturing standpoint, prismatic and cylindrical cells differ from pouch cells. Electrodes and separators are assembled by folding or stacking in the pouch cells and winding for the other two. Prismatic and cylindrical cells consist of electrode strips and separators while pouch cells are composed of single sheets of electrodes and either single sheets or z-folded strips of separators.

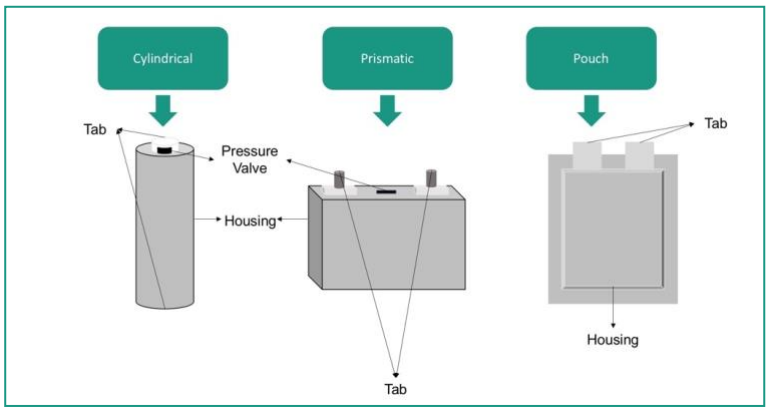

Figure 2.21. Classification of batteries according to their shapes (Schröder et al., 2016a).

2.6 Web Handling

The handling of continuous flat material strips, so-called 'web', is conveyed by roll systems that have shaft axes nominally parallel to each other. The term ‘web’ may refer to a variety of materials that is in continuous strips. From now on, the terms web and foil are used interchangeably. The challenge of making the processes faster in order to render the products more economical leads to higher rejection rates, inferior quality products, and inefficient production (Pfeiffer, 1987). To prevent potential malfunctions in web handling and also to eliminate the existing web quality problems, understanding web behavior under tension is of importance.

Web mechanics is analyzed to optimize the roll-to-roll manufacturing processes. Adjustments are accommodated either in the machine direction (longitudinal) or the cross-machine direction (lateral) to stabilize the oncoming fluctuations. Driven rolls control the machine direction parameters such as speed and tension and Web guides reposition the web in the lateral direction (Seshadri and Pagilla, 2012).

2.6.1 Web Stability

Forces acting on the web can be simplified by using an imaginary resistive tension member (IRTM) approach. Figure 2.22 presents the positioning of two different IRTMs. $RM1$ is the tension due to a resistive member with a perfectly aligned web and $RM2$ is the tension when the roll is non-parallel to the previous roll. The lateral force F_{lat} can be quantified as follows:

$$F_{lat} = RM2 * \sin(\theta) = -F_{st} = \tan(\theta) * T_2 \quad \text{Eq. 2.6.1}$$

where T_2 is the traction force, F_{st} is the stabilizing force and θ is the misalignment angle of the web. Traction forces T_1 and T_2 can be quantified as follows:

$$T_1 = RM_1, \quad \text{Eq. 2.6.2}$$

$$T_2 = RM_2 * \cos\theta. \quad \text{Eq. 2.6.3}$$

Eq. 2.6.3 shows the correlation between the tension and angle of misalignment (Hawkins, 2003). Bending stiffness is an important parameter particularly for the thin film materials considering their flexibility. This is mathematically described by flexural rigidity:

$$D = \frac{Et^3}{12(1-\nu)}. \qquad \text{Eq. 2.6.4}$$

where the terms *D*, *E*, *t*, and ν refer to the flexural rigidity, Young's Modulus, thickness and Poisson's Ratio respectively. As given in Eq. 2.6.4, the thickness has an impact on the order of the third power (Liu et al., 2018). Extremely thin webs have negligibly low stiffness. Thereupon, thin foil structures can be handled by pulling each tension member through a machine roll. The tension applied on the foil is due to the traction forces applied by the roll on the contact surface. These traction forces are presented in Figure 2.22 as T1 and T2 (Hawkins, 2003).

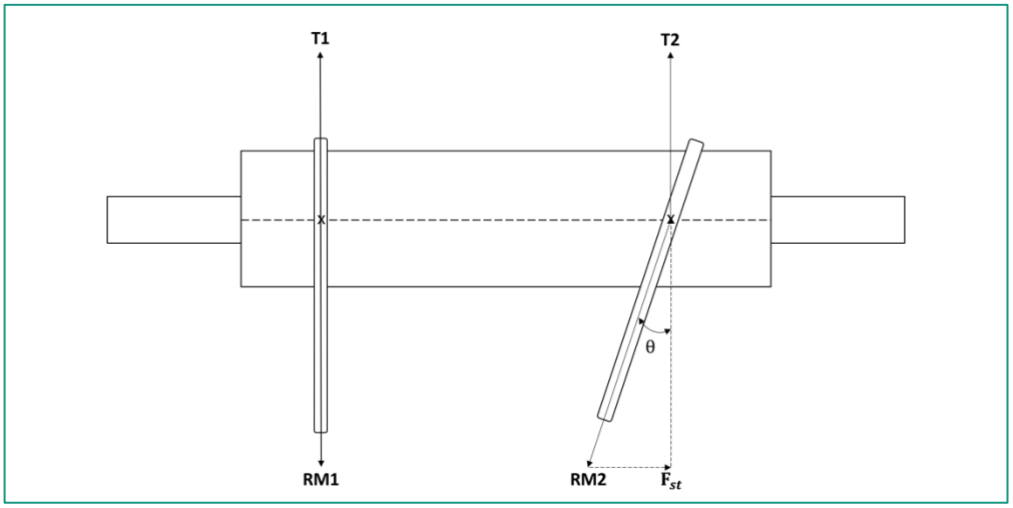

Figure 2.22. Visualization of Imaginary Resistive Tension Member Approach (Hawkins, 2003)

The addition of these traction forces over the relevant surface area that is in contact with the roll defines the total web tension. Inhomogeneous tension across the profile causes web disturbances. In case this behavior is persistent, the critical velocity reduces. The critical velocity is an upper threshold at which static instabilities occur beyond this velocity (Banichuk et al., 2013).

2.6.1.1 Roll Misalignment

The accuracy of the alignment between two rolls depends on the bending stiffness of the web material. Operation tension, width and flexibility of the roll are determining parameters of the tolerable misalignment angle (Hawkins, 2003).

Misalignment of a roll results with angle θ in Figure 2.22. As this angle increases, shear stresses arise. Critical misalignment angle limits the handling design and assembly regarding the orientation of the roll placement. Beyond this angle, the bending stiffness is not anymore sufficient to resist the compressive loads caused by shear stress. Consequently, buckling occurs due to excessive shear across the web. Once the misalignment angle is set, tension is the only factor to avoid buckling (Tang et al., 2017).

2.6.1.2 Air Entrainment

Traction is essential for web handling stability. The critical velocity is strongly correlated with the coefficient of friction and the web tension distribution. Rotation of the roll drives the air towards the interface between the web and roll. Beyond the critical velocity, the air entrainment is strong enough that a layer of air starts forming between surfaces causing traction losses (Arzate and Tanguy, 2004).

By ensuring adequate surface contact of the web with the roll, traction is sustained. In the absence of slippage, web materials tend to approach the roll perpendicular to the roll axis. This is also called web perpendicularity (Pfeiffer, 1987). Low tension and higher speeds lead to significant variations of tension. This is explained by an air film layer growing thicker between the web and the roll. Eventually, slippage occurs due to loss of contact between the working surface pairs. Under these circumstances, relative motion between the roll and web is present (Shin and Kwon, 2007).

2.6.1.3 Tension and Velocity Imbalances

Sliding web, an uneven roll surface or cambers on the web are possible causes of velocity fluctuations. These fluctuations also result from tension fluctuations across the web, as these parameters are strongly coupled together. The web tension fluctuations are even more critical considering that any accumulation overshoots below or above the upper/lower tension limit lead to folds or possibly even tears on the web (Koc et al., 2002).

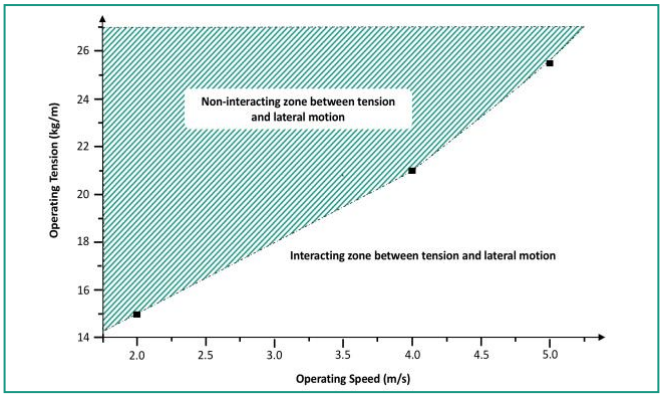

Figure 2.23: Lateral motion and interdependence between tension and lateral motion.

As shown in Figure 2.23, Shin and Kwon (2007) evaluated the relationship between speed and tension concerning lateral motion. This figure shows a combination of baggy web and high speeds with a tendency to a more radical lateral movement. Low tension causes the web to undulate. The increasing velocity makes it even more unstable since the frequency of the waves is dictated by the operating speed. A growing layer of air film discussed in 2.6.1.2 facilitates the loss of lateral control.

2.6.1.4 Inhomogeneous Tension Profile

The Effects of inhomogeneous tension profile at the downstream of the roll are investigated by Banichuk et al. (2013). The inhomogeneous tension was assumed to be linearly distributed to avoid complex models. The thin elastic plate model was adapted to investigate the stability of the static forms

numerically. Based on isotropic material, negligible gravity forces and bending rigidity assumptions, the study has revealed a tension inhomogeneity of 20% between the edges decreased the critical velocity by 10%.

The tension distribution on the contact surfaces should be uniformly distributed. Any disturbance leads to instabilities and visible faults which impair the quality of the web and go beyond the maximum operating limit. Uneven tension and shear forces cause folds on the web surface due to localized force differences. In other words, the web tends to move towards a lower energy state, leading to changes in web geometry.

2.6.1.5 Anisotropy

A web can be classified anisotropic if it has a different Young's modulus depending on the direction of loading. Comparing the findings of Shelton (1969) and Hashimoto (2007), anisotropic materials have entirely different web characteristics considering the effects of misalignment angle and tension. Even a slight orientation difference can alter Young's modulus. These changes fluctuate the correlation between the tension and the angle of misalignment largely. Thus, it is hardly possible to predict the wrinkling behavior of anisotropic materials. Defining the system boundaries for tension and misalignment can potentially be used for a range of Young's moduli (Hashimoto, 2007).

2.6.2 Lateral Movement of the Foil

Even though web motion is meant to be in a longitudinal direction, in practice, this is often not attainable. Web conveyance systems are often subjected to lateral disturbances. Lateral motion can be triggered by either the physical properties of the web or the web handling assembly. Identification of the potential problems and their impact on the motion, particularly in the lateral direction, is critical in order to prevent productivity losses of the production system and lowered web quality. Thus, understanding the lateral dynamics of the web is critical (Sievers et al., 1988).

Shelton (1969) applied the standard beam theory to quantify the response of the web towards web guiding systems and also to find the relation of process parameters to the lateral movement of the web. Kwon and Shin (2007), Sievers et al. (1988), and many others referred to Shelton's work as a basis of their studies on lateral dynamics of web handling.

2.6.2.1 Elementary Beam Theory

Shelton (1969) validated the use of elementary beam theory in a lateral motion as the web is transported between the two rolls. Comparing his experimental data with the theory, he concluded that the theory applies for lateral web dynamics. This approach is followed by this work such that the effects of misalignment for the single electrode sheet production can be evaluated. Following assumptions are used in order to apply this theory:

- All deflections are relatively small. The deflections are small enough to change the shape of the material such that the loads acting on the material do not affect the change considerably.

- Camber occurring on the edges of the web as well as any other uneven surfaces are assumed to be ignorable.
- The web has a homogenous and uniform structure and is free of local imperfections.
- Deflection due to shear is insignificant, the web that enters the web perpendicular to the roll axis remains perpendicular when it is exiting the roll. Consideration of span length is critical, as the shorter the span length gets, the greater the shear stresses are.

Shelton derived the critical correction angle θ_L using the steps discussed below. Considering the relatively small deflection angle θ following derivations can be obtained:

$$\lim_{\theta \to 0} \theta = 0, \quad \text{Eq. 2.6.5}$$

$$\sin\theta \approx \theta, \quad \text{Eq. 2.6.6}$$

$$dx = d\theta * \rho. \quad \text{Eq. 2.6.7}$$

ρ represents the radius of curvature. Using the postulate of geometric similarity

$$\frac{dl'}{dx} = \frac{\rho - y}{y} \quad \text{Eq. 2.6.8}$$

or,

$$dl' = \frac{\rho - y}{y} dx. \quad \text{Eq. 2.6.9}$$

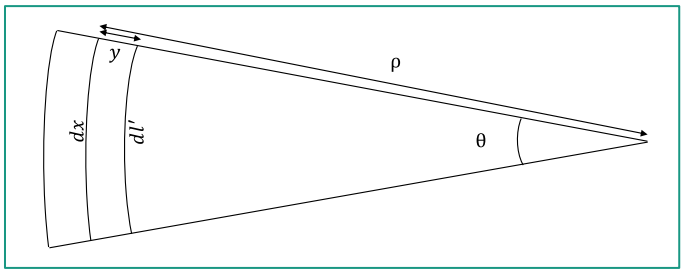

Figure 2.24: Euler-Bernoulli beam

$$\epsilon = \frac{dl' - dl}{dl} \quad \text{Eq. 2.6.10}$$

or,

$$\epsilon = -\frac{y}{\rho}. \quad \text{Eq. 2.6.11}$$

Strain ϵ is deformation rate of the sample of material with respect to its original length. The following equation defines the relation of stress and strain:

$$\sigma = \epsilon E \quad . \quad \text{Eq. 2.6.12}$$

Using equations Eq. 2.6.11 and Eq. 2.6.12 maximum strain ϵ_{max} and maximum stress σ_{max} can be obtained:

$$\epsilon_{max} = \frac{y_{max}}{\rho}, \quad \text{Eq. 2.6.13}$$

$$\sigma_{max} = E * (\frac{y_{max}}{\rho}), \quad \text{Eq. 2.6.14}$$

$$\epsilon = -\epsilon_{max} \frac{y}{y_{max}} \quad \text{Eq. 2.6.15}$$

and

$$\sigma = \sigma_{max} \frac{\epsilon}{\epsilon_{max}} = \sigma_{max} \frac{-y}{y_{max}}. \quad \text{Eq. 2.6.16}$$

Force and moment equations are as follows:

$$F = \int \sigma dA \quad \text{Eq. 2.6.17}$$

and

$$M = \int \sigma y dA. \quad \text{Eq. 2.6.18}$$

By placing σ from equation Eq. 2.6.16 into the force and moment equations Eq. 2.6.17 and Eq. 2.6.18:

$$F = \int \sigma_{max} \frac{-y}{y_{max}} dA = -\frac{\sigma_{max}}{y_{max}} \int y \, dA \quad \text{Eq. 2.6.19}$$

and

$$M = \int \sigma_{max} \frac{-y^2}{y_{max}} dA = -\frac{\sigma_{max}}{y_{max}} \int y^2 dA = -\frac{\sigma_{max}}{y_{max}} I \quad \text{Eq. 2.6.20}$$

or simply by replacing σ_{max} from Eq. 2.6.14,

$$M = -\frac{E}{\rho} I. \quad \text{Eq. 2.6.21}$$

Assuming the first derivative of deflection y' being close to zero, we can approximate the second derivative of deflection y'' as the radius of curvature $\frac{1}{\rho}$. Hence the moment can be rewritten as

$$M = -EIy''. \quad \text{Eq. 2.6.22}$$

The internal shear force ϑ can be calculated using

$$\vartheta = \frac{dM}{dx} = -EIy'''. \quad \text{Eq. 2.6.23}$$

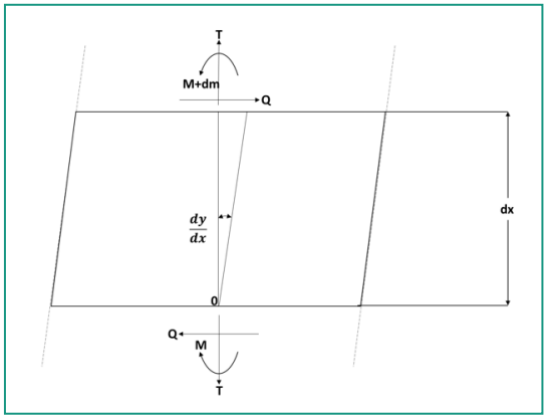

Figure 2.25: Free-body diagram of the web for static analysis (Shelton, 1969).

If the deflections present are trivial, a non-deflected configuration of the web can be used for internal force calculations based on this assumption. The reaction moment equation with reference to point 0 shown in Figure 2.25:

$$M + Qdx - T\frac{dy}{dx}dx - M - dM = 0 \qquad \text{Eq. 2.6.24}$$

Here, external shear forces are assumed to be insignificant. Therefore, dQ at location dx is disregarded from the free-body diagram shown in Figure 2.25. Rearranging Eq. 2.6.24 and Eq. 2.6.23 yields

$$Q = \frac{dM}{dx} + T\frac{dy}{dxdx}dx = -EIy''' + Ty'. \qquad \text{Eq. 2.6.25}$$

Since there's no external shear load, Q is constant and thus, $\frac{dQ}{dx}$ yields 0. Using this expression

$$\frac{dQ}{dx} = 0 = -EIy^{iv} + Ty'' = y^{iv} - K^2y''. \qquad \text{Eq. 2.6.26}$$

constant K replaces $\frac{T}{EI}$ based on the assumption that tension, Young's modulus and the area moment of inertia across the web are constant. Eq. 2.6.26 is a 4th order linear ordinary differential equation. Using the expression $y = e^{\lambda x}$, the general solution is

$$y = C_1\sinh(Kx) + C_2\cosh(Kx) + C_3x + C_4 \qquad \text{Eq. 2.6.27}$$

To determine four unknown constants, four boundary conditions are required. These conditions can be listed as follows, using Figure 2.25 as a reference:

- Point $x = 0$ is the starting point of the web. The lateral position $y(x)$ of the web at $x = 0$ can be assumed as zero.
- Assuming friction forces in the lateral direction being sufficient to counteract towards the lateral forces, the lateral speed $\frac{dy}{dx}$ at position $x = 0$ can be equated to zero.
- As the misalignment angle at $x = l$ is θ_L, due to web perpendicularity, $\frac{dy}{dx}(x = l)$ is equal to the misalignment angle at that position.

- At position $x = l$ the moment M is zero. The finite radius of curvature of the web implies the web is longer on one side and smaller on the other. With adequate traction in the longitudinal direction (no slip), the velocity differences between the edges would exert a moment on the roll until the moment cancels out with the movement of the web. This bias supports that the moment must be zero at downstream of the free span (Shelton, 1969).

Substituting the last boundary condition into Eq. 2.6.22 yields

$$M(x = l) = 0 = -EI\, y(x = l)'' = y_L'' \qquad \text{Eq. 2.6.28}$$

Using the first three boundary conditions, all constants can be defined in terms of C_1. Using Eq. 2.6.27 and Eq. 2.6.28, placing all constants in terms of C_1 and simplifying the equation results with:

$$C_1 = -\frac{\theta_L}{K}\frac{\cosh(KL)}{\cosh(KL)-1}, \qquad \text{Eq. 2.6.29}$$

$$C_2 = \frac{\theta_L}{K}\frac{\sinh(KL)}{\cosh(KL)-1}, \qquad \text{Eq. 2.6.30}$$

$$C_3 = \theta_L\frac{\cosh(KL)}{\cosh(KL)-1}, \qquad \text{Eq. 2.6.31}$$

and

$$C_4 = -\frac{\theta_L}{K}\frac{\sinh(KL)}{\cosh(KL)-1}. \qquad \text{Eq. 2.6.32}$$

Using Eq. 2.6.29 through Eq. 2.6.32 and plugging them into Eq. 2.6.27, the equation of motion yields

$$y = -\frac{\theta_L}{K}\frac{\cosh(KL)}{\cosh(KL)-1}\sinh(Kx) + \frac{\theta_L}{K}\frac{\sinh(KL)}{\cosh(KL)-1}\cosh(Kx) + \theta_L x\frac{\cosh(KL)}{\cosh(KL)-1} - \frac{\theta_L}{K}\frac{\sinh(KL)}{\cosh(KL)-1}. \qquad \text{Eq. 2.6.33}$$

Based on the assumption that the axis of the first roll corresponds to the y-axis, the critical condition is illustrated in Figure 2.26. Critical condition is where the inner edge of the web at $x = 0$ has no tension. In other words, the inner edge of the web is slack at the upstream of the first roll. As tension is assumed to be uniform across the width w, resultant tension can be described as T and is located in the center of mass of the triangular load distribution. Hence, tension T is positioned with a distance of $w/3$ from the outer edge of the web.

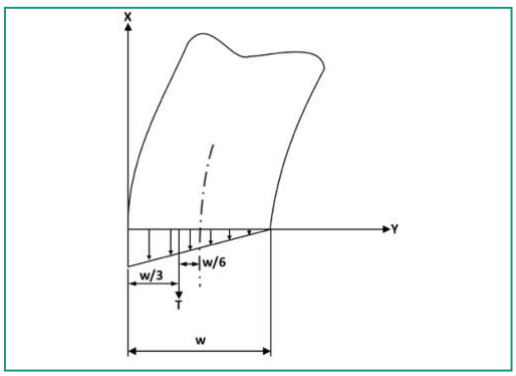

Figure 2.26: Defining the critical condition based on the tension distribution (Shelton, 1969).

Moment equation and Critical moment can be derived using Eq. 2.6.28, Eq. 2.6.33 and the position of resultant tension T:

$$M = \frac{\theta_L T}{K}\left(\frac{\cosh(\mathrm{KL})\sinh(\mathrm{Kx})}{\cosh(KL)-1} - \frac{\sinh(KL)\cosh(Kx)}{\cosh(KL)-1}\right), \quad \text{Eq. 2.6.34}$$

$$M_{0,crit} = -\frac{Tw}{6} = -\frac{\theta_L T}{K}\frac{\sinh(KL)}{\cosh(KL)-1} \quad \text{Eq. 2.6.35}$$

Rearranging Eq. 2.6.35, critical angle can be derived:

$$\theta_{L,crit} = \frac{Kw}{6}\frac{\cosh(KL)-1}{\sinh(KL)}. \quad \text{Eq. 2.6.36}$$

Under the defined assumptions, Shelton's static behavior approach can be used to determine relevant parameters of the critical moment and misalignment. The critical angle of misalignment $\theta_{L,crit}$ depends on Young's modulus E, the moment of inertia I, width w, and length L.

2.6.2.2 Validity of Beam Theory

Beam theory does not apply to the following factors unless the variation of these factors is considerably small:

- Velocity variation
- Change of span length
- Dancer motion.

The speed variation during the acceleration or deceleration of the driven rolls is accompanied by the tension variation since these factors are coupled. Change of span length is associated with two possibilities: the motion of a dancer to counteract against the tension variations or the turret rotation on winding and unwinding rolls (Kang and Lee, 2008).

The potential causes mentioned above are avoided while carrying out the experiments. Thus, the results can be used to compare to the theoretical results using the beam theory. The electrode handling assembly at wbk has velocity variations and also equipped with a dancer which changes the span length.

Any theoretical analysis also considering such factors would require advanced computer simulation methods. The scope of this work is rather to have an experimental approach to identify the problems faced during the electrode processing. Determination of these issues point to the boundaries of the system. This is essential to design an electrode processing assembly with improved cycle time.

2.6.3 Web Handling Problems

It is decisive to locate and understand the challenges of processing thin webs. Handling problems can arise due to the web itself as well as the handling system. This section focuses on these possible problems and a key objective is to improve the processes from unwinding the calendered electrode until the electrode residue is removed from the system.

2.6.3.1 Wrinkle Formation

Wrinkle formation is the most common problem in web handling applications since these defects impair the web quality, result in machine downtimes and material loss. Identifying potential causes of wrinkling and intervening against permanent wrinkles improves the performance of the web handling equipment (Lin and Mote, 1996). Typical wrinkle forming conditions are associated with errors such as roll misalignment, web-treatment problems and the imperfections on the roll geometry. These problems usually result in wrinkles recur in the same location. If the location of the wrinkles is unstable, then the problem is presumably span or time-dependent. These type of formations can be a result of factors such as the inaccurate tension control mechanism, uneven or cambered web surfaces (Hawkins, 2003).

A linear normal tension distribution in both ends of the web over all four edges would be the ideal case to obtain flawless operation. Wrinkles emerge as the non-linear portion of the load exceeds the critical value. The critical non-linear load should be estimated under consideration of the flexural stiffness. Wrinkle formation is induced due to the material's inability counteract against the compressive loads. The resistivity of counteraction against compressive forces can be quantified by the flexural stiffness of the web material (Lin and Mote, 1996).

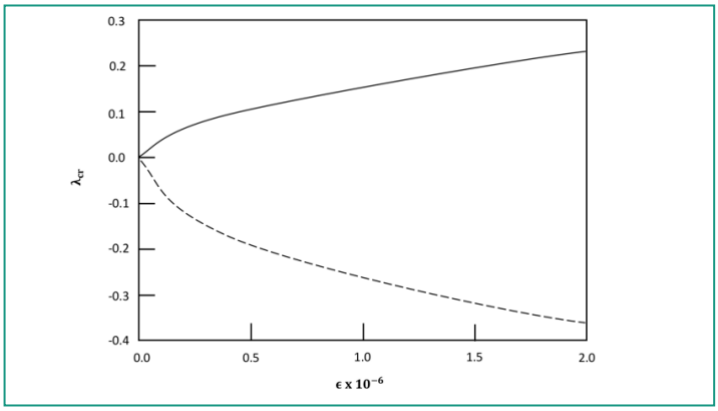

Figure 2.27: The relation of stiffness ratio ϵ and critical value λ_{cr} (Lin and Mote, 1996).

According to Lin and Mote (1996), the effects of the stiffness ratio ϵ have a significant influence on the formation of wrinkles. The stiffness ratio is described by

$$\epsilon_{st} = \frac{Et^3}{12(1-\nu^2)Tl^2} \qquad \text{Eq. 2.6.37}$$

Wrinkle formation can be avoided between the continuous and dashed line depicted in Figure 2.27. By adjusting parameters in the stiffness ratio, the critical value range for wrinkle formation can be avoided. The upper and lower critical values are λ_{cr}^{P} and λ_{cr}^{N} correspondingly, where these values are determined by taking the largest negative and smallest positive eigenvalues of the dimensionless equilibrium equation of the web (Lin and Mote, 1996).

2.6.3.2 Delamination

Strong adhesion between the active material and current collector is essential to prevent rapid ageing of the cell. Delamination indicates loss of electrical contact between the active material and current collector. This problem induces internal resistance, triggering the ageing process. Delamination can occur either during the operation of the battery or during the electrode handling.

Graphite has a porous structure which allows the electrolyte to penetrate through these pores optimizing the transport of lithium ions. This structural change results in large volume variations which may cause delamination of the material. Maintaining a good adhesion when processing the electrode is therefore vital for the battery service life (Vetter et al., 2005). The sheets of active material coated foils are subjected to bending loads when these sheets are transferred to the cutting assembly. Extreme bending stresses can also cause the active material to detach from the foil. Given this consideration, bending stresses on the electrode web conveyor assembly should be prevented to the greatest extent (Kaiser et al., 2014).

2.6.3.3 Scratches

Relative motion between the roll and web can result in scratches on the web surface. As discussed in 2.6.1.2, a relative motion should be avoided for web processing applications. Relative motion forms a zone within the wrapped surface that has raised tension between web entering the roll until it leaves the roll. This zone is known as the creep zone due to elongation resulting from tension differences. If the creep zone grows beyond the plastic deformation limit of the material, the scratches appear on the surface of the web.

Despite the increased coefficient of friction, which allows improved traction, the rough surface of the rolls causes more scratching problems compared to rolls with smooth surfaces. Therefore, the surface material for the rolls should be selected carefully based on the toughness of the web. Tougher materials can be used on rubber surfaces, while more sensitive materials should be operated on roll materials with better surface quality like steel or aluminum (Hawkins, 2003).

Consequently, the scratches pose a potential risk to the electrode conveying assembly. Even if the scratches do not affect the battery chemistry as much, chipped off particles can puncture the separator, leading to serious safety hazards such as thermal runaway.

Chapter 3

Methodology

This chapter presents the methods used to design the experiments. Additionally, the design of each experiment is described.

3.1 Structure

To preserve the result-oriented approach, mainframe of the work is subdivided into four stages: a collection of knowledge on the state of the art of lithium-ion pouch cell production and web conveyance technologies, drafting of experiments on the foundation of the gathered knowledge, execution of the experiments and designing the improvement proposal. Getting familiar with the current technology on lithium-ion pouch cell production and also with web conveyance fundamentals is essential to improve the current process errors and bottlenecks. The experimental procedure is intended to focus on the expected outcome while accounting for the knowledge gathered. The experiments are carried out obeying the procedure and the hypothesis for each experiment are examined using the quantitative data. Subsequently, the design proposals are presented on the basis of a comprehensive analysis of the experimental data and state of the art technology on web conveyance systems.

The scientific method is applied to design the experiments. By choosing a control factor and changing the independent variables, data is collected and analyzed. The test-bench described in 2.4.4 is modified to carry out the experiments that deliver relevant parameters to the focus of this work. To make this modifications, parts required for the necessary modifications are designed with the aid of Siemens NX 11. Designed parts are ordered accordingly.

The test bench is modified by replacing web clamp with an aluminum idle roll. In addition, the right clamp was also replaced with an aluminum roll which can be driven with a servo motor. The torque transmission is provided by a belt and a pair of gears. These modifications were done to perform closed loop web experiments which are discussed in 4.1.2.

Consequently, improvements possibilities are considered in order to optimize the processing speed of the electrodes both for the anode and cathode materials. Furthermore, components featuring the proposed optimizations are designed using the Siemens NX 11 such that these adjustments can be adapted on the design proposals. The designs are discussed in 5.1. Besides, additional research and design improvements are advised for the future work in Chapter 6.

3.2 Preparation of Experiments

3.2.1 Roll Roundness

Before conducting the experiments, rolls are inspected for geometrical imperfections. This procedure aims to account for the tension disturbances caused by imperfections such as dents, eccentricity, and waviness of the roll surface. In this case, two rolls are inspected: the driven roll and idle roll. The imperfections are identified by measuring the surface of the roll using a digital gauge.

Before the roll surface inspection, rpm is measured. Measured rpm is then compared to the estimated time given by the technical data of the motor and calculating the output rpm using the gear ratio of the torque transmission. A reference point is established and marked on both of the rolls to indicate the completion of each rotation. The tip of the digital gauge is placed on the roll surface to spot the reference mark point after the motor is set to a predetermined speed of $200\,rpm$. A stopwatch is used to time every turn it takes the roll to complete 360-degree rotation.

Figure A. 3 shows a comparison of the estimated rpm of the driven roll to the measured rpm. The difference is potentially the result of additional losses due to the belt used to transmit the torque from the gearbox to the roll. Slip and heat dissipation are potential resources of these losses. The average accuracy of the measurements is around 96.05% thus estimated rpm would give results for the roundness considerations with an error of 3.95%. For better accuracy, the average of the measured data is used for the roundness test. The time for 360° turn is averaged as $1{,}986\,s$.

The measurement is performed at five different locations. The illustration in Figure 3.1 shows the distribution of measurement points used on the roll roundness test. A measurement in 2-second intervals would imply an average difference of $0.014\,s$. Thus, approximately 139 measurements with $2\,s$ intervals would be adequate to get 139 distinct surface points on the surface of the roll. This assumption is used to collect the data points measured by the sensor for each location identified in Figure 3.1. The same calculations are also used for the idle roll, in which 81 measurements are adequate to obtain 81 distinct points for each section of measurement.

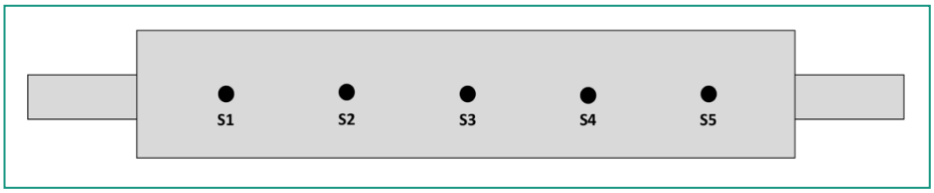

Figure 3.1: Representation of locations used on roll roundness test.

As shown in Table 3.1, the maximum difference between the diameter of the roll and local measurement is in the center (S3). The most significant difference is $12\,\mu m$ while the average difference is around $1.4\,\mu m$. Even if the most substantial differences are less than 0.005% of the roll radius, deviations in the driven roll surface are negligible at all sections. More detailed results of the idle roll deviations are shown in Figure A. 5.

Table 3.1: Evaluation of the driven roll roundness test.

Driven Roll	S1	S2	S3	S4	S5
Average Deviation (mm)	$1.15 \cdot 10^{-3}$	$1.092 \cdot 10^{-3}$	$1.40 \cdot 10^{-3}$	$2.199 \cdot 10^{-3}$	$0.773 * 10^{-3}$
Max Deviation (mm)	$4 \cdot 10^{-3}$	$3 \cdot 10^{-3}$	$13 \cdot 10^{-3}$	$7 \cdot 10^{-3}$	$5 * 10^{-3}$
Radius (mm)	450	450	450	450	450
% Average Deviation	$3.8 \cdot 10^{-4}$	$3.6 \cdot 10^{-4}$	$4.6 \cdot 10^{-4}$	$7.3 \cdot 10^{-4}$	$2.6 * 10^{-4}$
% Max Deviation	$13.3 \cdot 10^{-4}$	10^{-3}	$43.3 \cdot 10^{-4}$	$23.3 \cdot 10^{-4}$	$16.6 * 10^{-4}$

As given in Table 3.2, the most substantial average deviation on the idle roll is in S4 which is less than 0.0027% of the radius of the idle roll. On the other hand, the most significant deviation contributes to less than 0.005% of the roll, which is still minor.

Table 3.2: Evaluation of the idle roll roundness test.

Idle Roll	S1	S2	S3	S4	S5
Average Deviation (mm)	$2.89 \cdot 10^{-3}$	$0.76 \cdot 10^{-3}$	$6.3 \cdot 10^{-3}$	$8.07 \cdot 10^{-3}$	$0.05* 10^{-3}$
Max Deviation (mm)	$9 \cdot 10^{-3}$	$12 \cdot 10^{-3}$	$2 \cdot 10^{-3}$	$33 \cdot 10^{-3}$	$4* 10^{-3}$
Radius (mm)	300	300	300	300	300
% Average Deviation	$9.63 \cdot 10^{-4}$	$2.55 \cdot 10^{-4}$	$2.10 \cdot 10^{-4}$	$26.9 \cdot 10^{-4}$	$16.7* 10^{-4}$
% Max Deviation	$30 \cdot 10^{-4}$	$40 \cdot 10^{-4}$	$6.67 \cdot 10^{-4}$	$110 \cdot 10^{-4}$	$13.3* 10^{-4}$

Closed loop web experiments aim to evaluate the effects of operation-related parameters as well as material-related parameters. Operation-related parameters are web velocity, web tension and misalignment angle. Material related parameters can be listed as follows: the chemical composition of the material, thickness, width, and span. There are also additional parameters that cannot be quantitatively measured or controlled which also impact the experimental data. These parameters can be listed as follows: Adhesive band thickness, quality of adhesive attachment, quality of the cutting edges, and quantity, the severity of wrinkles on the web before the test bench is in operation.

The web is tested in a closed loop. This setup allows one to evaluate the same web at longer intervals under different conditions. For this purpose, existing test bench discussed in 2.4.4 is modified. Modifications include replacement of clamps with idle, driven roll and addition of a motor on the right clamp assembly. The idle roll and driven roll has a radius of $300\ mm$ and $450\ mm$, a width of $305\ mm$ and $290\ mm$ respectively. The motor powers the driven roll and can be controlled with a controlling unit equipped with a potentiometer as well as switches that enable to change the direction of rotation, instantaneous velocity and acceleration.

The web is operated under constant tension and velocity such that the elementary beam theory in section 2.6.2.1 is comparable with the experimental data. A closed loop web is operated continuously to evaluate the web under different operating parameters.

The transfer of the material on the test bench requires a sequence of steps. These steps aim to minimize the formation of permanent wrinkles until the material is transferred and taped into its closed loop form. First, a tape band longer than the desired width is cut and placed near the test bench. This is to ensure the adhesive tape is on hand as soon as both corners of the web are entirely parallel to each other. The web is then unwinded from the supply roll onto an intermediate roll which is made out of cardboard. The intermediate roll allows the material to be transferred to the test bench and also provides a support structure to tape the ends of the material onto each other. After the desired span is wrapped onto the intermediate roll, a rotary cutter is used to cut the web on a plate with a smooth surface. The rotary cutter is guided with a ruler in order to ensure smooth and even edges.

The intermediate roll can then be mounted on the frame between the clamping assemblies. This frame is typically built for fitting additional idle rolls which can then be used to check the impact of variable wrapping angles. This assembly is illustrated in Figure 2.15, which is marked as '**2**'. Two screw heads at each end of the frame enable the intermediate roll to rotate without any translational movement unless it is lifted upwards and removed from the frame. The web can now be unwinded to wrap around both of the rolls. Once the loop is completed one side of the web is placed onto the other end of the web which is supported by the intermediate roll. The web should overlap perfectly on both sides in order to ensure each side has the same loop length and tension. Otherwise, tension distribution will be uneven, this results with one edge taut and the other edge baggy web. Subsequently, the closed loop is then permanently secured with the help of an adhesive tape. The assessment of the results should account for the section which has the tape, as the thickness of the web changes due to the tape and overlapping webs on this region.

In order to evaluate the results visually, a camera is placed onto the setup. It is essential to maintain the position so that results can be evaluated from the same point of view. This configuration intends to evaluate the effects of the velocity, misalignment angle, tension, and span. The material web is observed both visually with the help of a camera and quantitatively measuring the tension readings using the load cells. The input velocity and acceleration of the driven roll are adjustable with the potentiometer of the motor controller unit. Such tools ared used to evaluate the impact of process parameters on the critical velocity. The critical velocity is the velocity where the wrinkle formation starts. Thus, wrinkle formation can be detected using camera. The velocity and tension is monitored by the motor controller and load cell respectively. Material and process-related parameters is discussed in the following sections.

3.2.1.1 Material Related Parameters

Experiments are conducted with current collector foils as well as the foils coated with the active material on them. The anode consists of a copper foil with a graphite coating. The cathode consists of aluminum foil with a $LiCoO_2$ metal oxide coating. Effects of different spans can be demonstrated for Aluminum. Aluminum, coated aluminum, copper and coated copper have the thickness of $19\ \mu m$, $116\ \mu m$, $10\ \mu m$, $143\ \mu m$ respectively.

Effects of web span are tested with aluminum foil material. The material is predicted to have a stronger lateral motion and less stable operation for shorter spans of material. This hypothesis is based on Shelton's (1969) interpretation of beam theory, and its relation to the shear stress accordingly. The experiment focuses on three different spans of aluminum with the same thickness, similar quality of adhesive taping, and a number of wrinkles. Along with the span, variation of tension and velocity are also evaluated interchangeably such that the impact of these parameters on different spans is also assessed.

Aluminum material is also compared to the cathode active material coated on both sides of the aluminum foil. Since the cathode is thicker than the pure aluminum foil, it is expected to have considerably higher flexural stiffness. It is therefore expected that the cathode will be more stable towards extremities such as increasing misalignment angle. The cathode is also expected to operate more stable also under lower tensions regardless of the operation velocity due to the higher flexural stiffness. However, as discussed in 2.4.2, the coating is not uniform across the entire web body. For this purpose, testing the cathode web under higher tension needs to be evaluated carefully. In this context, the material behavior under higher tensions may pose interesting results particularly for the assessment of the stable operation of the positive electrode.

The anode is made of high-purity copper coated with graphite active material. Pure copper foil and anode web are also tested for comparison similarly as the aluminum foil and the cathode web described above. As the copper foil is thinner, the impact of thickness change is expected to change more severely. Therefore, change in thickness is more radical and hence is expected to affect the stability more distinctly compared to aluminum and cathode.

3.2.1.2 Operational Parameters

Each of the material parameters mentioned above are evaluated under various operational parameters. Impact of different velocities are evaluated under constant tension and misalignment angle. To minimize the inertial effects, acceleration is minimized to the lowest possible value. Here the effects of velocity are expected to be associated with the misalignment angle and tension accordingly. Therefore, the hypothesis includes all three parameters. Three tension values are expected to be assessed with three different misalignment angles along with three different velocities.

The lateral displacement is expected to increase concerning the rising misalignment angle accordingly. The higher angles of misalignment angle are expected to cause more instabilities and eventually lead to severe wrinkles across the web surface. Therefore, the aim is to start with 0° angle and to increase the angle until different tension and velocities, specifically lead to permanent longitudinal wrinkles. It is additionally expected to reveal a relation between lateral motion and a similar relation of tension and velocity similar to Figure 2.23. The results which can be used to make an objective comparison with the theory and that can contribute to the design proposal are presented.

3.2.2 Stress-strain Tests

Young’s modulus is a critical component in predicting the behavior of the web under different operating conditions. Determination of ideal operating tension can only be done with a constant Young’s modulus. Accumulations may occur due to parameters such as thickness, the direction of the tension load, homogeneity of the coating. In order to ensure that Young’s modulus is constant, a stress-strain test should be performed for each electrode. Here, the material should be evaluated with different sections and load directions in order to obtain information considering Young's modulus.

Additionally, these tests are also used for determining the maximum admissible stress (σ_c) and yield stress (σ_y). Yield stress is defined as the maximum stress that the material can handle without undergoing the phase of plastic deformation. Maximum admissible stress is the point where the material start's necking[2]. Maximum tension applied on the material should not exceed the yield stress in order to avoid material quality losses.

Tensile test for limp web materials such as aluminum foil is predicted to be problematic considering foil materials mostly do not exhibit much elasticity. For extremely thin materials the web might break from the clamp ends instead of breaking in the middle of the specimen. This situation leads to false readings. The stress-strain graph is obtained by measuring the amount of strain under increasing tension. In order to measure the strain of the material during the test, the strain is expected to occur in the center of the specimen so that sensors can detect the change in strain depending on the stress.

3.2.3 Side stretching Experiments

As described in section 2.4.3, the current process pulls the web towards the die-cutting assembly through a clamp which gains traction across the web profile. Alternative gripping methods are considered for the clamping principle. Based on the folding behavior mentioned in 2.6.3.1, an improvement in the transportation of the web is proposed. It is expected that, counteracting the shear forces eliminate the folding and straighten the web in the lateral direction. Elimination of these folds would imply better stability enabling higher operation speeds. To validate the accuracy of this hypothesis, side clamp design is proposed and is evaluated in this experiment setup.

The type of instabilities can be listed under different categories. Baggy edges, cross-directional and longitudinal wrinkles are the most common instabilities. Addressing these problems would improve the behavior enabling a faster operation with better quality products.

Side clamp testing assembly is designed such that it can be adapted to the existing test stand discussed in section 2.4.4. All of the components are mounted on the baseplate for the rotating assembly as shown in Figure 2.15 ('**2**'). The primary objective of this test is to assess the stability improvement possibilities by gripping and stretching the web. Unless the web wrinkling is material related, the direction and type of wrinkles are dependent and recurring based on the process parameters.

Cross-directional tension is obtained by the parts shown in Figure 3.2. The rail ('**4**') moves the module in the lateral direction and thus allows the stretching. The rail plate meshes with a guide mechanism, and their coefficient of friction is in the range of 0.04 and 0.08. This connection constraint all degrees of freedom except that in the lateral direction. Tension spring ('**2**') is attached to the rail.

[2] Necking: A concentration of large local stresses in a particular region of the material which leads to narrowed material geometry on the weak portion of the loaded sample.

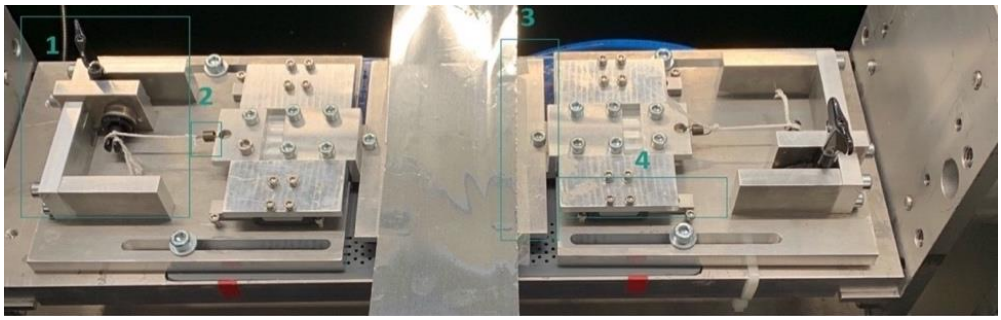

Figure 3.2: Side stretching test unit

The tension applied to the web is measured by measuring the strain on the spring. The tension can be calculated using the following formula:

$$T = k(x_2 - x_1) \qquad \text{Eq. 3.2.1}$$

where T,k, x_1, and x_2 stands for tension, spring coefficient, the initial position of the spring and final position of the spring respectively.

A bass guitar tuner ('**1**') is used to adjust the position of the spring. The spring is connected to the tuner via a fabric string which transmits the tension. The tension range foreseen is $2 - 16\ N$ for each spring summing up to $4 - 3\ N$ in total. By rotating the bass tuner handle in the clockwise direction, the string tension rises which pulls the web outwards.

Uniform force distribution is vital in order to reach a reasonable conclusion on this experiment. Three options are possible to fix the web to these mechanisms. These principles are discussed in 2.3. Mechanical gripping is risky regarding gripping reliability. The object may slide off of the fixture in case the friction is insufficient. Vacuum gripping, on the other hand, is complicated. Ensuring stable force distribution is difficult as the design should regard consideration of airflow. In addition, a large number of gripper plates with different design geometry would be necessary to perform reliable experiments. It is too costly and time-consuming to obtain the right design using vacuum grippers.

The last option is the adhesive gripper. The samples used on the experiments are not used on a functional battery cell, which means that contamination of the samples by the adhesives is not an issue. In addition, adhesives have a superior capability of uniform force distribution. Even though adhesives cannot be used on real-life applications on battery production, it delivers the purpose of the experiment. Thus, gripping of the web is emulated by an adhesive gripper. Adhesives are applied on the surface of the aluminum gripping plate ('**3**') which is pressed against the web. The aluminum clamping sheet is mounted onto the guide rail plate.

Chapter 4

Results and Discussion

This section discusses the experimental results and conclusions that can be withdrawn from the results of these experiments. Besides, theoretical principles are collated with the results of the experiments. Using the verified outcomes, design requirements are clarified for improvement proposals. Based on the requirements, feeder and gripper concepts are reviewed and compared. A preferred arrangement of feeder and gripper concepts are combined to introduce new designs.

4.1 Experiments

4.1.1 Tensile Test

The major intention of this test was to determine Young's modulus. Secondly, the isotropy of each material was tested. To adapt the theoretical background, the material should be isotropic.

Figure 4.1: Example of a valid negative electrode sample

Once the tests were initiated, since the material was so thin and also limp, most of the samples were broken on the edges which may have resulted with potential false readings.

Figure 4.1 shows the sample broken on the center between the clamping points. When the sample was broken on the clamped point, compressive loads were also present. This characteristic resulted in inaccurate stress-strain curves. The following sections exclude these samples.

4.1.1.1 Young's Modulus

Table 4.1, Table 4.2 and Table 4.3 shows the Young's modulus found for each sample; the average of the longitudinally, laterally loaded samples and the overall average of Young's modulus for aluminum, cathode, and anode, respectively. The difference between the average Young's modulus of laterally and longitudinally loaded samples are approx. $5\ GPa$. The overall Young's modulus is around $30.1\ GPa$. This value is used for the comparison of the theoretical approach to experimental results.

Table 4.1: Young's modulus evaluation of aluminum Foil with thickness of $19\ \mu m$

$E_{lat,avg}(GPa)$	27.794	$F_{y,\mathrm{LONG,AVG}}(\mathrm{GPa})$	72.473	$F_{\max,\mathrm{LONG,AVG}}(\mathrm{GPa})$	94.017
$E_{long,avg}(GPa)$	32.604	$F_{y,\mathrm{LAT},AVG}(\mathrm{GPa})$	79.464	$F_{\max,\mathrm{LAT},AVG}(\mathrm{GPa})$	103.424
$E_{avg}(GPa)$	30.199	$F_{y,AVG}(\mathrm{GPa})$	75.968	$F_{\max,AVG}(\mathrm{GPa})$	98.720

Comparing the laterally and longitudinally loaded results, positive electrode samples have a much closer average value. The difference is approximately $0.09\ GPa$ which is relatively much smaller compared to the difference between the aluminum samples. The overall average of the positive electrode is $6.25\ GPa$. There is a significant difference in Young's modulus between the aluminum foil and positive electrode material. This gives a better idea, how the double side active material coating had an impact on the material.

Table 4.2: Young's modulus evaluation of cathode web with thickness of 116 μm

$E_{long,avg}(GPa)$	6.326	$F_{y,LONG,AVG}(GPa)$	76.926	$F_{max,LONG,AVG}(GPa)$	93.998
$E_{lat,avg}(GPa)$	6.213	$F_{y,LAT,AVE}(GPa)$	73.341	$F_{max,LAT,AVG}(GPa)$	97.742
$E_{avg}(GPa)$	6.259	$F_{y,,AVE}(GPa)$	74.818	$F_{max,,AVG}(GPa)$	96.200

The direction of the load has a negligible difference on the anode samples. The average difference between the longitudinally loaded samples and laterally loaded samples is around $0.01\ GPa$. Young's modulus of the anode sample is defined with an overall average of $0.462\ GPa$ as stated in Table 4.3. Comparing these results to the cathode samples, cathodes have a Young's modulus about 13.6 times higher than the anode samples.

Table 4.3: Young's modulus evaluation of anode web with thickness of 145 μm

$E_{lat,avg}(GPa)$	0.472	$F_{y,LONG,AVG}(GPa)$	104.789	$F_{max,LONG,AVG}(GPa)$	124.951
$E_{long,avg}(GPa)$	0.455	$F_{y,LAT,AVG}(GPa)$	104.804	$F_{max,LAT,AVG}(GPa)$	123.507
$E_{avg}(GPa)$	0.462	$F_{y,AVG}(GPa)$	104.795	$F_{max,AVG}(GPa)$	124.357

4.1.1.2 Isotropy

To identify whether each material was isotropic or not, tensile loads were applied in σ_{xx} and σ_{yy} directions. In order to do this, a set of samples were cut lengthwise, while others were cut cross-wise from the same material. Thus, the tension load could be applied in both directions.

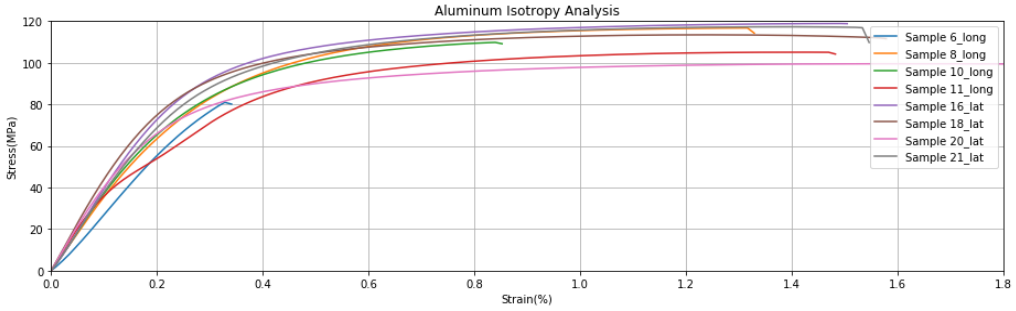

Figure 4.2: Isotropy analysis for aluminum foil with $3mm$ width, $14.5\ mm$ length and $19\ \mu m$ thickness.

Figure 4.2 displays the similarity between the longitudinal and lateral samples. The slope of the linear portion of the stress-strain curve is very similar, with the exception of sample 6, which was tested in the longitudinal direction. Sample 6 is assumed to be an outlier as the other three samples show almost identical slopes in the linear region in contrast to the other four lateral samples. However, considering the comparison of average young's moduli for the laterally and longitudinally loaded materials, there is a significant difference of $5\ GPa$. Figure 4.2 implies isotropic behavior, quantitative comparison shown in Table 4.1 suggests that Young's moduli do not agree with this statement. Hence, isotropy of the aluminum is questionable.

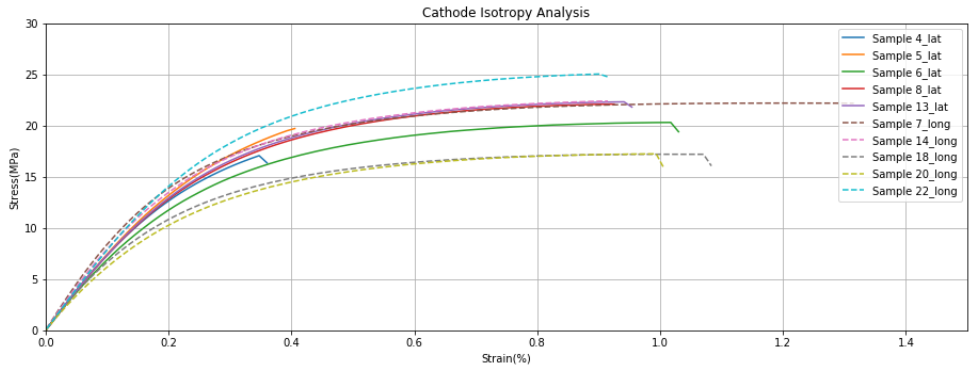

Figure 4.3: Isotropy analysis of the cathode $3\ mm$ width $14.5\ mm$ length and $116\ \mu m$ thickness

Figure 4.3 illustrates the isotropy analysis for the cathode. Five valid samples in each direction were tested. The material was calendered positive electrode with a $3\ mm$ width $14.5\ mm$ length and $116\ \mu m$ thickness. The tensile load direction has no influence on the slope within the elastic range. The quantitative comparison of laterally and longitudinally loaded samples in Table 4.2, also implies the presence of isotropic properties. Thus, the cathode is considered isotropic.

Figure 4.4 shows the results of the anode tensile test. Five samples for each direction are analyzed to compare the slope of the elastic region. The difference of $0.01\ GPa$ in average Young's modulus with a change of loading direction, also agrees that the anode samples are isotropic. The comparison of these images is shown in Figure A. 9.

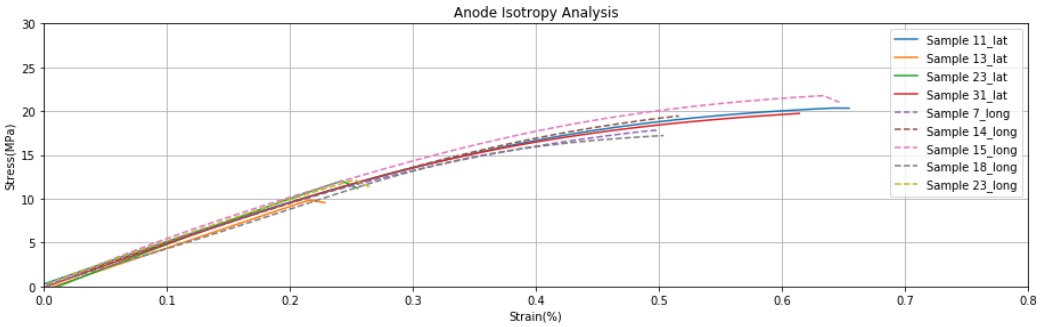

Figure 4.4: Isotropy analysis of the anode

4.1.1.3 Yield and Ultimate Tensile Forces

The average yield forces (F_y) and ultimate tensile forces (F_{max}) are shown in Table 4.1, Table 4.2, Table 4.3. The average yield force is around $76\ N$, $75\ N$ and $104\ N$ for pure aluminum, cathode and anode accordingly. The average maximum admissible force, also referred to as the ultimate tensile force is around $98\ N$, $96\ N$ and $124\ N$ for aluminum foil, cathode and anode web samples respectively.

The comparison of pure aluminum and cathode samples shows a similar maximum admissible force as well as yield force. The strength of the cathode was even slightly less in comparison to the pure aluminum foil. This was not predicted as the double-sided coating was expected to add additional strength to the material. However, it is clear that the double sided graphite coating doesn't affect the yield or admissible stresses.

The anode samples have a much higher yield and admissible forces in contrast to the cathode samples. This behavior is reasonable considering the anode being about $16\ \mu m$ thicker than the cathode which contributes to the flexural stiffness.

4.1.2 Closed Loop Experiment

4.1.2.1 Web Span

Before the experiments with web materials were carried out, sewing thread was placed on the test bench with a closed loop configuration to demonstrate the effects of the span on principle discussed in 2.6.1. The effects of threads were much simpler to evaluate with respect to the results of web with different spans. Visual examination and comparison of string and aluminum web span tests revealed that the behavior in different spans of material was barely comparable. The tension peaks due to adhesive band, made the evaluation complex and harder to compare for different spans. The lateral shifts of the sewing thread were less dramatic in contrast to the aluminum web. Thus, results of the thread experiments are rather illustrated in this section. This makes easier to compare the experimental data to the expected outcomes of the theory.

The thread tests were carried out with sewing threads with a span of $109\ cm$, $154\ cm$ and $195.5\ cm$ respectively. Under constant tension of $22\ N$, a motor speed of $3100\ rpm$ and same misalignment degree, the rate of lateral displacement changes as the thread gets shorter. The tests were carried out at high speeds to identify the differences between the lateral movement clearly.

Figure 4.5 shows a clear correlation between the web span and lateral displacement. The measurements shown in the figure is taken from the load cell located on the left side of the roll. Therefore, the decrease in tension is an indication of the string moving away from the cell. This was also clearly visible during the test as the motor was operating at high speed.

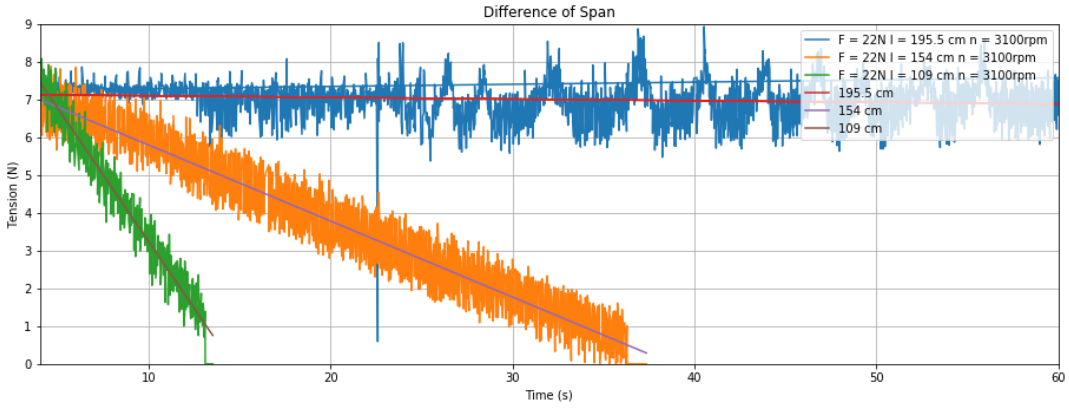

Figure 4.5: Illustration of effects of different span with IRTM Approach

The experimental data show that the shorter thread gets, the faster rate lateral displacement occurs. Applying Eq. 2.6.33 and the testing parameters as input, the test results and theory is compared. Misalignment angle could not be precisely determined as the angle could only be arranged with factors of $0.5°$. Therefore the comparison can be only assessed qualitatively.

As seen in Figure 4.6, both Shelton's principle and experimental results agree on a rising tendency of lateral displacement as well of the rate of lateral displacement as web span gets shorter.

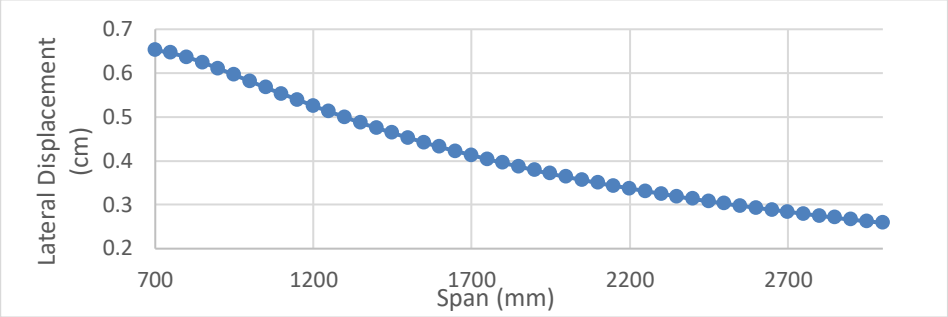

Figure 4.6: Correlation between lateral displacement and span according to Shelton's approach

4.1.2.2 Tension Variation

Aluminum foil with a thickness of $20\ \mu m$ was introduced into the closed loop setup. Aluminum web with a total loop span of $158\ cm$ was tested at a motor speed of 300 and $900\ rpm$. Web tension values were $22\ N$, $69\ N$ and $90\ N$. The misalignment angle was maintained constant. Tension measurements taken by the load cell was cyclic and repetitive with a small degree of variation. In other words, the lateral displacement is negligibly small.

Evaluation of tension fluctuations was the core of this experiment configuration. The effect of different tensions was monitored. To ease the comparison, the graphs obtained from each test were shifted such that all three tension values have the same starting point. The illustration of shifted curves can be seen in Figure 4.7 and Figure 4.8 with a motor speed of $900\ rpm$ and $300\ rpm$ respectively. Sinusoidal blue, orange and green curves refer to average web tension of $22\ N$, $69\ N$ and $90\ N$ correspondingly. All three tests were performed on the same web.

Aluminum web operated under lower tension resulted in less tension variation in contrast to larger web tensions. This relation seems to be more clear at operations $300\ rpm$. The operations at $900\ rpm$, however, seems to cause tension peaks, especially under high tension operation. This contradicts with the findings of Shin and Kwon (2007) discussed in 2.6.1.2. A possible explanation could be the web speed not being fast enough to form an air film and cause a slip in between the web and roll.

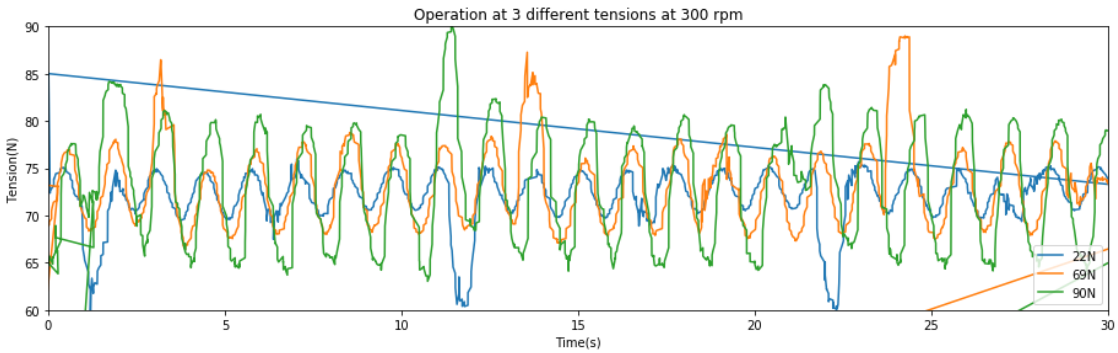

Figure 4.7: Operation of the aluminum web under 3 different tensions at $300\ rpm$

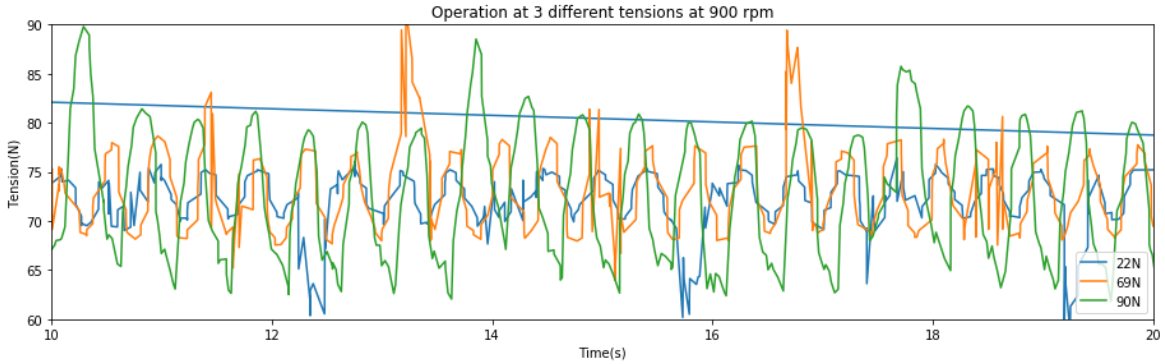

Figure 4.8: Operation of Aluminum Web under 3 different tensions at $900\ rpm$

Normally, undulating motion of the web due to low tension operation was expected to cause larger tension variations, while keeping the desired web tension higher would imply less undulating motion leading to tension fluctuations with lower intensity. The experiment, however, suggests otherwise. The implications of these experiments show that it is beneficial to operate the web rather with lower web tensions. The web under high tension causes large tension peaks and also a larger range of tension variations in this case.

4.1.2.3 Velocity

Figure 4.9 illustrates the comparison of the cathode material with different operating velocities under $68.5\ N$ tension. Higher speed intensifies rapid peaks in the tension profile. This peaks should be considered especially under high web tensions since the peaks can damage or even break the web. The peaks seem to be periodic. This could be an indication of a particular location of the web causing the peaks.

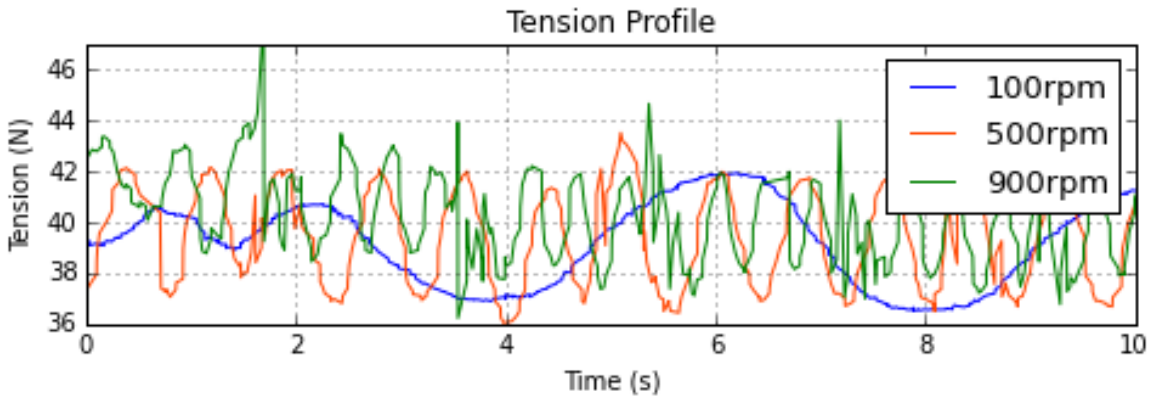

Figure 4.9: Cathode web tension profile at different speeds

In this case, these peaks occurred where the web was attached by a tape band. These peaks were induced due to non-uniform thickness across the web. The band caused the peaks since it adds significant thickness to this section of the web. The adhesive band is shown in Figure 4.10.

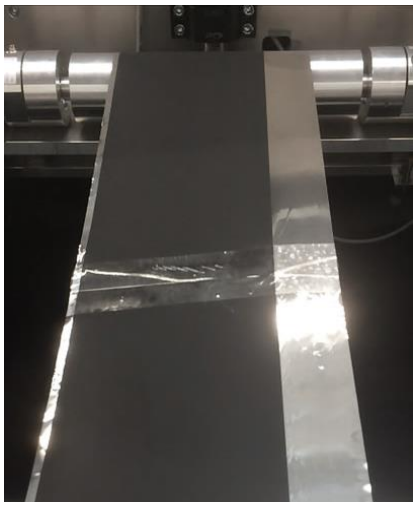

Figure 4.10: The adhesive band that caused tension peaks when in contact with the roll

This outcome also points to the problem of web disturbances. High-speed operation is only possible if the web has minimal thickness variation. Thus, even a small difference in thickness due to a wrinkle is a potential problem for high-speed operation. Wrinkles cause a tension peak as it comes in contact with one of the rolls. The tension peaks pose the risk of web quality degradation and may even cause the web to tear if the web is exposed to tensions beyond the admissible limit.

4.1.2.4 Coated vs. non-coated web

Tension profiles of aluminum and cathode webs were compared at $100\ rpm$ motor speed. The result is illustrated in Figure 4.11. Both samples were tested under the longitudinal tension of $68.5\ N$. The loop spans were $158\ cm$ and $156.5\ cm$ for aluminum and cathode web respectively. The images of both setups are shown in Figure A. 9.

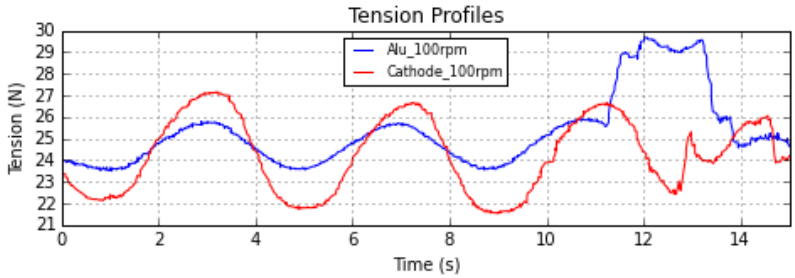

Figure 4.11: Tension profile comparison of Aluminum and Cathode webs at $100\ rpm$

There are two major differences in this comparison. Looking into the time intervals between $0 - 10\ seconds$, tension variation is roughly $2.1\ N$ and $4.9\ N$ for aluminum and cathode samples respectively. Secondly, between 11.5 and $13.5\ seconds$, there is a tension peak for one sample and tension trough for the other. The adhesive tape thickness difference caused these peak and troughs. Aluminum web has a larger peak in contrast to the cathode web. These differences are likely due to stiffness ratio. Thus, the stiffness ratio should be compared using the Eq. 2.6.37.

Young's moduli for both materials are defined in Table 4.1 and Table 4.2. The poisons ratio is taken as 0.33 and 0.2 for aluminum and cathode respectively (Wiedemann et al., 2013). The cathode stiffness ratio was larger by a factor of 44.58. The calculations are shown in Figure A. 10. Using this result, we can comment on the findings. The stiffness ratio is directly proportional to the tension variation and inversely proportional to tension peaks. In other words, the coating material causes a large increase of stiffness ratio, which results in a larger rise in tension variations and fewer tension peaks.

4.1.2.5 Misalignment Angle

Figure 4.12 illustrates a comparison of misalignment angle operating the aluminum foil at a motor speed of $100\ rpm$ and under a total tension of $68\ N$. The measurement here was performed only by the left load cell. The shift in tension is a result of the web moving further away from the load cell. Even at low speeds, a lateral displacement is visible at intervals of $5\ seconds$. The misalignment angle should be kept to a minimum, since even a slight misalignment results with imprecisely cut electrode sheets.

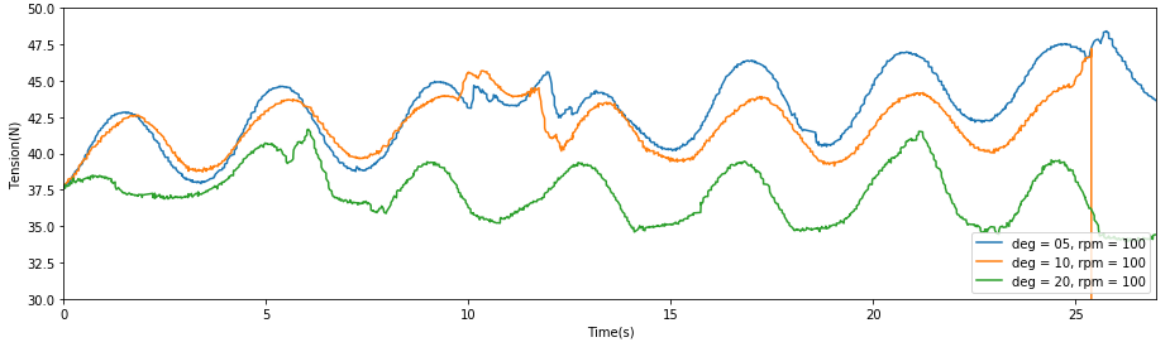

Figure 4.12: Single side load cell measurements at 0.5°, 1° and 2°.

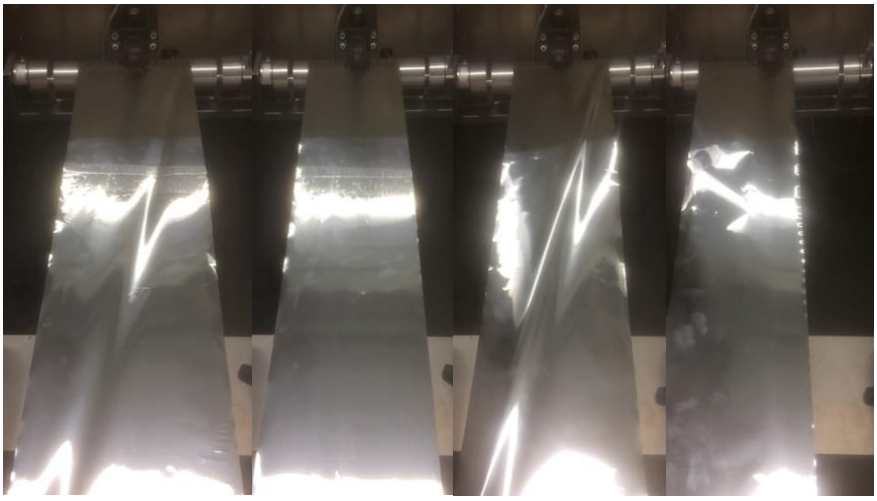

Figure 4.13: Before and after images of the aluminum foil with degrees of $1°$ and $2°$ respectively

Figure 4.13 shows the comparison of running the aluminum foil under $74.5\ N$ tension with $700\ rpm$ motor speed at $1°$ and $2°$ respectively. Comparing the first image with the second, it appears that $1°$ was tolerable for the web to recover the temporary fold seen on the first image without causing permanent wrinkles. At misalignment angle of $2°$, as shown in the fourth image, the web has wavy marks on the right edge. These marks can be considered as an indication of plastic deformation.

4.1.2.6 Influence of a Baggy Edge

An aluminum web with a taut center and a single-sided, baggy edge were accidentally developed as a result of inadequate adhesive tape application. The bagginess came from one edge of the web being shorter than the other, causing uneven web tension distribution across the web width. However, it was reasonable practice to visually inspect the web as it was operated on the closed loop setup. This inspection was instrumental in describing the behavior of the partially baggy webs. The web was conducted with $22\,N$ tension at a motor speed of $100\,rpm$ and the video was recorded at a rate of $120\,fps$. Reviewing the video at the rate of $24\,fps$ enhanced the ability to capture details regarding the motion of the sample.

Aluminum foils reflect light like a mirror which is helpful to differentiate even slight undulations as the foil reflects the light at different angles. Using this principle, the undulating motion of the baggy side was visible as the light reflection was radically changing. When the adhesive joint came in contact with the roll, the undulating motion stopped. The web appeared to be smooth, except for a slight change in the center, which was visible through a minor trough at this location. Figure 4.14 illustrates the instant the web surface with adhesive tape was in contact with the roller (left) and after this surface leaves the roller (right).

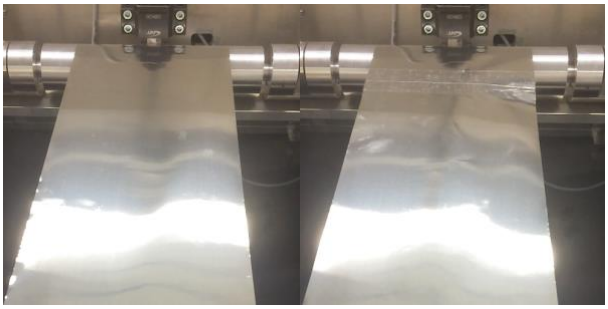

Figure 4.14: Behavior of the partially baggy web

Bagginess allows an additional degree of freedom in the x-direction since it is not stiff enough to exert a reaction force on the tension gradients caused by thickness variation at the point the adhesive surface contacts the roll. The additional degree of freedom enables propagation of this tension difference through the baggy portion of the web causing undulating motion. If this undulating motion exceeds the maximum strain the web can handle, local plastic deformations occur on the surface of the web resulting in permanent marks on the web.

The roll was able to balance the web when in contact with the adhesive joint. This response was a result of the roll pulling all of the IRTMs including the ones on the baggy side. However, as the aluminum web did not have much room for neither plastic nor plastic elongation, the tension built up on the taut portion of the web. Thus, despite the web looking equally taut, there was actually a considerable difference between the taut and baggy portions of the web. This statement can be further justified with the slightly trough region located in between the center and the baggy edge. This region is a clear indication of a transition zone with a considerable tension gradient. These kind of gradients pose a risk of plastic

deformation on the taut surface, permanent wrinkles or even tear-off. As long as each IRTM has the same span between the rolls, baggy surfaces can be prevented.

4.1.2.7 Evaluation of Wrinkle Formation

Aluminum foil with a thickness of $0.019\,\mu m$ was evaluated during wrinkle formation. The foil was operated at a negligible misalignment angle, a tension of approximately $50\,N$, and a motor rotation speed of $100\,rpm$. The loop span was in the range of $150-170\,cm$ which would be sufficient for the assumption of negligible external shear loads. The evaluation was completed comparing the tension measurements to the video of the experiment reviewed in slow motion.

Observing Figure 4.15 a) between $4-29\,s$ intervals, unveiled that there is a distinct shift of tension profiles. Therefore, the experiment video was examined looking into this time interval. In this interval, longitudinal folds developed into permanent wrinkles. Figure 4.15 b) shows the permanent wrinkle formed. The tension of the right load cell rises between $10-15\,seconds$ since the wrinkle formation is closer to this side. On the other hand, tension on the left load cell drops as the wrinkle formation is permanent, and it shortened the right side of the web, taking the load off the left side.

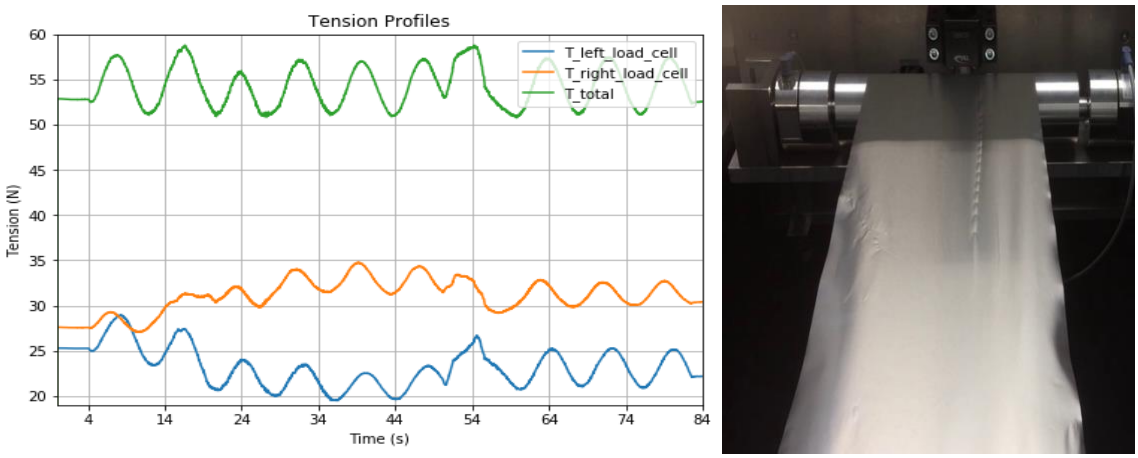

Figure 4.15: a) Tension profile during formation of permanent wrinkles b) Image of the permanent wrinkles.

4.1.2.8 Air Entrainment and Roll Surface Imperfections

At higher speeds, the air film between the roller and web grows thicker. This results in trapped air bubbles. These bubbles cause a local pressure rises at several locations. These pressure rises may cause plastic deformation causing dents on the web surface. On the other hand, similar dents can also result from roll surface imperfections. Using the conclusions from chapter 3.2.1, the dents shown in Figure 4.16, are due to air entrainment induced during operation at the rotor speed of $1100\,rpm$. These dents, however, were not present on the cathode web at the same operation speed. A likely explanation could be that aluminum surfaces on the cathode barely come into contact with the roll. On the other hand, active material layers on both sides have more resistance against the localized pressures.

Figure 4.16: Indentations on the Aluminum surface after high-speed operation

4.1.3 Side Stretching

Web tension is closely dependent on the severity of longitudinal folds. Externally applied shear forces remove the longitudinal wrinkles when applied with the right intensity. This conclusion is derived from the evaluation based on the graph illustrated in Figure 4.17. This graph shows the longitudinal tension applied on the sample, and lateral tension applied to remove the fold formed by the adhesives applied on a square metal plate with a $10\ mm$ length and $5\ mm$ width attached to the side stretching assembly.

Using the outcomes of section 4.1.2.1, longitudinal folds could be generated easily using webs with relatively shorter span. As generating the longitudinal were only possible under different conditions, results of the side-stretching experiments on different web materials are not comparable. The anode was tested under shorter web spans. When long anode sample was tested with the same setup, folds didn't sustain to reach the side stretching assembly. The cathode and aluminum samples were tested with similar spans which were relatively longer than the anode sample. Aluminum had much lower bending stiffness in contrast to the cathode material. It is thus harder to generate folds on the cathode web. Cathode samples required relatively higher web tensions to generate a similar longitudinal fold.

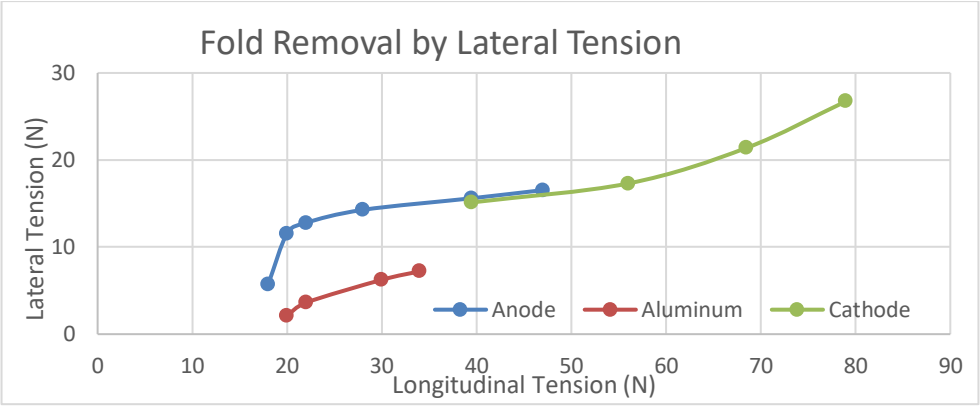

Figure 4.17: Lateral loads to remove longitudinal wrinkles under different web tensions

Side stretching assembly enables a great degree of controllability of the folds. The setup is simple and reliable. Operating the web under high tension makes the folds harder to remove. Higher stresses are required to overcome the fold forming localized shear loads. Different electrode materials require a different amount of tension to spread out the folds. However, adjustable spreading allows the flexibility to deal with a range of different type of folds on the electrode web. Hence, this type of setup can be considered as a web spreading solution for a large range of web spreading applications.

4.2 Feeder Concepts

4.2.1 Idle and Driven Rolls

Table 4.4: Benchmarking of idle and driven rolls.

Idle/Driven Rolls	Percentage (%)	In contact										Contactless	
		Rubber Covered Aluminum		Rubber Covered Steel		Aluminum		Steel		Carbon Fiber		Air Turn	
		Points	Value	Points	Value	Points	Value	Points	Value	Points	Value	Points	Value
Running Costs	15	3	45	3	45	3	45	3	45	4	60	5	75
Stability	15	2	30	2	30	3	45	3	45	4	60	5	75
Inertia	13	2	26	1	13	2	26	1	13	5	65	5	65
Contamination	13	3	39	3	39	2	26	2	26	4	52	5	65
Maturity	10	5	50	5	50	5	50	5	50	3	30	1	10
Complexity	8	4	32	4	32	5	40	5	40	3	24	1	8
Cost	8	5	40	4	32	5	40	4	32	2	16	2	16
Mounting	5	3	15	3	15	3	15	3	15	3	15	1	5
Adjustability	5	1	5	1	5	1	5	1	5	1	5	5	25
Running Costs	5	5	25	5	25	5	25	5	25	5	25	1	5
Maintenance	3	2	6	2	6	3	9	3	9	3	9	5	15
Total	100	313		292		326		305		361		364	

A benchmarking approach is applied in this section and the following sections. Each roll type is compared within the same table for several measures, considering the significance of each measure. The relevance of each measure is interpreted as a percentage. Each type is evaluated based on the performance of the solution for that parameter. The lowest score is one, which implies poor performance; the highest score is five, which indicates excellent performance. This score is then multiplied with the percentage defining a value for the corresponding parameter. In the end, all values are added to get a sum. These values give an overview score for each technology making them comparable.

Table 4.4, shows the comparison of each technology. Each parameter given in this table is briefly introduced before the technology comparison is presented. Speeding up the system without trading off for quality is the main focus of this work. Inertia has a significant influence on the stability and also on the critical speed. The roll mass affects web stability due to inertial forces particularly on production lines with repetitive start-stop motions. Electrode contamination should be avoided especially for electrode transport applications. Contamination affects both the performance and safety of the lithium-ion battery.

Lithium-ion batteries are manufactured in mass production facilities. Technologically mature solutions are desirable, as they offer ruggedness and lower equipment investments. Solutions with complex working principle have extended downtime in case of an unexpected failure. For instance, simple mechanical components can be replaced by in-house facilities, while more complex parts would require the input of the manufacturer. Equipment costs influence the unit cost of the product. Mounting also has a relevant impact on the machine downtime. Adjustability is explained later in this chapter.

Additional costs necessary to maintain the operation of the component are considered under the running costs parameter. Maintenance assesses the expected maintenance frequency of the component.

The Air Turn does not have any rotational parts allowing the web to be transported at very high speeds. Carbon fibre rolls cannot exhibit as promising performance, yet the lightweight structure enables a smoother acceleration which still eases the ability to accelerate faster in contrast to the steel and aluminum rolls.

Web stability is partly associated with roll inertia. Air Turn roll allows movement of the web free of inertia. Moreover, the airflow in Air Turn rolls has a natural spreading effect. This is a result of air flowing towards the edge of the web pushing the wrinkles away. Carbon fibre rolls also offer a better stability performance in comparison to the steel and aluminum as these rolls have less inertial forces thanks to its lightweight structure. The metal rolls, however, have a larger mass. For this reason, these rolls also have a larger moment of inertia which leads to poor stability.

In contrast to the metal rolls, rubber covered rolls are less likely to contaminate the electrode web. In contrast, the Air Turn provides a cleaner environment, as long as the supply air is not contaminated. Carbon fiber is more resistant towards, wear and chip-offs in contrast to the rubber, aluminum and steel rolls. This makes the carbon fiber rolls also a considerable option for contamination-sensitive practices.

Usage of aluminum and steel rolls are quite common. These rolls are more accessible, and there are a variety of manufacturers offering these rolls. In contrast, carbon fibre rolls are new to the market and are not yet widely used. Therefore, there are not many companies that offer these type of rolls. Air Turn rolls, on the other hand, are also very new to the market and are supplied by a single company. Thus, the availability of these rolls on a commercial scale is yet questionable.

Material roll replacement can be improved by adding a safety chuck instead of fixing the roll through a bearing to the housing. This allows the shaft to be removed without tools. The time saved by this feature improves the performance substantially. The Air Turn roll has additional tubing, and the roll is not built compatible with the safety chuck. Replacing the material roll requires much more effort compared to in contact rolls. However, a new housing design featuring easy roll changeovers is proposed in section 5.1.1.

Web height adjustability is an extra feature that the Air Turn offers. Adjusting the airflow, the distance between the Air Turn and web can be adjusted. As a result, the Air Turn is more flexible for different web thicknesses. Adjusting the supplied airflow webs with different heights can be handled which saves time and adds practicality.

The rolls with rubber sleeve covering should be replaced periodically as it wears out over time. In comparison, aluminum, steel, and carbon fibre rolls without covering require almost no maintenance as these materials are durable and the wear is not as much as it occurs with the rubber-web contacts. In other words, steel and aluminum rolls have almost no running costs. The Air Turn has continuous running costs as air compression is required to operate these rolls. However, accounting for the rotation-free operation, Air Turn rolls can be operated maintenance free for more extended periods in contrast to the other types.

As a result, the Air Turn and carbon fibre rolls have a better overall performance concerning the others. Despite being a costly solution, both of these rolls offer a better value of speed, stability, inertia as well as contamination. Comparing the scores of these two, as the difference is not distinctly decisive, both the Air Turn and the carbon fibre rolls are favorable for idle as well as driven roll applications.

4.2.2 Web Guides

Table 4.5 illustrates the benchmarking of web guide types. The web stability is the most relevant parameter here as web guides are meant to move the web laterally, and lateral movement is a significant cause of web instabilities. Besides, as discussed in earlier sections, a larger moment of inertia influences the stability of the web causing disturbances.

Position accuracy, on the other hand, is also decisive. An imprecisely cut electrode can lead to performance issues or even safety hazards. Additional components required to provide the guiding function is also considered since these parts add an extra dimension to space allocation, mounting, cost and complexity. The contribution to these parameters is separately considered under the additional components parameter in this table. Space allocation is also essential for manufacturing facilities regarding productivity, logistics and efficient layout planning.

Table 4.5: Benchmarking of web guides

Web Guides	Percentage (%)	In contact						Contactless	
		Steering		Partial Displacement		Complete Displacement		Radial Air Bearing	
		Points	Value	Points	Value	Points	Value	Points	Value
Stability	21	1	21	2	42	3	63	5	105
Position Acurracy	20	3	60	3	60	4	80	5	100
Cost	18	4	72	4	72	4	72	2	36
Aditional Components	11	3	33	3	33	3	33	3	33
Space Allocation	10	5	50	2	20	3	30	4	40
Mountability	8	3	24	3	24	1	8	5	40
Running Costs	7	5	35	5	35	5	35	1	7
Complexity	5	4	20	4	20	4	20	1	5
Total	100	315		306		341		366	

Concave radial air bearing shifts the web laterally forming a pressure difference. Contactless lateral motion contributes to better stability since there is no physical contact between the roll and the web during lateral motion. A complete displacement is also a plausible option for good stability. All of the rolls are connected to the same rail which can be powered by rack and pinion and a stepper motor. There is no relative movement between the rolls. Thus the stability of the web can be maintained.

The complete displacement assembly enables also pinpoint positioning thanks to the stepper motor allowing positioning by an angle of rotation. In contrast, air bearings offer even better precision. As reported in section 2.2.2, a $30\ g$ shear force can be controlled with a resolution of $1/100th$ of a gram which enables a sensitive control over the lateral position.

From the cost perspective, the steering guide offers the most economical solution. This guide only adjusts the misalignment angle rather than changing the positioning of the whole set of rolls. Both partial and complete displacement guides require more torque to move more components. Thus, a bigger motor is necessary for making these systems costlier than the steering guide. The radial air bearing is expected to be the most expensive since it is still not produced on a mass production scale. However, it is foreseen that this technology will be cost-competitive, as the industry will acknowledge this product to improve sensitive web materials.

The use of the radial air bearing would require compressed air while the other guidance systems would require stepper motor. Therefore, one is not necessarily more desirable than another regarding additional components. Additional components have a considerable impact, concerning space allocation and running costs. Steering guide occupies smallest least space as a motor, and a small guidance mechanism is sufficient to adjust the misalignment angle. In contrast, partial and Complete displacement guides move a set of rolls. In this case, larger linear guidance systems are required to handle the components. Air bearings can only be operated with compressed air, which would be supplied with an air compressor. In case the existing facility does not have the infrastructure to provide this air, a considerable amount of space is required to supply the bearing.

Moreover, air compression is an energy-intensive step. In contrast to the operating costs of the other three systems, which have a virtually free operation, the air bearing is unfavorable in terms of operating expenses. The air bearing also has an intricate design with a microporous structure. Therefore, the other methods are more favorable regarding the complexity, as these provide rugged electro-mechanical solutions.

Linear guiding is used on the steering guide and also displacement guide solutions. The entire system should be attached to the linear guiding which makes the mounting complicated. Air bearing, on the other hand, requires mounting of small components and tubing, which takes considerably less effort in comparison.

Despite the disadvantages like cost, maturity and additional components, radial air bearing provides a plausible solution with fine stability and precise positioning. These two parameters are vital particularly for electrode processing applications. Superior performance for these parameters differentiates the air bearing from the alternative guiding systems.

4.2.3 Web Spreader

Web spreaders are designed to pull the web outwards in the lateral direction. This is achieved by applying shear loads. Shear that can be applied by either physical contact or by vacuum. The web can be damaged, when the shear is applied through physical contacts. This is considered under the damage risk parameter. The term adjustability on Table 4.6 quantifies the adjustability of the spreading aggressiveness. Adjustability gives extra flexibility to handle a variety of wrinkles without damaging the web by spreading it excessively. Effectiveness parameter stands for the effectiveness of the spreading action.

The term aggressiveness, however, defines the capability of the spreader to spread out the extreme wrinkles.

Table 4.6: Comparison of web spreaders.

Spreaders	Percentage (%)	In contact										Contactless			
		Grooved		Bowed		Concave		Flat Expander		Angled Contact Nip		Vacuum Side Stretch		Angled Vacuum Nip	
		Points	Value	Points	Value	Points	Value	Points	Value	Points	Value	Points	Value	Points	Value
Damage Risk	25	2	50	2	50	2	50	3	75	1	25	5	125	5	125
Adjustability	15	1	15	1	15	1	15	4	60	5	75	5	75	5	75
Effectiveness	15	2	30	3	45	3	45	4	60	5	75	5	75	4	60
Cost	10	5	50	5	50	5	50	3	3	4	40	1	10	2	20
Agressiveness	8	3	24	3	24	3	24	4	32	5	40	3	24	3	24
Maturity	8	4	32	5	40	5	40	3	24	3	24	1	8	2	16
Complexity	6	5	30	5	30	5	30	2	12	3	18	3	18	3	18
Mounting	5	5	25	5	25	5	25	5	25	1	5	3	15	1	5
Running Costs	4	5	20	5	20	5	20	5	20	5	20	2	8	2	8
Maintenance	4	3	12	3	12	3	12	3	12	3	12	4	16	4	16
Total	100	288		311		311		323		334		374		367	

As already mentioned, contact spreaders have a higher risk of damaging the webs. Combination of contact rolls and high aggressiveness can scratch limp materials easily. Therefore, angled contact nip rolls should not be used unless extreme wrinkling is a frequent occurrence for the particular application. On the other hand, contactless spreading solutions can be used for aggressive wrinkles. These spreaders don't pose a risk of damaging the web as there is no physical contact.

The aggressiveness both for the vacuum side stretching and angled vacuum nip roll is adjustable during the operation. With an additional servo motor and a controller, these can be used with an encoder to correct the web autonomously as soon as the wrinkles are detected. In comparison, the flat expander spreader is an alternative in contact solution with a reasonable degree of aggressiveness and adjustability. However, these spreaders can only be adjusted manually. This type of adjustment is risky as asymmetrical modifications could lead to further wrinkle generations.

Grooved roll, bowed roll and concave rolls lack the flexibility of spreading a wide range of wrinkle types. Thus, the effectivity of these rolls is questionable. The flat expander and angled nip contact roll allow more flexibility. They can effectively spread out a greater variety of wrinkles. The vacuum side stretch and angled vacuum nip roll utilize airflow. Therefore, the distribution of shear loads is more uniform which provides effective spreading. Additionally, the force applied is adjustable which makes these two applications superior.

Angled vacuum nip roll and vacuum side stretching are new technologies. These solutions are not yet industrially acknowledges ones, since these products are not yet produced in masses. Hence both of these technologies have a cost disadvantage. Bowed roll is the most commonly used solution in the industry, and since the design is simple, it can be produced easily. From an economic standpoint, bowed roll is, therefore, a mature technology that offers a low-cost solution.

Bowed, concave and grooved rolls are implemented in one piece and are easy to assemble. In contrast, the nip rolls as well as the vacuum side stretch assemblies come in pairs and should be attached to both sides of the web. Considering this, mounting requires more effort for these applications.

Both of the vacuum-driven rolls have running costs due to the need for vacuum air. The contact spreading solutions do not have any running costs. However, as they directly contact the web, the roll surface results with wear over time. Thus, these rolls require more maintenance or replacement.

Contactless solutions offer a better performance despite higher running and investment costs. A uniform airflow enables good spreading behavior without posing the risk of damaging the material. Adjustable spreading gives greater freedom to handle a wide range of web disturbances.

4.2.4 Driving Mechanism

Table 4.7: Comparison of driving mechanisms

Driving Mechanism	Percentage (%)	In contact		Contactless	
		Stepper Motor		Radial Air Bearing	
		Points	Value	Points	Value
Cost	16	4	64	3	48
Stability	14	3	42	5	70
Speed	12	4	48	4	48
Controlability	11	5	55	3	33
Space Allocation	9	2	18	5	45
Lifetime	9	2	18	4	36
Maturity	8	5	40	1	8
Complexity	7	4	28	1	7
Mounting	6	2	12	5	30
Running Costs	4	4	16	3	12
Maintenance	4	1	4	4	16
Total	100	345		353	

Electrode web can be driven via a stepper motor or a concave radial air bearing. Other types of motors cannot comply with the precise electrode positioning in the longitudinal direction, so they are not considered for this comparison. Conventional web processing applications utilize the stepper motors to convey the web. These motors are characterized by precise positioning via the angle of rotation. Concave radial air bearing provides an alternative drive system. This technology enables precise positioning both in the lateral and longitudinal directions through airflow and air direction control.

Stepper motors are used in various industries in a wide range of products from automotive to robotics applications. The technology is well-developed, and these products are offered by a broad range of companies. In this sense, the stepper motors are cost effective. Besides, these motors are electrically driven; the electrical components barely require maintenance. The mechanical components are used to transmit the torque. These components, however, require maintenance or even replacements over time.

Additional components such as coupling or belt are required for torque transmission. This also leads to a distinct disadvantage regarding space allocation since gearing and couplings take additional space.

The radial air bearing is a competitive way to replace the motor-driven web conveying assemblies. Contactless operation enables the stable transport of the web with the least web disturbance possible. Airflow naturally exerts an external shear force in the lateral direction. This creates a natural spreading effect enabling stable operation. This technology is not yet used on a commercial scale since the concept of using air bearings to obtain rotational motion is relatively new.

For this reason, the components are expected to be less economical in contrast to the stepper motor. Contactless operation enables smooth acceleration. High speeds can be easily reached and adjusted by adjusting the distance and angle between the Air Turn roll and the radial air bearing.

The radial bearing is quite space efficient. It only requires minor space allocation for tubing and the speed, direction adjustment plate.

Mounting of the components does not require much effort. However, compressed air is costly since it is an energy intensive process to supply the air. It includes neither any parts to transmit the torque nor any rotational bodies, and maintenance is not necessary until the microporous structure is disturbed.

Since the stepper motor involves mechanically moving parts, the lifetime of the motor is limited. Air bearing theoretically does not have a lifetime limitation as far as the air provided does not have solid particles big enough to block the porous structure. Air quality is critical for the lifetime of air bearings.

Despite the cost disadvantage, concave radial air bearing improves stability, enhances process speed and has an easier mount, minimal maintenance, and a more compact design. However, as a result of benchmarking, since there is a slight difference between the two, one design features the stepper motor and the other features radial concave air bearing.

4.3 Gripper Concepts

The gripper concept is employed to move the end of the electrode web past the die-cutting tool while retaining it taut and stable. There is also an alternative approach to transport the electrode web fulfilling the same function of a gripper. This is presented in section 5.1.1. Die-cutting tool removes the utilized portion of the electrode with precision. The residual material is then removed which is also to be fulfilled by the gripper assembly.

Benchmarking approach implemented in the previous sections is also used here. Each gripper type is compared within the table for various measures with regard to the importance of each measure. The importance of each measure is interpreted in percentages. The performance of the grippers can be assessed from the following aspects: material damage, contamination, gripping reliability, speed, material and form flexibility.

Li-ion electrodes are limp and sensitive, particularly to local compressive stresses. Due to negligibly low flexural stiffness, the material web is easily punctured. Non-contact grippers including vacuum, magnetic

and electrostatic grippers deliver superior performance over contact grippers by eliminating frictional contacts that can cause material damages. Friction-induced grippers such as gripper jaws or surface hooking grippers such as needle grippers can scratch, dent or tear the material. Despite such drawback, these grippers can exert a substantial amount of gripping force on the object. Therefore, heavier objects are often better handled with these grippers.

Lithium-ion cells require a clean and dry environment to avoid the presence of burrs, other particles that pose the risk of puncturing the separator. Besides, in the presence of water molecules, the cells are chemically unstable. This side reaction mechanism is described in section 2.5.1. Particles with high electrical conductivity may cause short circuits within the cell. Furthermore, sharp particles may puncture the separator which may also cause short circuits due to internal current leaking through this puncture. All of these cases cause a decline in battery performance and are a potential cause of safety hazards.

Table 4.8: Comparison of grippers

Gripper Concepts	Percentage (%)	Force Closure								Form Closure		Material Closure	
		Friction Induced		Vacuum induced		Magnetic		Electrostatic		Surface Hooking		Adhesive	
		Points	Value	Points	Value	Points	Value	Points	Value	Points	Value	Points	Value
Non-damage Gripping	24	1	24	5	120	4	96	4	96	1	24	1	24
Contamination	21	3	63	4	84	5	105	5	105	3	63	1	21
Speed	17	4	68	5	85	4	68	4	68	4	68	1	17
Gripping Reliability	14	3	42	3	42	1	14	1	14	5	70	5	70
Gripping Force	12	4	48	3	36	3	36	3	36	5	60	5	60
Material Flexibility	8	4	32	3	24	2	16	2	16	4	32	4	32
Form Flexibility	4	1	4	4	16	3	12	3	12	2	8	1	4
Total	100	281		407		347		347		325		228	

Magnetic and electrostatic grippers have neither contact nor any molecules physically pushed in a specific direction. These attributes minimize the risk of contamination. Comparatively, vacuum grippers, still have a low chance of contamination due to airflow. However, if the provided airflow is prefiltered, the risk of contamination is negligible. On the other hand, contact grippers such as mechanical clamps and needle grippers are often made of metals. As the mechanical contacts wear out over time, there is a significant risk of contamination due to metal burr formation. In contrast, adhesive grippers, are not applicable for contamination-sensitive environments, as the gripping is achieved through the application of a chemical layer. Besides, removal of these chemicals may lead to free-standing particles on the surface of the electrode in the best case, de-lamination or tearing the electrode in the worst case. Thus, usage of the adhesives for the lithium-ion electrode processing is not possible. Hydro adhesive grippers are also ruled out from the comparison as the water molecules should not come in contact with the lithium-ions.

All grippers with the exception of the adhesive gripper, are characterized by fast actuation and gripping. Adhesive grippers require time to complete chemical bonding. To ensure a secure grip, all of the bonds should settle before lifting the object. These bonds allow the gripper and the object act in one piece and

become rigid. Therefore, adhesive gripping results in reliable gripping. In comparison, surface gripping is also reliable since it holds the object by penetrating through the material. This penetration makes the object difficult to slip away from the gripper. Vacuum grippers depend on an adequate airflow to ensure reliable gripping. It is intricate and time-consuming to identify the appropriate design to obtain such airflow. On the other hand, friction-induced grippers have the risk of the material slipping off. Thus gripper surface should have certain roughness to ensure a steady grip. The electrostatic grippers are limited to light materials as the electrostatic forces can handle the object reliable up to a limited weight.

Friction-induced grippers can be used on any material as far as the friction coefficient of contact surfaces is sufficient. Surface hooking grippers are also suitable for any material that can be penetrated. To ensure reliable and tight gripping, the porosity of the material is critical for vacuum grippers, restricting the material flexibility. On the other hand, a common cathode has a double-sided $LiCoO_2$ coating. Some electrodes such as $LiFePO_4$ cathodes that have ferromagnetic properties. However, not all of the cathode and anode electrode materials contain species that bring such properties. Thus, the magnetic gripper has a major disadvantage as it serves functionality for a limited kind of materials.

The suction cups and pneumatic tubing used in vacuum grippers are flexible. An extensive range of different geometries can be held with the same vacuum gripper, making these grippers versatile in contrast to the other alternatives. In contrast, friction-induced and surface hooking grippers have a limited ability to handle materials of different forms as the location of the applied gripping forces affects the gripping reliability.

Consequently, vacuum grippers have non-intrusive gripping capabilities. Such characteristic makes these grippers suitable for sensitive material applications. Moreover, contamination-free airflow and fast actuation enable safe, fast gripping and ejection of the object. Despite the complex airflow design requirements, the vacuum grippers feature an optimal solution for electrode web gripping.

Chapter 5

Solutions and Conclusions

This chapter describes the design proposals, the selection of the favorable design and reference to the design parameters obtained through the comparison of the theoretical background to the experimental results.

5.1 Design

The new designs incorporate unique systems capable of enhanced process speed and improved stability achieving a better product quality. Identified weaknesses discussed in 2.4.3.1 are eliminated to the greatest extent. Two different electrode handling assembly designs are proposed. Design proposals consist of modifications to the existing system which involves replacement and also complete elimination of some elements in the existing system. Since the selection of the die-cutting assembly is out of scope for this work, design modifications are adjusted to the specifications of this assembly. For intellectual property reasons, a CAD drawing of the cutting assembly could not be provided. Thus, the assembly used in the design proposals roughly designed based on the manual measurements of the existing system.

The gripper that pulls the end of the electrode web has a linear motion. This is a significant drawback regarding cycle time. As discussed in 2.4.3.1, the linear motion contributes to about 67.6% of the cycle time for each electrode sheet. Every time the electrode needs to be prepared for the die-cutting tool, the gripper has to accelerate, decelerate and stop, grab the electrode, accelerate in the opposite direction, decelerate and stop again.

Selection of system components for the design proposals is based on the comparison tables introduced in chapter 4.2, 4.3 and the outcomes of the experiments in chapter 4.1.

5.1.1 Contactless Electrode Transport Design

The web is transported in the current assembly using traction. Web stability is a prime issue with this type of handling. The uneven surface of the rolls or the non-parallelism between the rolls shift the web laterally and cause local tension variations, leading the web to an unstable state. Besides, roll surface imperfections cause dents on the web surface. Besides, inertial moments of the heavy rolls cause additional disturbances.

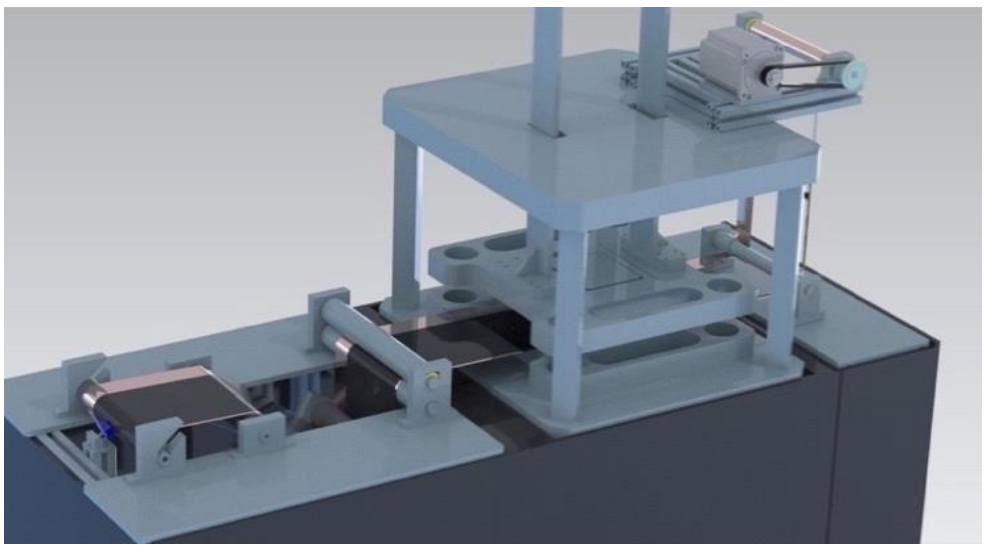

Figure 5.1: Contactless electrode transport

All components before the die-cutting unit can be seen more closely on

Figure 5.3. Each one is marked with a number which is given in parenthesis for the corresponding component in the text. Concave radial air bearing (‘**1**’) described in section 2.2.1.2 allows the web to shift in both lateral and longitudinal directions eliminating the need of an additional web guide. The air bearing is used in combination with the Air Turn rolls. The porous structure of the Air Turn rolls allows a uniform airflow. Uniform flow is vital for stability and precise control of the distance between the roll and web. The Air Turn roll replaces the aluminum driven roll, the idle rolls as well as the dancer roll.

The airflow that strikes the web surface follows the surface and leaves the web eventually inducing a self-spreading effect. This effect ensures that the web is kept taut in both the lateral and longitudinal directions as it passes through the rolls. During start-up and cut-off, the acceleration and deceleration cause fewer disturbances on the web as the inertial forces are eliminated.

Support plates of the driven roll (‘**2**’) can be easily mounted and dismounted allowing quick material roll changes. This feature replaces the function of the safety chuck. For material roll changes, the driven roll should be lifted and removed through the guide. Such a design provides safe operation and practical removal of the material roll without needing additional tools.

Pneumatic fittings fit in the shaft holes of the driven roll (‘**3**’), the idle roll (‘**4**’) and the dancer roll (‘**5**’). The distance of the web from the Air Turn rolls can be adjusted by controlling the same air supply control unit.

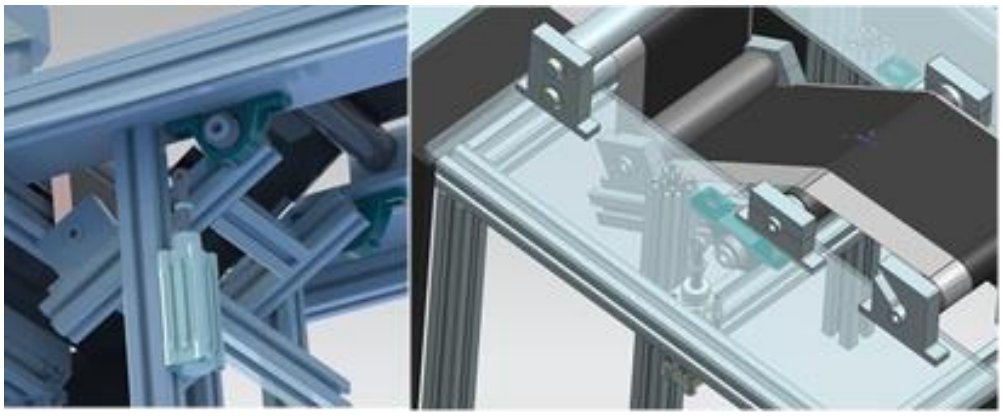

Figure 5.2: Dancer assembly equipped with Air Turn rolls

To minimize tension fluctuations, support plates of the dancer roll (‘**5**’) are attached to a pneumatic cylinder which is adjusted via an encoder using the output of the dancer position sensor. To keep the web taut while the die-cutting is cutting through the web, the aluminum nip roll pair (‘**6**’) is retained as the existing design.

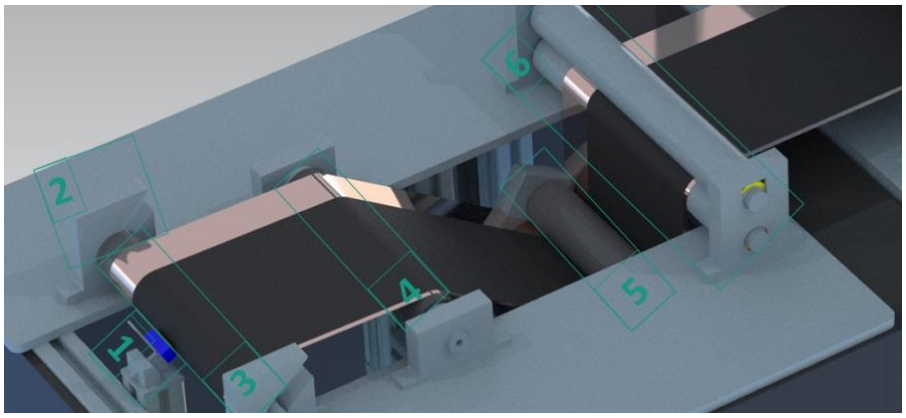

Figure 5.3: Electrode transport before the die-cutting assembly

Linear motion of the gripper is eliminated by replacing it with an aluminum idler roll. The discontinuity of the residual material is avoided by improving traction through the design shown in Figure 5.1.4. The surface is designed such that roll contacts the web only at the points where there is residual material.

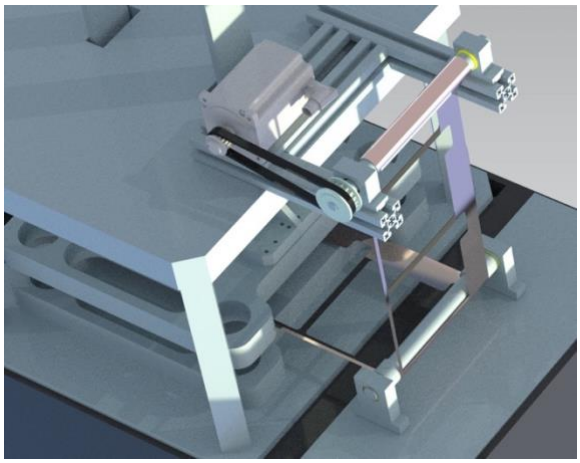

Figure 5.4: Electrode transport after the die-cutting assembly

This roll is followed by a driven aluminum roll which is used to wind up the residue. Driven roll is connected to a servo motor through a gear belt pair. Coordination of this servo motor and the radial concave air bearing is necessary; thus an additional encoder is required.

5.1.2 Second Design

Lateral position is crucial for lithium-ion cell production. The electrode sheets should be cut precisely to obtain standard quality and safety. Linear guide shown in Figure 5.5, is located on both ends of the unwinding assembly. The carriage supporting the frame allows lateral positioning. Linear guide rail allows low-friction movement and constrains the carriage movement to one axis. This motion is provided through a stepper motor. The torque is then transmitted through a coupling between the stepper motor and shaft-hub connection that drives a ball-screw pair. A ball nut is attached to the bottom of the carriage. When the stepper motor rotates the screw shaft, the ball nut starts moving. The moving direction is defined by the rotational direction of the stepper motor.

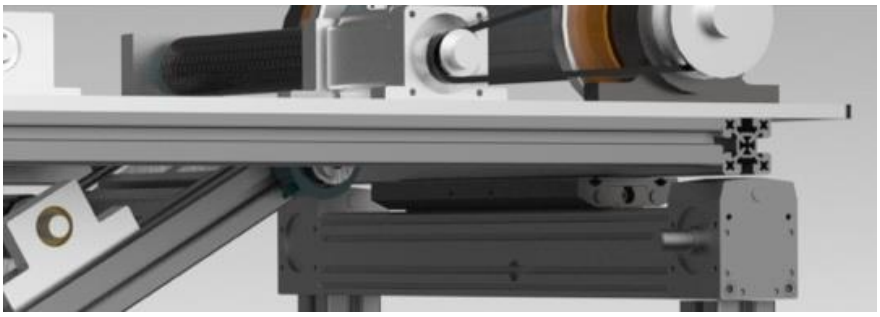

Figure 5.5: The guide rail allowing position adjustment in lateral direction

Unwinding mechanism is similar to the original design described in Chapter 2.4.3. The mechanism can be seen in Figure 5.6. The longitudinal traction bars (‘**1**’) lock up the material roll as it begins to rotate. The material roll can be removed easily by sliding it off in the lateral direction.

The safety chuck (‘**2**’) enables quick material roll changes. This component is shifted laterally with a push by hand whereby the upper portion of the square key geometry is clicked out. The roll is now no longer constrained in the x-direction(opposite of the direction of gravity). The unwinder roll (‘**3**’) can then be removed by simply lifting it. When the material roll is placed onto the unwinder roll, it can simply be placed back, and the chuck can be clicked back into its locked position. A stepper motor (‘**4**’) drives the roll. Torque is transmitted via gear-belt pair (‘**5**’).

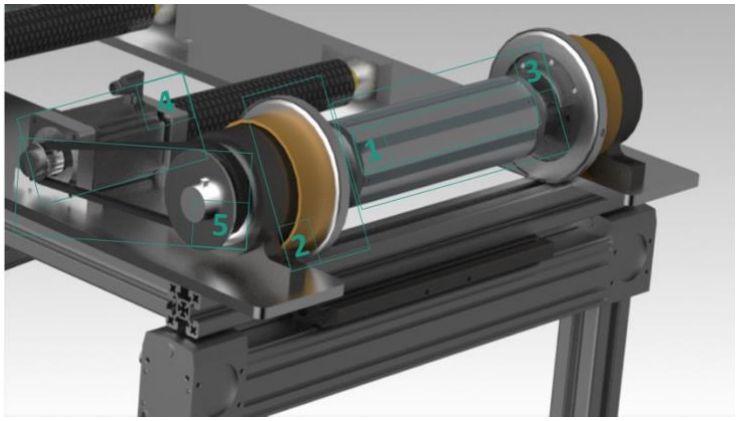

Figure 5.6: Unwinding and linear guide mechanism.

All of the following parts described are shown in Figure 5.7. As discussed in Chapter 4.2.1, it is desirable to use carbon fiber roll on idler rolls (‘**2**’) instead of the aluminum roll. There are two main reasons for this selection. Firstly, aluminum rolls can contaminate the surface of the electrode causing damage to the separator. The carbon fiber roll is less risky, since the carbon fiber coating is durable, and the material worn out is not electrically conductive. Secondly, the rotational inertia of the aluminum rolls may undulate the web during the acceleration and deceleration of the rolls. Carbon fibre rolls have less inertial effects since it is lightweight. The dancer assembly (‘**3**’) is similar to the one described in contactless electrode transport design and the mechanism works the same except for the roll. The dancer roll in this design is carbon fibre as well. To minimize the folds induced by shear stresses, a considerable amount of space is left between the idler roll after the dancer roll and the side stretching assembly. The longer span allows already a web with fewer instabilities. The adjustable vacuum side stretching assembly can correct the remaining folds.

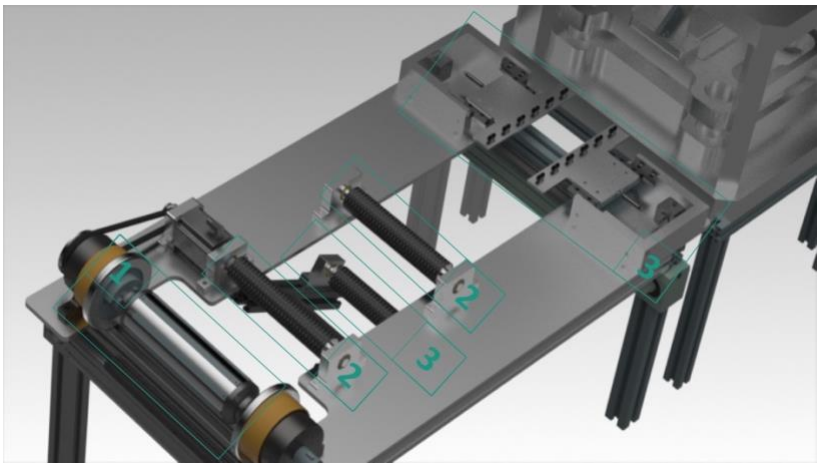

Figure 5.7: Unwinding assembly

Side stretching assembly (‘**3**’) is activated as the web stops moving. This response allows clamping force while the die-cutting assembly is cutting through the web. The side stretching assembly is shown in Figure 5.8. First, six flat suction cups located under both side of the web are actuated so the module can grab the web to stretch the web in the lateral machine direction. Stepper motors located on both sides start pulling on a metal string ensuring the wrinkles are evened out. Having separate motors on the sides allow lateral position adjustment as well as advanced wrinkle control over the web. A metal string is connected to a spring which allows precise measurement of the forces applied on the web by measuring the elongation of the spring. Pulling forces exerted on the spring moves the guide plate through a low friction linear guides. As the die-cutting is completed, the controller interrupts the vacuum supply of the suction pads so the web can start moving again towards the longitudinal machine direction.

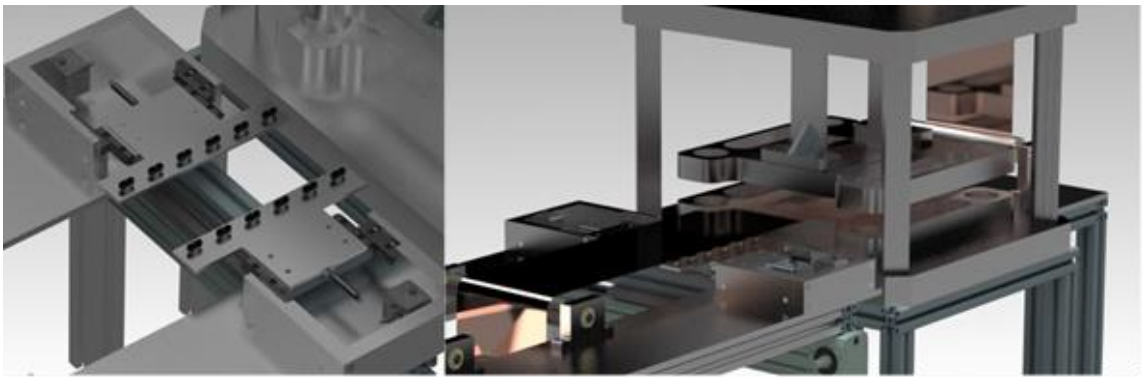

Figure 5.8: Vacuum side stretching assembly

After the electrode sheet is cut the web starts moving again. The residual material is drawn by a vacuum roll (‘**1**’) and winded by a wind-up roll (‘**2**’) shown in Figure 5.9. The vacuum roll was selected for two main purposes. The residual material is too delicate to handle with an aluminum roll. Any web discontinuation results in increased dead time reducing the productivity of the production. The vacuum provides a uniform negative pressure around the web, avoiding any possible tears on the web. Besides, even this portion is torn, since a vacuum is provided from both sides, the discontinuity could be prevented. Secondly, vacuum roll and the side clamp mechanism secures a taut web so that the die mold can go through the web with precise positioning.

A stepper motor (‘**3**’) drives windup roll. Torque is transmitted through a gear belt pair. Rotation pulls the web from the vacuum roll and collects it around the windup roll. Windup roll diameter is much less than the other rolls to maximize the collection of material residue without needing to dismount the roll.

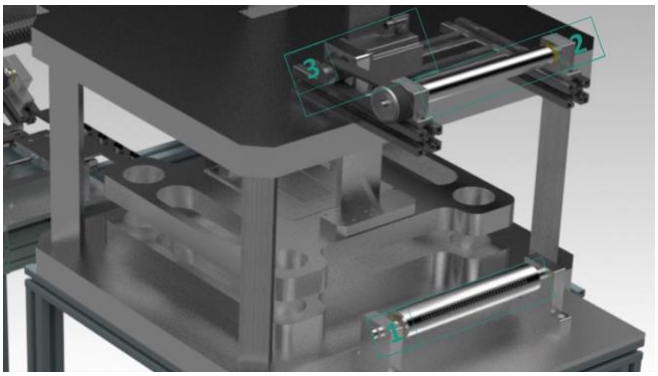

Figure 5.9: Vacuum gripper roll and the winding roll

5.2 Design Selection

Table 5.1: Comparison of contactless electrode transport, the second and the reference design

Concept Designs	Percentage (%)	Contactless Transport		Second Design		Single Sheet Stacking Unit at wbk	
		Points	Value	Points	Value	Points	Value
Stability	15	5	75	3	45	2	30
Speed	15	4	60	3	45	2	30
Material Quality	14	5	70	4	56	3	42
Process Reliability	13	3	39	3	39	5	65
Contamination	10	5	50	4	40	3	30
Costs	10	2	20	3	30	4	40
Lifetime	9	4	36	3	27	3	27
Maintenance	8	4	32	3	24	3	24
Mounting	6	5	30	4	24	4	24
Total	100	412		330		312	

Table 5.1 shows a comparison of the two design proposals and single sheet stacking unit at wbk described in 5.1 and 2.4.3 respectively. In this section, the single sheet stacking unit at wbk is referred to as the current system. Stability and speed are the primary key performance indicators of this work. Obtaining improved results of these parameters makes the production process faster and cost-efficient. Improving process speed without satisfying material quality standards is necessary for lithium-ion battery production. Electrode sheets should have a preserved surface quality free of scratches, wrinkles and loose-particles. Electrode web transport should operate without stopping due to any discontinuity or other process errors. This factor is considered under process reliability. Contamination is a primary concern for lithium-ion batteries. Particularly for safety reasons, electrode webs should be free of any sharp pieces, burr and water particles. Cost and lifetime of the material are considered together. A long lifetime of a product can make up for the cost differences. The frequency of the maintenance required and practicality of mounting is considered as these factors affect the downtime of the production.

Contactless transport delivered through Air Turn rolls and radial concave air bearing, material conveyed to the die-cutting assembly offers excellent stability. Airflow used to lift and adjust the web has a self-spreading effect. This effect hinders potential fold formations. Friction-free lateral shift minimizes the potential of localized shear stresses. Second design also has improved stability since the light carbon fibre rolls reduce inertial forces exerted on the web. In addition, the side stretching assembly allows active wrinkle removal. However, since there is still contact between the web and carbon fibre rollers, stability is still an issue due to friction. In addition, a high-quality roll surface may cause web slip causing complications. The current system has stability problems. These problems are associated with the short span between the rollers, sizeable inertial forces particularly during acceleration and deceleration and lack of a spreading solution.

Using the pressure differences, an air bearing can adjust the bearing both laterally and longitudinally. Contactless transport enables friction free operation. Friction-free operation and improved stability enable high-speed operation. Web speed is rather limited on the other two designs. Carbon fibre has a slightly better speed performance since it is lighter than aluminum rolls. This reduces the impact of inertial forces. Due to the stability problems mentioned, and also the time required for the gripper to perform the complete cycle of picking up and holding onto the web, overall cycle time to deliver electrode sheets is limited.

Both of the proposed designs feature an acceptable electrode sheet quality. This is obtained by optimizing the process parameters as well as adjusting the design aiming for the stability improvements. Contactless web transport, minimizes the possibility of scratches as the only section which has actual contact with the web is the nip-roller. The contactless solution has passive spreading while the second design has an active spreading. Spreading also implies a considerable quality improvement on the electrode sheets. Fold formations are less likely to occur in the presence of spreading. Quality of the current solution is also arguably acceptable but has a room for improvement.

Process reliability is questionable for both of the designs as both require airflow to fulfill specific functions. Obtaining a reliable operation is complicated and requires a substantial amount of testing before the designs can be implemented into commercial applications. Besides, it is not yet clear if the electrode web can be transported flawlessly by the airflow featured by the contactless web transport. The current design, however, is proven to be reliable and functional despite the stability problem and non-ideal process cycle times.

Contactless transport has no risk of wear over time as it provides a contamination-free environment. The compressed air provided, however, should be filtered before it is fed to the radial air bearing and the Air Turn rolls. The second design will also not have much wear since the coating applied to the carbon fibre rolls are durable. Aluminum rolls fulfill web transport in the current solution. Wear and material chip-off over time may stick to the electrode web surface. Particularly, sharp particles may puncture the surface of the separator as the cell is assembled and compressed into pack form.

The second design is inexpensive in comparison to contactless transport. The Air Turn and radial concave air bearing technology involves complicated design and materials. Formation of an evenly

distributed network of pores on both of these structures requires complex manufacturing solutions. On the other hand, carbon fibre is also costly in contrast to the conventional aluminum rolls. Except for the custom-designed gripper, the current solution is composed of widely available standard components. It is thus a low-cost system.

Friction and wear-free operation improve the lifetime of the contactless transport design substantially. The second design is also durable but still requires maintenance. Web transport is obtained through mechanical movement on both the second design and current solution. This requires periodic lubrication and maintenance of all of the bearings or replacements.

Mounting components of the second and current designs require extensive effort. Both designs rely on complete displacement guide that should be mounted onto the base plate of the complete unwinding assembly. Components of the contactless transport design can be dismounted separately. Besides, the design does not require additional components for lateral transport. The concave radial air bearing is able to control the web both in lateral and longitudinal directions. In addition, mounting of this component is much less complicated in contrast to the linear guide rail used on both the second and current designs.

As a result, both contactless transport design and the second design deliver improved overall attribute performance. The contactless transport design offers better performance for electrode processing line. Despite high-cost components, stability and speed are improved without trading off for the material quality. Particularly for these reasons, this design is more favorable both over the second design and the current solution.

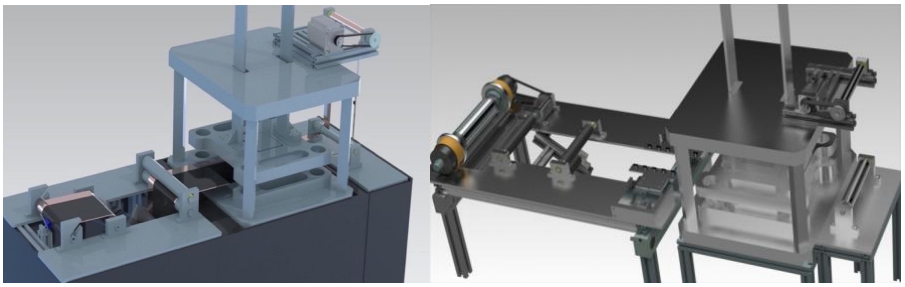

Figure 5.10: Contactless electrode transport (left) and the second design (right).

5.3 Final Remarks

Besides the design proposals, improvements on various process parameters are necessary. The result of the experiments discussed in 4.1 suggested several process adjustments. These adjustments improve the productivity of the manufacturing process and product quality. The web tension, speed, stiffness, misalignment angle and velocity has a considerable influence on the electrode handling.

Evaluating the results in 4.1.2.2, the web showed more stable behavior at $22\ N$ in contrast to operating tension of $69\ N$ and $90\ N$. This behavior holds for web operation with motor speeds until $900\ rpm$. It is thus favorable to operate the web at lower tensions unless the motor speed exceeds $900\ rpm$. However, the web tension has a minimum limit. Beyond this limit, the web is not taut enough. Bagginess results in the undulating web through the operation. If the web is extensively undulated, plastic deformations

on the web surface reduce the material quality. Permanent wrinkles or even delaminations may occur under these conditions.

On the other hand, web thickness variation is inevitable in web handling applications. Web problems such as permanent wrinkles cause thickness variations across the web. As the thicker section of the web comes in contact with the roller, the IRTMs get shorter. This results in tension peaks on the web. Higher web tension yields higher web peaks. In addition, higher web speed also causes higher tension peaks. Determination of the ideal web tension is dependent on the yield strength σ_y of the electrode web, web speed and the minimum tension that causes plastic deformation on the web surface due to undulations. The web tension should be set in between the yield strength and the minimum tension limit.

The parallelism between each roll is critical. Increasing misalignment angle reduces the critical web speed. The position of each roll should be finely calibrated to avoid web instabilities. If there is a significant non-parallelism between two rolls, web tends to be taut on one portion and baggy on the other the transition region between the baggy and the taut zone is often split with a transverse fold. Adjustable web spreading solutions such as side stretching assembly are necessary for these cases.

High tension causes either permanent wrinkles or scratches on the web. The Air Turn avoids this problem by removing the contact between the web and the roll. Additionally, dents and air bubbles on the web surface are avoided using this solution. Besides, self-spreading effect through the use of Air Turn rolls, allow passive removal of wrinkles without using spreading equipment. Moreover, parallelism is not as critical in contactless web transport, as shear stresses due to friction between the web and roll are eliminated.

5.4 Expected Cycle Time Improvement

Both of the proposals include upgrading this linear motion to a continuous motion. Even applying the same rate of acceleration and deceleration through continuous motion, the process speed can potentially increase at least by a factor of two, as the steps of the gripper are halved. This would correspond to about 33.8% cycle time improvement. Further web stability optimizations enable higher critical operating velocity. Conveying the web with 10% higher velocity would bring an additional improvement of 4.5% in the cycle time. Adding such improvements, we conclude with a cycle time improvement of 38.3% of the electrode sheet forming process.

Table 5.2: Cycle time comparison for electrode sheet processing assembly

Processes	Time (s)	
	Current	Design Proposa
Die Cutting Down	0.32	0.32
Die Cutting Up	0.44	0.44
Handling On	0.55	0.495
Handling Off	0.47	0.423
Clamping Down	0.15	0.15
Clamping Up	0.47	0.47
Vacuum Gripper In	2.84	1.278
Vacuum Gripper Out	3	1.35
Vacuum On	0.2	0.2
Vacuum Off	0.2	0.2
Total	**8.64**	**5.326**

Chapter 6

Assesment and Outlook

This chapter finalizes this work assessing conclusions and pointing out aspects to be developed in future work.

6.1 Assesment

Two designs were proposed with the objective of improved stability better quality product, and enhanced operation speed for the electrode processing assembly. A design comparison was carried out in terms of stability, speed, material quality, process reliability, contamination, cost, lifetime, maintenance and mounting. As a result of this benchmarking, contactless electrode transport design was superior over the second design. Additionally, based on the theory and experimental results, optimal operational parameters are proposed to obtain fast and stable operation in chapter 5.3. As a result of these outcomes, a cycle time improvement by 38.3% is foreseen in contrast to the current system.

All of the experiments performed on the materials were conducted outside the dry room conditions. It should be considered that commercial lithium-ion cell production takes place under the dry room conditions where humidity is minimized. This parameter may alter the Young's modulus of the material.

During the closed loop web experiments one of the load cells were damaged due to web tension exceeding the tension limits of the load cell. Majority of the tests were thus performed using one of the load cells. Eventually, the load cell was sent for replacement. Rest of the closed loop web experiments could not be carried out in this interval as there was no bearing support on one side of the roller. The replacement arrived after three months. However, tension calibration could not be completed as the replacement tension load cell did not respond to the communication protocol.

Consequently, closed loop experiments could not be carried out on the anode web. Additionally, most of the results presented on 4.1.2 could not be performed on the cathode for the same reason. Thus, aluminum foil results were instead analyzed to draw conclusions. It is notable that the isotropy of the aluminum was questionable given the tensile tests. Thus, the experiments carried out with the cathode and anode electrodes could lead to different conclusions.

The correlation between the operating tension and tension variation on the web was tested on 4.1.2.2. The results did not satisfy the behavior suggested in the theory discussed on 2.6.1.3. The experiment suggests that operating the web under higher tension results with larger tension variations. Shin and Kwon (2007) suggests otherwise. This contradiction is potentially due to the experiment parameters. The motor speed was set to $900\,rpm$ when these experiments performed. Testing on the same experiment setup with higher rpms may yield contrary implications to those yielded on 4.1.2.2.

It was extremely difficult to place the copper web into the experimental setups without causing severe wrinkles. Thus copper was neither in closed loop tests nor in side stretching tests used. Copper foil has a very low stiffness as it is extremely thin ($9\,\mu m$). These wrinkles would affect the results of each experiment. Hence the measurements would and conclusions drawn from this experiments would be corrupted. Since these experiments could not be performed the results of the stress-strain test was not necessary in this case.

On closed loop experiments, permanent wrinkles were mostly generated on the interface between the web and the adhesive tape. The tape band joins both ends of the tape. When this tape is not uniformly applied or air was trapped between the band and the web it either leads to baggy edges or permanent wrinkle generations. Thus, the application of the tape bands was time-consuming on each closed loop experiment.

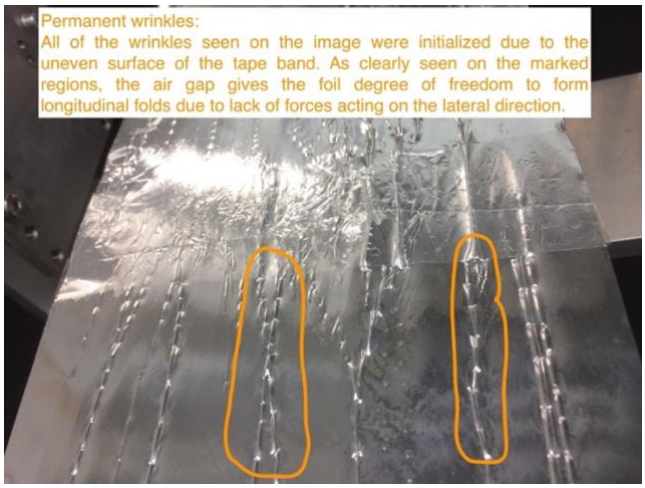

Figure 6.1: Wrinkle generation due to air bubbles trapped between the web and the adhesive tape.

6.2 Outlook

Air Turn rolls and concave radial air bearing is discussed in chapter 2.2.1.2. The experiments presented on the literature showed substantial stability improvement web handling. These results can be found in Figure A. 1 and Figure A. 2. However, additional experiments on the electrode web are necessary to ensure the validity of featured attributes. Furthermore, stable behavior may be disrupted at high-speed operations. Thus, it is necessary to test this technology with electrode web at different speeds to investigate the effect of speed on contactless electrode web transport. In addition, it is strongly recommended to test the applicability of the components besides the Air Turn and concave air bearings. Operating the electrode web on carbon fibre, vacuum rolls and vacuum side stretching assembly should be tested. Only this way, proposed designs can be validated. Moreover, the benchmarking carried out on these designs should agree with the experimental results.

On the other hand, the concave radial air bearing is controlled with a manual handle on the design proposed in 5.1.1. Precise automated control of the air bearing is expected to be complicated. Different type of actuator should be considered with the aim of providing advanced control of the web speed and positioning both in lateral and longitudinal machine directions.

Using image recognition, active prevention of instabilities are possible. An advanced control system which detects the oncoming instabilities in advance can direct the dancer rollers and the web spreading mechanism to optimize the web. However, the speed of the image recognition is a concern as the major focus of this mechanism is to speed up the lithium-production in the first place. Thus, such advanced control mechanisms should be assessed with respect to speed.

Annex I

Air Turn Roll Experimental Results

ANNEX I

Air Turn Rolls are tested for PET and stainless steel webs. The results include the fly height- foil width relation with respect to the orientation of the sensor, fly height-preload force applied.

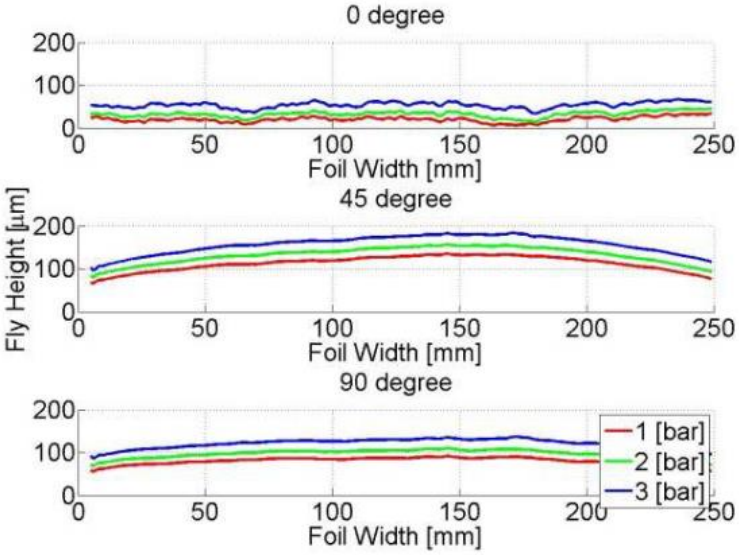

Figure A. 1: Fly height of PET foil at several positions with different supply air pressures

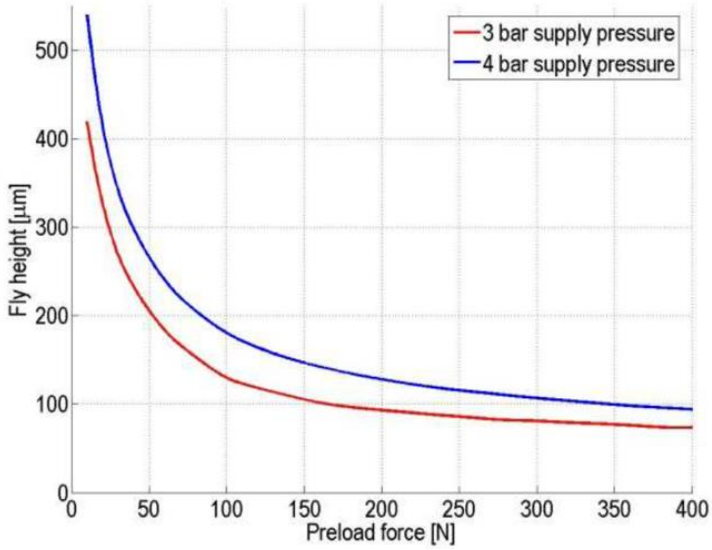

Figure A. 2: Relation of applied force, supply pressure to fly height of a stainless steel foil (van Dam et al., 2014)

Annex II

Roll Roundess Results

ANNEX II

Aluminum rolls used in the test bench should be verified for roundness tolerances. Rolls used in the setup should have high surface quality such that the high-tolerance surface does not affect the web tension measurements.

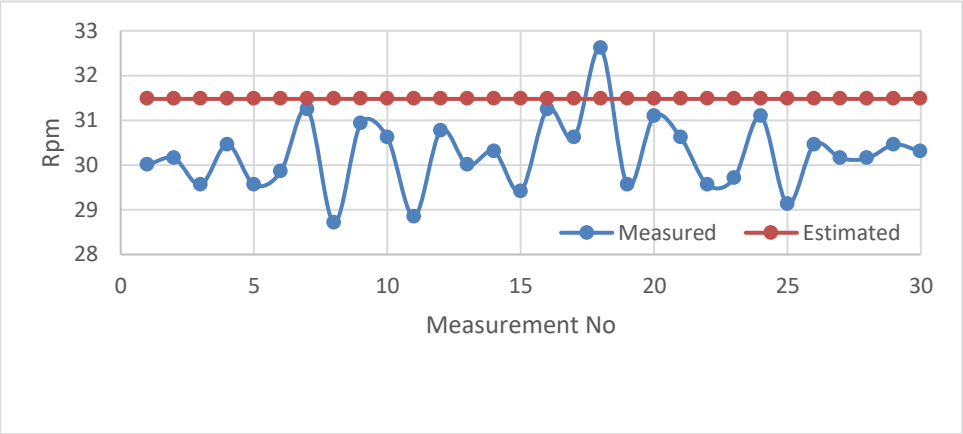

Figure A. 3: Estimated and measured rpm of the roll when the motor is operated at $200\ rpm$.

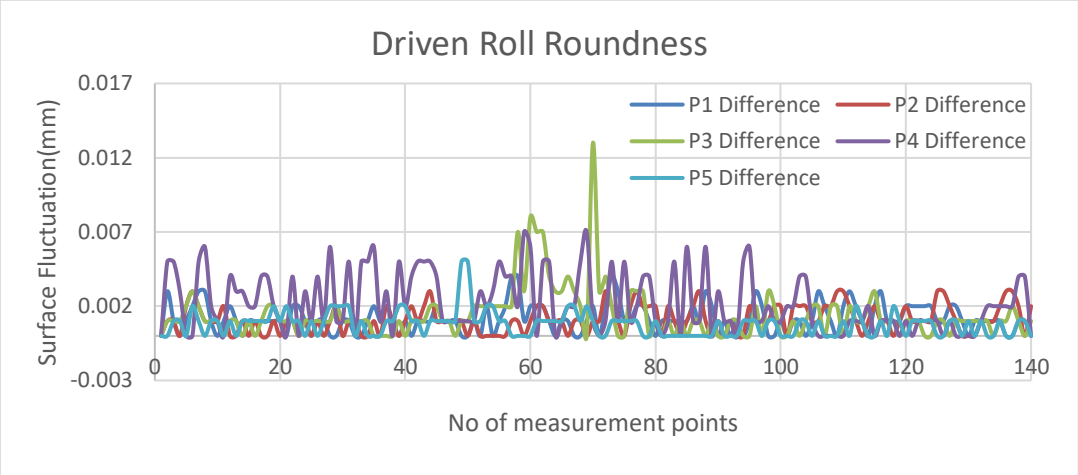

Figure A. 4: Roundness check of the driven roll 5 different widths

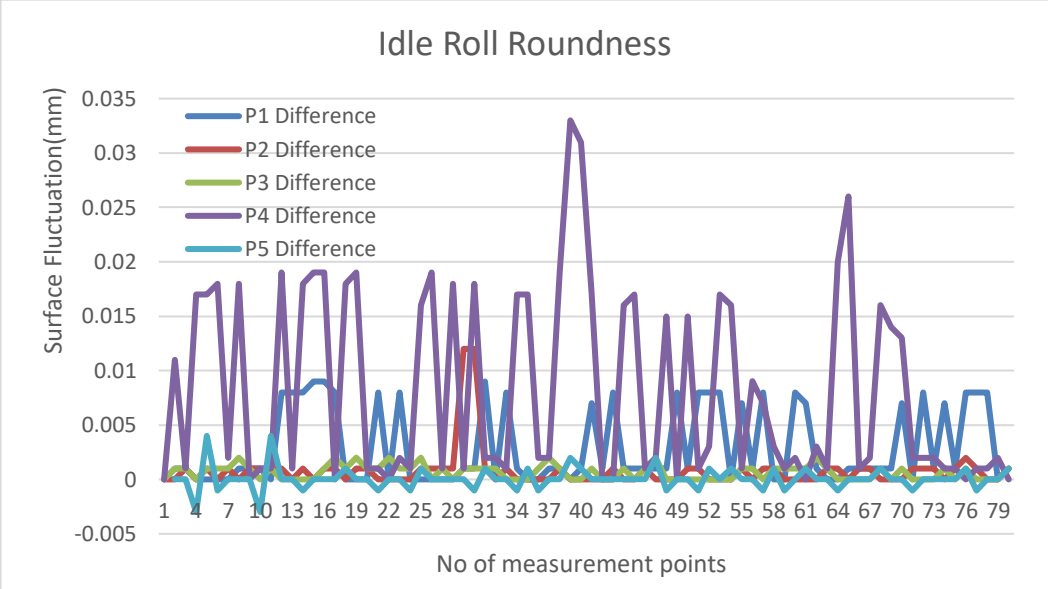

Figure A. 5: Roundness check of the idle roll at 5 different locations

Annex III

Tensile Tests

ANNEX III

Images of samples from tensile tests are shown in this section.

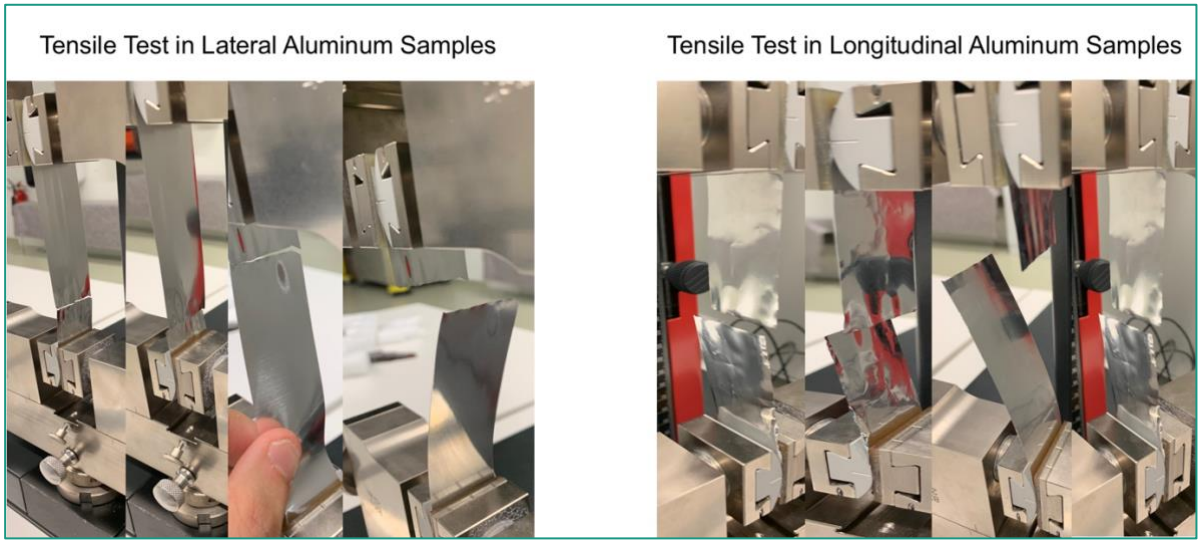

Figure A. 6: Comparison of lateral and longitudinal tensile tests on aluminum samples

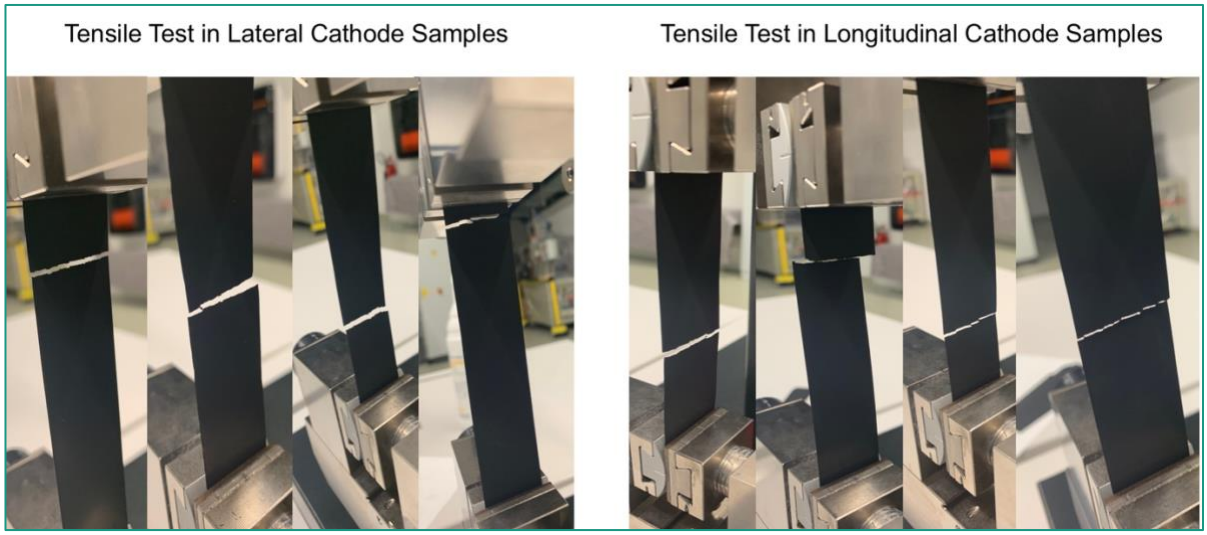

Figure A. 7: Comparison of lateral and longitudinal tensile tests on cathode samples

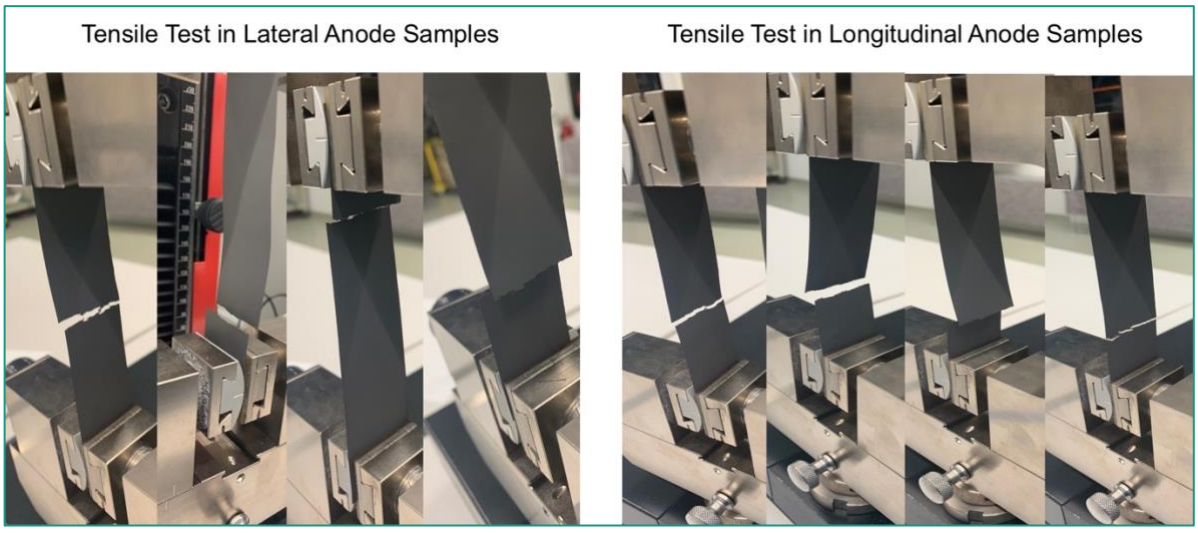

Figure A. 8: Comparison of lateral and longitudinal tensile tests on anode samples

Annex IV

Closed Loop Test Aluminum vs. Cathode

ANNEX IV

Images of samples from closed loop tests are shown in this section.

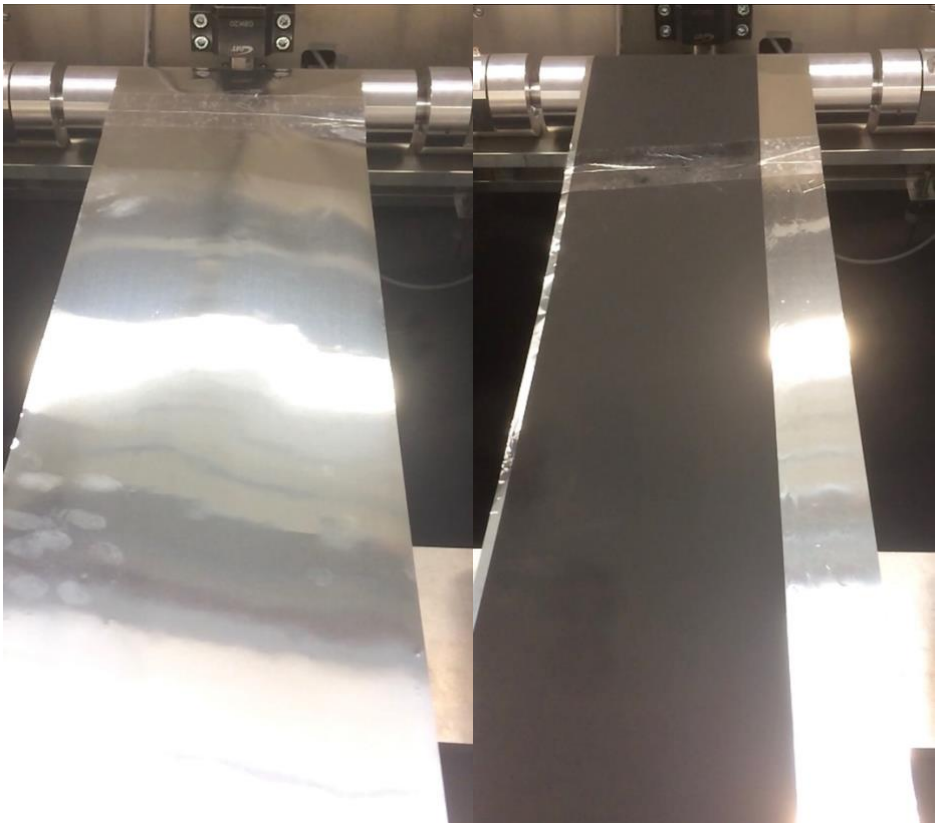

Figure A. 9: Comparison of Aluminum and Cathode samples on closed loop test

Annex V

Stiffness Ratio Calculations

ANNEX V

```python
#defining Young's modulus of each sample
E1_al= 30.2*1000
E1_cat= 6.26*1000
#average longitudinal Tension applied on the samples
T_avg = 24.3
#span length of each sample
l1_al = (158/2)*10
l1_cat =(156.5/2)*10
#thickness of each sample
t1_al = 0.019
t1_cat = 0.120
#poissons ratio of aluminum and cathode
nu1_al = 0.33
nu1_cat = 0.2
#implementation of stiffness ratio formula
eps1_al = (E1_al*(t1_al**3))/(12*(1-nu1_al)*T_avg*(l1_al**2))*(10**8)
eps1_cat = (E1_cat*(t1_cat**3))/(12*(1-nu1_cat)*T_avg*(l1_cat**2))*(10**8)

print('Stiffness ratio of aluminum web: %fE-8'%eps1_al)
print('Stiffness ratio of positive electrode web: %fE-8'%eps1_cat)
print('Factor of stiffness ratio (stiffness ratio of cathode/stiffness ratio of al): %f'%(round((eps1_cat/eps1_al),2)))
```

```
Stiffness ratio of aluminum web: 0.169884E-8
Stiffness ratio of positive electrode web: 7.573068E-8
Factor of stiffness ratio (stiffness ratio of cathode/stiffness ratio of al): 44.580000
```

Figure A. 10: Calculation of stiffness ratio for aluminum and cathode samples.

References

Arzate, A., Tanguy, P.A., 2004. Air entrainment on a moving continuous web. Chemical engineering science. 59, 3527.

Aydemir, M., Glodde, A., Mooy, R., Bach, G., 2017. Increasing productivity in assembling z-folded electrode-separator-composites for lithium-ion batteries. CIRP Annals 66, 25–28. https://doi.org/10.1016/j.cirp.2017.04.096

Banichuk, N., Jeronen, J., Neittaanmäki, P., Saksa, T., Tuovinen, T., 2013. Theoretical study on travelling web dynamics and instability under non-homogeneous tension. International Journal of Mechanical Sciences 66, 132–140. https://doi.org/10.1016/j.ijmecsci.2012.10.014

Baumeister, M., 2017. Automatisierte Fertigung von Einzelblattstapeln in der Lithium-Ionen-Zellproduktion, Forschungsberichte aus dem wbk, Institut für Produktionstechnik, Karlsruher Institut für Technologie (KIT). Shaker Verlag, Aachen.

Baumeister, M., Fleischer, J., 2014. Integrated cut and place module for high productive manufacturing of lithium-ion cells. CIRP Annals 63, 5–8. https://doi.org/10.1016/j.cirp.2014.03.063

Baunach, M., Jaiser, S., Schmelzle, S., Nirschl, H., Scharfer, P., Schabel, W., 2016. Delamination behavior of lithium-ion battery anodes: Influence of drying temperature during electrode processing. Drying Technology 34, 462–473. https://doi.org/10.1080/07373937.2015.1060497

Biernat, B., 2017. Konstruktion und Aufbau eines Versuchstandes zur definierten Beanspruchung von Elektroden und Separatoren für Lithium-Ionen Batterien. Karlsruher Institut für Technologie, Karlsruhe.

Bonatti, C., Mohr, D., 2016. Anisotropic viscoplasticity and fracture of fine grained metallic aluminum foil used in Li-ion batteries. Materials Science and Engineering: A 654, 329–343. https://doi.org/10.1016/j.msea.2015.11.048

Burheim, O.S., 2017. Engineering Energy Storage. Academic Press, London.

Curry, C., 2017. BNEF Lithium-ion Battery Costs and Market. Bloomberg New Energy Finance.

Damour, J., 2017. Air Loaded Adjusta-Pull® Anti-Wrinkle System by CAC.

Damour, J., 2016. Web Spreading Devices Webinar.

Delettre, A., Laurent, G.J., Haddab, Y., Le Fort-Piat, N., 2012. Robust control of a planar manipulator for flexible and contactless handling. Mechatronics 22, 852–861. https://doi.org/10.1016/j.mechatronics.2012.05.003

Devitt, A.J., 2010. Method and apparatus for in-line processing and mimediately sequential or simultaneous processing of filat and flexible substrates through viscous shear in thin cross section gaps for the manufacture of micro-electronic circuits or displays.

Devitt, D., Allen, J., 2014. Viscous Shear in Air Bearing Gaps for Precise Web Tension and Temperature Control (Experiment Report). New Way Air Bearings, Ashton, PA, USA.

Dwivedula, R.V., Zhu, Y., Pagilla, P.R., 2006. Characteristics of active and passive dancers: A comparative study. Control Engineering Practice 14, 409–423. https://doi.org/10.1016/j.conengprac.2005.02.003

Fantoni, G., Santochi, M., Dini, G., Tracht, K., Scholz-Reiter, B., Fleischer, J., Kristoffer Lien, T., Seliger, G., Reinhart, G., Franke, J., Nørgaard Hansen, H., Verl, A., 2014. Grasping devices and methods in automated production processes. CIRP Annals 63, 679–701. https://doi.org/10.1016/j.cirp.2014.05.006

Fleischer, J., Förster, F., Gebhardt, J., 2016. Sustainable Manufacturing Through Energy Efficient Handling Processes. Procedia CIRP 40, 574–579. https://doi.org/10.1016/j.procir.2016.01.136

Giuseppe, M., 2011. Pneumatic needle gripper. US8104807B2.

Glaize, C., Genies, S., 2013. lithium batteries and other electrochemical storage systems, Electrical engineering series. ISTE Wiley, Hoboken, NJ.

Gulbinska, M.K. (Ed.), 2014. Lithium-ion battery materials and engineering: current topics and problems from the manufacturing perspective, Green energy and technology. Springer, London Heidelberg New York Dordrecht.

Hashimoto, H., 2007. Prediction model of paper-web wrinkling and some numerical calculation examples with experimental verifications. Microsyst Technol Microsystem Technologies 13, 933–941.

Hawkins, W.E., 2003. The plastic film and foil Web handling guide. CRC Press, Boca Raton.

Heiland, P., 2003. Electrostatic gripper. EP1387392B1.

Iwakura, C., Fukumoto, Y., Inoue, H., Ohashi, S., Kobayashi, S., Tada, H., Abe, M., 1997. Electrochemical characterization of various metal foils as a current collector of positive electrode for rechargeable lithium batteries. Journal of Power Sources 68, 301–303. https://doi.org/10.1016/S0378-7753(97)02538-X

Jia, Z., Li, T., 2016. Failure mechanics of a wrinkling thin film anode on a substrate under cyclic charging and discharging. EML Extreme Mechanics Letters 8, 273–282.

Kaiser, J., Wenzel, V., Nirschl, H., Bitsch, B., Willenbacher, N., Baunach, M., Schmitt, M., Jaiser, S., Scharfer, P., Schabel, W., 2014. Prozess- und Produktentwicklung von Elektroden für Li-Ionen-Zellen. Chemie Ingenieur Technik 86, 695–706. https://doi.org/10.1002/cite.201300085

Kang, C.-G., Lee, B.-J., 2008. MIMO Tension Modelling and Control for Roll-to-roll Converting Machines. IPV IFAC Proceedings Volumes 41, 11877–11882.

Koc, H., Knittel, D., de Mathelin, M., Abba, G., 2002. Modeling and Robust Control of Winding Systems for Elastic Webs. IEEE Transactions On Control Systems Technology 10, 197–208.

Kuribayashi, K., Nakajima, K., 1984. An Active Dancer Roller System for Tension Control of Wire and Sheet. IFAC Proceedings Volumes 17, 1747–1752. https://doi.org/10.1016/S1474-6670(17)61227-8

Land, C., Karlstads universitet, Avdelningen för Kemiteknik, 2010. Baggy paper webs effect of uneven moisture and grammage profiles in different process steps. Faculty of Technology and Science, Chemical Engineering, Karlstads universitet, Karlstad.

Li, W., Long, R., Chen, H., Geng, J., 2017. A review of factors influencing consumer intentions to adopt battery electric vehicles. Renewable and Sustainable Energy Reviews 78, 318–328. https://doi.org/10.1016/j.rser.2017.04.076

Lin, C.C., Mote, C.D., 1996. Eigenvalue solutions predicting the wrinkling of rectangular webs under non-linearly distributed edge loading. Journal Of Sound And Vibration 197, 179–190.

Linden, D., Reddy, T.B. (Eds.), 2002. Handbook of batteries, 3rd ed. ed, McGraw-Hill handbooks. McGraw-Hill, New York.

Liu, Y., Guo, K., Wang, C., Gao, H., 2018. Wrinkling and ratcheting of a thin film on cyclically deforming plastic substrate: Mechanical instability of the solid-electrolyte interphase in Li–ion batteries. Journal of the Mechanics and Physics of Solids. https://doi.org/10.1016/j.jmps.2018.08.006

Löchte, C., Kunz, H., Schnurr, R., Langhorst, S., Dietrich, F., Raatz, A., Dilger, K., Dröder, K., 2014. Form-Flexible Handling and Joining Technology (FormHand) for the Forming and Assembly of Limp Materials. Procedia CIRP 23, 206–211. https://doi.org/10.1016/j.procir.2014.10.086

Mahmoudzadeh Andwari, A., Pesiridis, A., Rajoo, S., Martinez-Botas, R., Esfahanian, V., 2017. A review of Battery Electric Vehicle technology and readiness levels. Renewable and Sustainable Energy Reviews 78, 414–430. https://doi.org/10.1016/j.rser.2017.03.138

Maiser, E., 2014. Battery packaging - Technology review. American Institute of Physics, pp. 204–218. https://doi.org/10.1063/1.4878489

Masias, A., 2018. Lithium-Ion Battery Design for Transportation, in: Behaviour of Lithium-Ion Batteries in Electric Vehicles : Battery Health, Performance, Safety, and Cost. Springer International Publishing, Cham, pp. 1–34.

Meyer, C., Bockholt, H., Haselrieder, W., Kwade, A., 2017. Characterization of the calendering process for compaction of electrodes for lithium-ion batteries. Journal of Materials Processing Technology 249, 172–178. https://doi.org/10.1016/j.jmatprotec.2017.05.031

Myung, S.-T., Hitoshi, Y., Sun, Y.-K., 2011. Electrochemical behavior and passivation of current collectors in lithium-ion batteries. Journal of Materials Chemistry 21, 9891. https://doi.org/10.1039/c0jm04353b

Ozawa, K., Matsuki, K., 2009. General Concepts, in: Lithium Ion Rechargeable Batteries. Wiley-VCH, Weinheim, p. 336.

Pfeiffer, J.D., 1987. Mechanics and Dynamics of Web Motion between Spans, in: Mechanics and Dynamics of Web Motion between Spans. Presented at the American Control Conference, IEEE, Minneapolis, MN, USA. https://doi.org/10.23919/ACC.1987.4789656

Pham, D.T., Yeo, S.H., 1988. A knowledge-based system for robot gripper selection: criteria for choosing grippers and surfaces for gripping. International Journal of Machine Tools and Manufacture 28, 301–313. https://doi.org/10.1016/0890-6955(88)90045-4

Roisum, D.R., 2003. Thinking Thin? Presented at the AIMCAL 2003 Fall Technical Conference.

Roisum, D.R., 1998. The mechanics of web handling. TAPPI Press, Atlanta, Ga.

Sahraei, E., Kahn, M., Meier, J., Wierzbicki, T., 2015. Modelling of cracks developed in lithium-ion cells under mechanical loading. RSC Advances 5, 80369–80380. https://doi.org/10.1039/C5RA17865G

Samsung Newsroom, 2017. Samsung Announces Cause of Galaxy Note7 Incidents in Press Conference (Press Conference). Samsung, Seoul.

Schlick, D.T., Hertel, D.G., Hagemann, B., Maiser, D.E., Kramer, M., 2011. E-Mobility – a promising field for the future. Roland Berger Strategy Consultants.

Schlögl Robert, 2012. Chemical Energy Storage. De Gruyter, Berlin, Boston. https://doi.org/10.1515/9783110266320

Schmits, C.J., 2018. Ermittlung von Wirkzusammenhängen bei der Verarbeitung von Elektroden in der Lithium-Ionen Batterieproduktion. Karlsruher Institut für Technologie, Karlsruhe.

Schröder, R., Aydemir, M., Glodde, A., Seliger, G., 2016a. Design and Verification of an Innovative Handling System for Electrodes in Manufacturing Lithium-ion Battery Cells. Procedia CIRP 50, 641–646. https://doi.org/10.1016/j.procir.2016.04.198

Schröder, R., Aydemir, M., Seliger, G., 2017. Comparatively Assessing different Shapes of Lithium-ion Battery Cells. Procedia Manufacturing 8, 104–111. https://doi.org/10.1016/j.promfg.2017.02.013

Schröder, R., Glodde, A., Aydemir, M., Seliger, G., 2016b. Increasing Productivity in Grasping Electrodes in Lithium-ion Battery Manufacturing. Procedia CIRP 57, 775–780. https://doi.org/10.1016/j.procir.2016.11.134

Seliger, G., Szimmat, F., Niemeier, J., Stephan, J., 2003. Automated Handling of Non-Rigid Parts. CIRP Annals 52, 21–24. https://doi.org/10.1016/S0007-8506(07)60521-6

Serrenho, A.C., Warr, B., Sousa, T., Ayres, R.U., Domingos, T., 2016. Structure and dynamics of useful work along the agriculture-industry-services transition: Portugal from 1856 to 2009. Structural Change and Economic Dynamics 36, 1–21. https://doi.org/10.1016/j.strueco.2015.10.004

Seshadri, A., Pagilla, P.R., 2012. Adaptive control of web guides. Control Engineering Practice Control Engineering Practice 20, 1353–1365.

Shelton, J.J., 1986. Dynamics of Web Tension Control with Velocity or Torque Control, in: Dynamics of Web Tension Control with Velocity or Torque Control. Presented at the American Control Conferenece, 1986, IEEE, Seatle, WA, USA, pp. 1423–1427. https://doi.org/10.23919/ACC.1986.4789149

Shelton, J.J., 1969. Lateral dynamics of a moving web. University of Oklahoma, [Norman, Okla.].

Shin, K.-H., Kwon, S.-O., 2007. The Effect of Tension on the Lateral Dynamics and Control of a Moving Web. IEEE Transactions on Industry Applications 43, 403–411. https://doi.org/10.1109/TIA.2006.889742

Sievers, L., Balas, M.J., von Flotow, A., 1988. Modeling of web conveyance systems for multivariable control. IEEE Transactions on Automatic Control 33, 524–531. https://doi.org/10.1109/9.1247

Singh, M., Kaiser, J., Hahn, H., 2015. Thick Electrodes for High Energy Lithium Ion Batteries. Journal of The Electrochemical Society 162, A1196–A1201. https://doi.org/10.1149/2.0401507jes

Smith, R.D., 2012. Guidelines for Rolls Used in Web Handling, in: AIMCAL Converting Quarterly Issue 2012, Quarter 3. Presented at the AIMCAL Europe 2012 Web Handling Conference, Prague, Czechia.

Stephan, J., 2001. Beitrag zum Greifen von Textilien, Berichte aus dem Produktionstechnischen Zentrum Berlin. IPK, Berlin.

Tang, W., Chen, J., Yin, Z., 2017. Elastic buckling analysis of webs transported through rollers with misalignment. Thin-walled structures. 121, 1–7.

Ünlü, B.S., Atik, E., 2007. Determination of friction coefficient in journal bearings. Materials & Design 28, 973–977. https://doi.org/10.1016/j.matdes.2005.09.022

U.S Department of Energy, 2014. Electric and Hybrid Electric Vehicle Sales: December 2010 - June 2013. Washington DC.

van Dam, T., Hamersma, I., Spaan, H., 2014. Porous Air Bearing Techniques for Contactless Handling, Flattening and Stabilization of Webs. AIMCAL 4.

Vetter, J., Novák, P., Wagner, M.R., Veit, C., Möller, K.-C., Besenhard, J.O., Winter, M., Wohlfahrt-Mehrens, M., Vogler, C., Hammouche, A., 2005. Ageing mechanisms in lithium-ion batteries. Journal of Power Sources 147, 269–281. https://doi.org/10.1016/j.jpowsour.2005.01.006

Wang, L., Yin, S., Zhang, C., Huan, Y., Xu, J., 2018. Mechanical characterization and modeling for anodes and cathodes in lithium-ion batteries. POWER Journal of Power Sources 392, 265–273.

Westermeier, M., Reinhart, G., Zeilinger, T., 2013. Method for quality parameter identification and classification in battery cell production quality planning of complex production chains for battery cells, in: 2013 3rd International Electric Drives Production Conference (EDPC). Presented at the 2013 3rd International Electric Drives Production Conference (EDPC), IEEE, Nuremberg, Germany, pp. 1–10. https://doi.org/10.1109/EDPC.2013.6689742

Wiedemann, A.H., Goldin, G.M., Barnett, S.A., Zhu, H., Kee, R.J., 2013. Effects of three-dimensional cathode microstructure on the performance of lithium-ion battery cathodes. Electrochimica Acta 88, 580–588. https://doi.org/10.1016/j.electacta.2012.10.104

Zhang, C., Xu, J., Cao, L., Wu, Z., Santhanagopalan, S., 2017. Constitutive behavior and progressive mechanical failure of electrodes in lithium-ion batteries. Journal of Power Sources 357, 126–137. https://doi.org/10.1016/j.jpowsour.2017.04.103

Zhu, J., Wierzbicki, T., Li, W., 2018. A review of safety-focused mechanical modeling of commercial lithium-ion batteries. Journal of Power Sources 378, 153–168. https://doi.org/10.1016/j.jpowsour.2017.12.034